Engineering Electrochemical Transformations in Continuous-Flow Reactors

Engineering Electrochemical Transformations in Continuous-Flow Reactors

PROEFSCHRIFT

ter verkrijging van de graad van doctor aan de Technische Universiteit Eindhoven, op gezag van de rector magnificus prof.dr.ir. F.P.T. Baaijens, voor een commissie aangewezen door het College voor Promoties, in het openbaar te verdedigen op vrijdag 7 september 2021 om 16:00 uur

door

Yiran Cao

geboren te Gansu, China

Dit proefschrift is goedgekeurd door de promotoren en de samenstelling van de promotiecommissie is als volgt:

voorzitter:	prof.dr.ir. D. C. Nijmeijer
1e promotor:	prof.dr. T. Noël (Universiteit van Amsterdam)
co-promotor:	Prof.Dr.Eng. F. Gallucci
leden:	Prof.Dr.-Ing. N. Kockmann (TU Dortmund)
	prof.dr. S. Kuhn (KU Leuven)
	prof.dr. E. V. Rebrov
	dr. N. Padoin (Universidade Federal de Santa Catarina)
	dr. M. F. Neira d'Angelo MSc

Het onderzoek of ontwerp dat in dit proefschrift wordt beschreven is uitgevoerd in overeenstemming met de TU/e Gedragscode Wetenschapsbeoefening.

心之所愿，无所不成

Nothing is impossible to a willing heart

Engineering Electrochemical Transformations in Continuous-Flow Reactors

Yiran Cao

Eindhoven University of Technology, 2021

A catalogue record is available from the Eindhoven University of Technology Library

ISBN: 978-90-386-5330-3

This work was funded by the Chinese Scholarship Council (CSC)

Printed by GVO drukkers & vormgevers B.V.

Cover designed by Yiran Cao & Dr. Xintong Ma

Contents

Chapter 1. Introduction 1

Chapter 2. Design of an undivided electrochemical flow microreactor 11

Chapter 3. Accelerating sulfonyl fluoride electrosynthesis in flow 29

Chapter 4. Efficient electrocatalytic reduction of furfural to furfuryl alcohol 43

Chapter 5. Paired electrochemical conversion of furfural in flow 59

Chapter 6. CFD study on gas bubble effects in Taylor flow electrochemistry 73

Chapter 7. CFD study on liquid-liquid Taylor flow electrochemistry 99

Outlook 135

Publications 136

Acknowledgement 137

About the author 138

CHAPTER 1

Introduction

1.1 Overview

Over the last century, researches on continuous-flow electrochemistry have flourished to a great extent ranging from academia to industry.[1,2] Particularly, microreactors have received great attention regarding increased mass and heat transfer phenomena, together with the likelihood to tackle the safety issues and improve analytical protocols therein.[3,4] Both chemists and chemical engineers will benefit from the organic combination of these technologies.[5,6]

Electrochemistry offers tunable and scalable synthetic possibilities to implement redox chemistry with the aid of traceless electrons as reagents, thereby preventing from the use of hazardous chemicals as oxidants or reductants.[7] The general acceptance of electrochemistry originates from the potential to use green electricity derived from sustainable power sources, like solar and wind energy.[8] Therefore, the electrification technology makes it possible to locally produce valuable chemicals, meanwhile effectively improving the current situation on hazardous chemicals storage and transportation.[9]

When combined with flow technology, electrochemistry provides great control over reaction conditions, thus enabling high reproducibility of electrochemistry.[10] The implementation of electrochemical reactions in flow, however, is much more complicated than merely pumping the reaction mixture into a electrolytic cell with narrow interelectrode distance. Understanding the engineering causes supporting the phenomena is crucial and can help to make most of the technology to a higher extent.[2] Hence, this dissertation aims at providing a comprehensive research on organic electrochemistry & microreactor in flow. This includes discussions on chemistry-oriented organic electrosynthesis regarding new reactions development and transformation from batch to flow, together with engineering-oriented microreactor design and application with mass and electron transfer analysis. Owing to the great control over mass transfer in the microflow reactor, electrochemical reactions can be carried out with high precision and reproducibility. With specific potential/current conditions, the conversion and selectivity of the reactions is tunable according to production requirements.

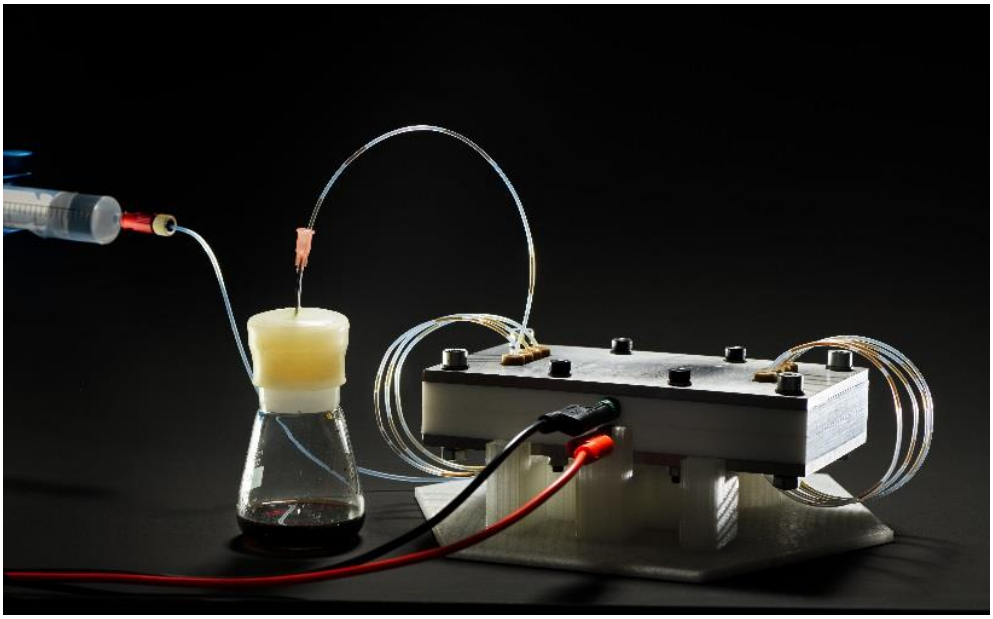

Figure 1.1 An electrochemical flow reactor developed by Noel Research Group.[10]

1.2 Electrochemical microflow reactor

Electrochemical reactions are driven by single electron transfer processes which are initiated at the surface of an electrode. Hence, electrochemical transformations can be regarded as heterogeneous reactions, and thus, substrates or electron mediators need to be transported from the bulk of the solution to the electrode surface. Such mass transport phenomena are, together with electron transfer kinetics, key in the design of an appropriate electrochemical reactor (Figure 1.2A). Typically, an electrochemical reaction starts with the mass transfer of the substrate from the bulk phase to the heterogeneous electrode surface. Next, the substrate adsorbs onto the electrode and an electron transfer can occur, converting the substrate into product. Finally, the product is desorbed from the electrode and diffuses back to the bulk liquid phase.

Evidently, the overall reaction rate will depend mainly on the slowest of these steps, i.e. the rate-determining step. Two extreme scenarios can be distinguished: (i) a charge transfer controlled regime and (ii) a mass transfer controlled regime (Figure 1.2B). With increasing electrode polarization, the reactant concentration at the electrodes becomes zero. In other

words, all reactants are immediately converted upon arrival at the electrode surface and, in such a scenario, the rate of mass transport limits the overall reaction rate. Under these conditions, intensified mass transport, e.g., by more vigorous stirring in batch or through use of static mixers in flow, can reduce the overall reaction time.

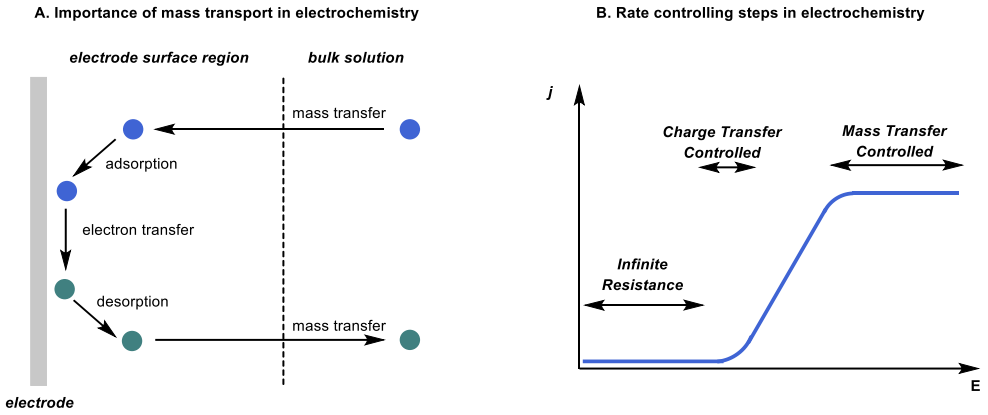

Figure 1.2 (A) Individual steps in an electrochemical transformation. (B) Simplified rate controlling parameters in electrochemistry with j the current density and E the potential measured versus a reference electrode.[10]

To address these problems, especially the mass and heat transfer limitations which restraints the scalability of electrochemical methods, we will describe an undivided-cell electrochemical flow reactor with a flexible reactor volume in chapter 2 (Figure 1.3). This enables its use in two different modes, which are highly relevant for flow chemistry applications, including a serial (volume ranging from 88 µL/channel up to 704 µL) or a parallel mode (numbering-up). The electrochemical flow reactor was subsequently assessed in two synthetic transformations, which confirms its versatility and scaleup potential.

With the above-mentioned reactor, organic electrochemical reactions are preferred to be developed in flow, because electrochemistry is currently resurging in popularity amongst synthetic chemists due to the unique opportunities it provides to activate organic molecules. Simultaneously, continuous-flow technology has been used to enable scalability and to increase the efficiency of the developed electrochemical processes. Many of these processes

involve a gaseous reagent or byproduct generated during the electrochemical process. The presence of a gas phase in flow reactors may lead to the generation of a so-called Taylor flow regime, where gas bubbles and liquid segments alternate. While Taylor flow has almost exclusive positive effects in flow chemistry due to increased mass and heat transfer, we will show that the ramifications of gas bubbles on flow electrochemistry are essentially negative (Figure 1.4). In chapter 6 & chapter 7, computational fluid dynamics (CFD) was used to gain a detailed understanding of the effects respectively induced by the gas phase on the electrochemical process or liquid-liquid two phase flow scenario, taking the reduction of furfural to furfuryl alcohol, or oxidative fluorination of thiophenol as benchmark , which was carried out in an in-house developed electrochemical reactor.

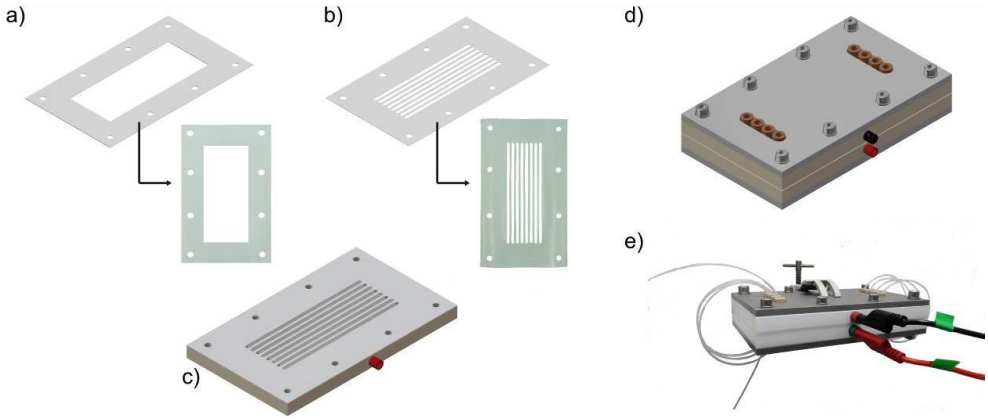

Figure 1.3 Schematic representation of electrochemical flow reactor. a) open-channel spacer; b) 8-channel spacer; c) bottom plate with electrode and 8-channel spacer; d) an overview of the whole device; e) front view of the assembled electrochemical flow reactor with cables.[11]

1.3 Synthetic organic electrochemistry in flow

Synthetic routes toward complex molecules typically comprise many individual synthetic and purification steps. Hence, a total synthesis of such molecules is a time- and labor-intensive undertaking, even for experts. Using continuous-flow technology many of these steps can be combined in one single, streamlined flow configuration.[9,12] This is especially important for the synthesis of short-living species, which can then be subsequently consumed

in a follow-up reaction without extensive degradation. It represents also an important strategy to generate and convert hazardous and toxic intermediates. Consequently, the total inventory can be kept small, which enables one to minimize the risks associated with handling such compounds.[13,14]

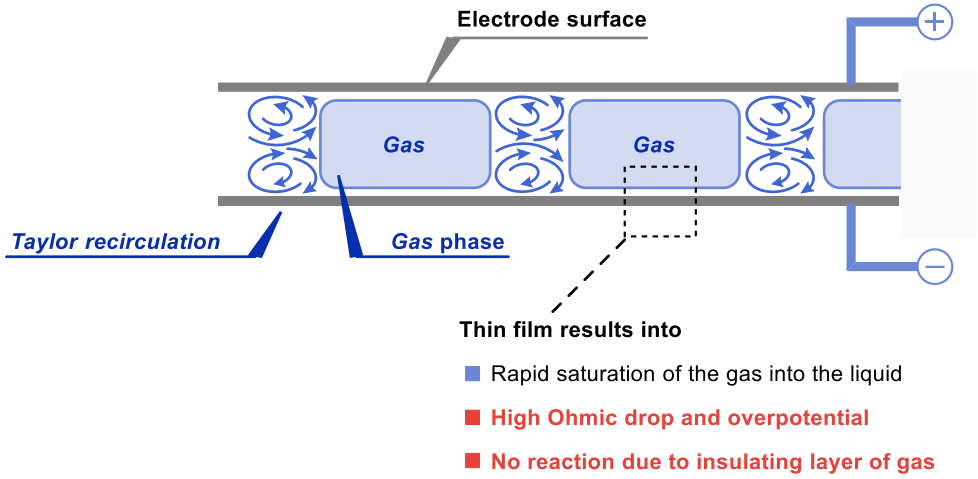

Figure 1.4 Influence of Taylor flow regime on electrochemical microreactors.[15]

In chapter 3, we will report a protocol to prepare sulfonyl fluorides via an anodic oxidation process starting from commodity chemicals like thiols or disulfides and potassium fluoride in flow (Figure 1.5).[16,17] Sulfonyl fluorides are important ynthetic motifs due to their applicability as stable sulfonyl precursors using sulfur(VI) fluoride exchange "click chemistry" (SuFEx). After the electrochemical step, phenyl sulfonyl fluoride was combined with a stream containing phenol, which enables the SuFEx chemistry in flow and yields the corresponding phenyl sulfonate derivative. This strategy enables to produce volatile sulfonyl fluorides and immediately utilize these moieties without intermediate isolation.

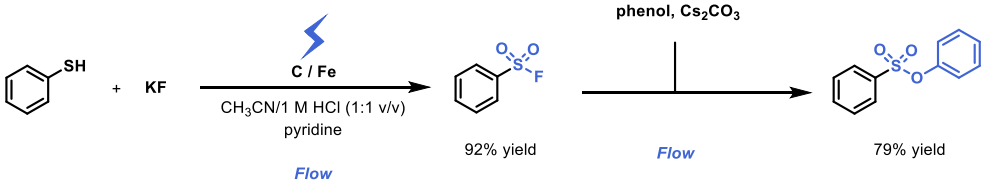

Figure 1.5 Electrochemical synthesis of sulfonyl fluorides in flow and follow up sulfur(VI) fluoride exchange "click" reaction in flow with phenol to yield phenyl sulfonate derivative.[10]

In chapter 4, we will discuss a new, continuous-flow approach enabling furfural electrocatalytic reduction to furfuryl alcohol (Figure 1.6)[18], as furfural is considered to be an essential biobased platform molecule. Recently, its electrocatalytic hydrogenation is regarded as a more environmentally friendly process compared to traditional catalytic hydrogenation. In an undivided multichannel electrochemical flow reactor at ambient temperature and pressure in basic reaction conditions, the yield of furfuryl alcohol reached up to 90% in only 10 min residence time. Interestingly, the faradaic efficiency was 90%, showing a good effectiveness of the consumed electrons in the generation of the targeted compound. Furthermore, the innovation lies in the direct electrolysis using the green solvent ethanol without the need for membrane separation or catalyst modification, which offers further proof for continuous and sustainable production in industry.

In chapter 5, we will further the study on furfural because its derivatization into other useful biobased chemicals is a subject of high interest in contemporary academic and industrial research activities, while most strategies to convert furfural require energy-intensive reaction routes. Here, the use of electrochemical activation allows to provide a sustainable and green alternative offering a disparate approach for the conversion of furfural based on a divergent paired electrochemical conversion, enabling the simultaneous production of 2(5H)-furanone via an anodic oxidation, and the generation of furfuryl alcohol and/or hydrofuroin via a cathodic reduction (Figure 1.7).[19] Using water as solvent and NaBr as supporting electrolyte and electron-mediator, a green and sustainable process was developed, which maximizes productive use of electricity and minimizes byproduct formation.

In a nutshell, this dissertation covers the fundamental principle studies and experimental practices with the use of continuous-flow microreactors to carry out synthetic organic electrochemical reactions. For the researches involving chemical engineering, the design concepts of the modularized electrochemical microflow reactor and the importance of mass transfer in liquid-liquid Taylor flow regime will be discussed. For the studies on organic synthesis in flow, efficient electrocatalytic conversion of furfural to valuable chemicals will be reported, both in undivided- and divided-cell electrochemical microflow reactor. Also, the sulfonyl fluoride electrosynthesis was transferred from batch to flow, thus accelerating the oxidative coupling of thiols and potassium fluoride to a great extent.

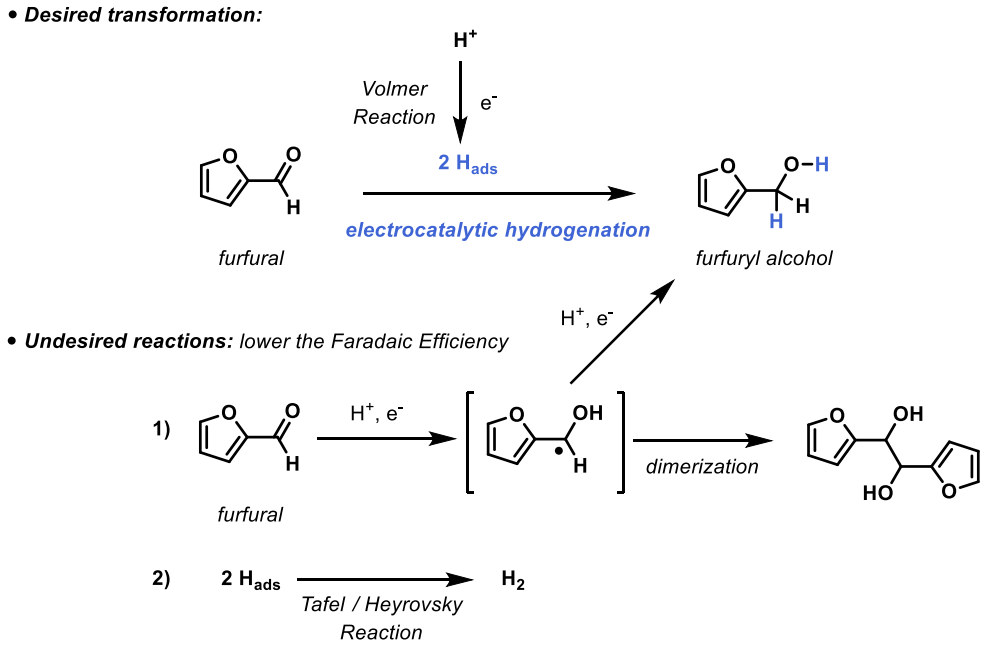

Figure 1.6 Desired electrocatalytic hydrogenation of furfural towards furfuryl alcohol versus undesired reactions.[18]

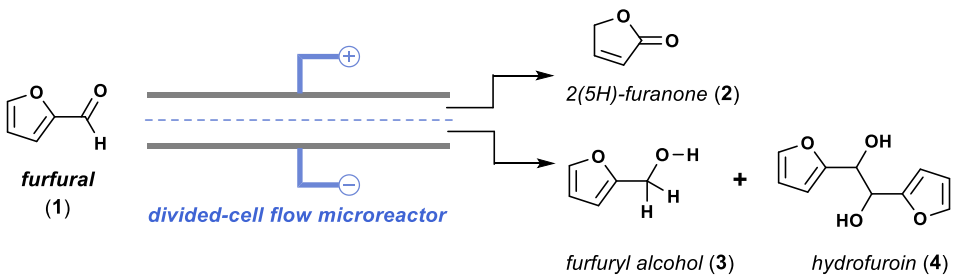

Figure 1.7 Processes based on a divergent paired electrolysis of furfural allows to obtain useful derivatives of both cathodic and anodic processes simultaneously.[19]

References

[1] Nicholls TP, Schotten C, Willans CE (2020). Curr Opin Green Sustain Chem 26:100355

[2] Leech MC, Garcia AD, Petti A, Dobbs AP, Lam K (2020). React Chem Eng 5:977–990

[3] Gutmann B, Kappe CO (2017). J Flow Chem 7:65–71

[4] Folgueiras-Amador AA, Wirth T (2017). J Flow Chem 7:94–95

[5] Pletcher D, Green RA, Brown RCD (2018). Chem Rev 118:4573–4591

[6] Wiebe A, Gieshoff T, Möhle S, Rodrigo E, Zirbes M, Waldvogel SR (2018). Angew Chemie Int Ed 57:5594–5619

[7] Laudadio G, Straathof NJW, Lanting MD, Knoops B, Hessel V, Noël T (2017). Green Chem 19:4061–4066

[8] Armaroli N, Balzani V (2011). Energy Environ Sci 4:3193–3222

[9] Britton J, Raston CL (2017). Chem Soc Rev 46:1250–1271

[10] Noël T, Cao Y, Laudadio G (2019). Acc Chem Res 52:2858–2869

[11] Laudadio G, de Smet W, Struik L, Cao Y, Noël T (2018). J Flow Chem 8:157–165

[12] Pieber B, Gilmore K, Seeberger PH (2017). J Flow Chem 7:129–136

[13] Gutmann B, Cantillo D, Kappe CO (2015). Angew Chemie Int Ed 54:6688–6728

[14] Kockmann N, Thenée P, Fleischer-Trebes C, Laudadio G, Noël T (2017). React Chem Eng 2:258–280

[15] Cao Y, Soares C, Padoin N, Noël T (2021b). Chem Eng J 406:126811

[16] Laudadio G, Bartolomeu A de A, Verwijlen LMHM, Cao Y, de Oliveira KT, Noël T (2019). J Am Chem Soc 141:11832–11836

[17] Cao Y, Adriaenssens B, de A. Bartolomeu A, Laudadio G, de Oliveira KT, Noël T (2020). J Flow Chem 10:191–197

[18] Cao Y, Noël T (2019). Org Process Res Dev 23:403–408

[19] Cao Y, Knijff J, Delparish A, d'Angelo MFN, Noël T (2021a). ChemSusChem 14:590–594

CHAPTER 2

Design of an undivided electrochemical flow microreactor

This chapter is based on:

Laudadio, G.; de Smet, W.; Struik, L.; Cao, Y.; and Noël, T. Design and Application of a Modular and Scalable Electrochemical Flow Microreactor. *Journal of Flow Chemistry* **2018**, 8 (3), 157–165.

Abstract

Electrochemistry constitutes a mild, green and versatile activation method of organic molecules. Despite these innate advantages, its widespread use in organic chemistry has been hampered due to technical limitations, such as mass and heat transfer limitations which restraints the scalability of electrochemical methods. Herein, we describe an undivided-cell electrochemical flow reactor with a flexible reactor volume. This enables its use in two different modes, which are highly relevant for flow chemistry applications, including a serial (volume ranging from 88 μL/channel up to 704 μL) or a parallel mode (numbering-up). The electrochemical flow reactor was subsequently assessed in two synthetic transformations, which confirms its versatility and scaleup potential.

2.1 Introduction

In the past few years, electrochemical transformations have received renewed interest from the synthetic community as a powerful activation mode to enable versatile organic transformations.[1–31] The application of electrons as traceless reagents avoids the use of hazardous or toxic oxidants, providing milder and more sustainable processes.[7, 8, 12, 19, 22] In addition, key electrochemical parameters, such as electric current and potential, can be easily tuned, providing an improved functional group tolerance and selectivity compared to classical thermal approaches.[1, 3, 7, 12] Even though the advantages of electrochemistry appear numerous and many remarkable procedures have been developed employing this technique, many synthetic organic chemists have been discouraged to apply this technique. This can be attributed to the need for specialized equipment and to the knowledge gap of most researchers in this rather esoteric discipline.[2, 9] In addition, electrochemical setups are often affected by process-related problems, like mass- and heat-transfer limitations, and by electrodeposition of organic substances on the electrode surface.[32–40] These drawbacks limit the reproducibility of electrochemistry and can hamper dramatically both its widespread use and its scalability beyond a laboratory scale.[2, 7, 9, 19]

From its advent in 2012, our laboratory has always been interested in the development and manufacturing of novel flow reactor technology to overcome technological limitations in organic synthetic chemistry, such as photochemistry[41–44] and gas-liquid transformations.[45–48] We felt consistently that a Do-It-Yourself (DIY) approach was beneficial as it leveraged a fundamental understanding of the technology.[49] This further enabled us (i) to reduce the overall capital investment, (ii) to repair setups quickly, (iii) to customize the design to our specific needs and (iv) to exploit the technology at its full potential.

We anticipated that also electrochemistry required a technological impetus to overcome the hurdles as described above. Indeed, most of the limitations associated with organic electrochemistry can be overcome by performing electrochemical reactions in continuous-flow microreactors. Specifically, the confined dimensions of micro-flow reactors (up to 1 mm interelectrode gap) allows to reduce the Ohmic drop, to minimize the total amount of supporting electrolytes, and to increase mass transfer from the bulk solution to the electrode

Surface.[32–40, 50–54] In addition, due to the continuous nature of these reactors, generation of local hotspots can be prevented. For these reasons, several electrochemical continuous-flow reactors were developed, commercialized and successfully deployed in a wide variety of electrochemical reactions.[32, 34–39, 51, 55–62] However, despite these great advances, we felt that a cheap, scalable and modular electrochemical flow reactor was still missing. In this article, we disclose our efforts towards this specific goal, and we benchmarked the electrochemical reactor in two relevant electrochemical transformations.

2.2 Results and discussion

Reactor design

At the outset of our design efforts, we defined the following design criteria for our electrochemical flow reactor:

i) flexible reactor volume which allows to carry out the reaction both at small and large scale.
ii) variable spacing between the electrodes, which can be readily accessed through adjustment of the gasket thickness.
iii) simple and flat electrode design to avoid complex machining requirements.
iv) high modularity in combination with easy exchangeable components.
v) inexpensive and solvent-resistant reactor materials.
vi) safe operation of the reactor where the wet part and the electric parts are adequately separated.

For the electrode casing, an easy-to-machine rectangular insulator (polytetrafluoroethylene, 160 mm × 95 mm × 10 mm) was chosen, which is solvent resistant and can be compressed between two stainless steel chucks using 8 screws (four 6 M × 400 mm screws + four 4 M × 400 mm screws) (Figure 2.1 & Figure 1.3). To introduce the liquids into the reactor, we used Super Flangeless Nuts (PEEK, 1/4–28 Flat bottom, for 1/16’’OD) which enable a distributed injection of the reaction mixture over the electrodes (Figure 2.1). Through this design, the contact between the reaction mixture and the insulated electrode holder is minimized. In addition, it also circumvents the need to include in the design a complex and difficult-to-machine flow distributor.[63, 64] The connection between the electrode and the power supply

was achieved via a threaded connection positioned at the insulating plate. Constant contact between the electrical connection and the electrodes was ensured via a spring. From our experience, we found that this strategy represents an excellent alternative to the classical soldered electrical contacts.

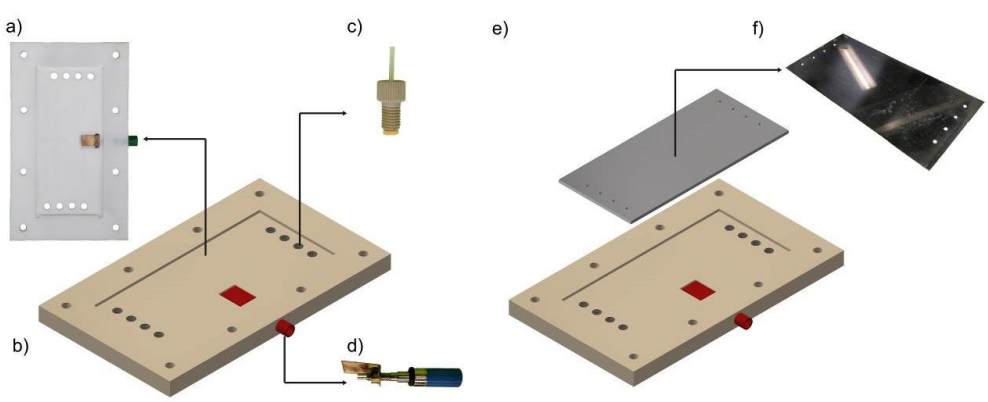

Figure 2.1 Individual parts of the electrochemical flow reactors: a) PTFE casing; b) electrode casing; c) Super Flangeless Fitting; d) electric contact; e) the electrode plate; f) electrode.

Flat rectangular-shaped plates (120 mm × 55 mm × 2 mm) were used as electrode material and could be readily fit into the PTFE casing. In order to avoid the use of complex and expensive electrodes (e.g. machined channels in the electrode plate), only small holes were drilled to establish the microfluidic connections. Between the electrodes, a PTFE gasket was placed which can be adjusted in thickness (dG = 0.25–0.5 mm are used in this manuscript) and shape, e.g. an open-channel gasket (110 mm length × 45 mm length) or an 8-channel gasket (106 mm length × 3 mm width per channel) (Figure 1.3 a–b).

Reactor characterization

During the course of our investigations, the 8-channel gasket was preferred as it enables a better fluid distribution over the electrodes and a narrower residence time distribution. In contrast, the open-channel configuration displayed bad mixing behavior and was not further pursued. Notably, using the 8-channel gasket (dG = 0.25 mm) equipped with stainless steel electrodes (SS), the reactor can be rapidly reconfigured giving access to a flexible reactor volume ranging from 88 µL/channel up to 704 µL when all channels are used in series (Figure

2.2). Furthermore, a result within the 88 µL reactor can be readily scaled by a factor of eight through use of all the channels in parallel (numbering-up). This flexibility in configuration is a unique feature of our reactor design providing rapid access to a wide variety of residence times and reaction scales in a single design.

To elucidate the average residence time in the individual reactor channels, flow rates ranging from 0.1 mL/min to 1.0 mL/min were evaluated. As shown in Figure 2.3, the volume of the individual channels averaged around 88 µL and 164 µL for the 0.25 mm and 0.5 mm thick gasket, respectively. The small differences between the channels can be attributed to the positioning of the flexible PTFE gasket upon closing the reactor. The standard deviation measured for both gaskets was below 10% (6.9% and 9.0% for the 0.25 mm and 0.5 mm thick gasket, respectively), which was considered acceptable.

Reactor performance

Next, we assessed the utility of this novel electrochemical flow reactor by examining its performance in two electrochemical transformations.

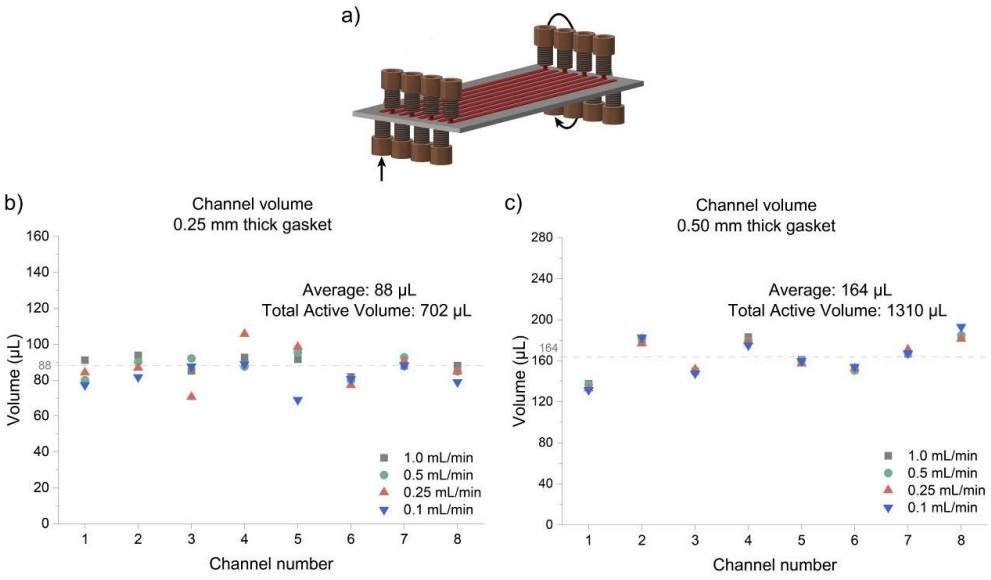

Figure 2.2 Reactor volume measurements at different flow rates. a) Schematic representation of the individual channels (in red in the figure); Obtained results for the b) 0.25 mm gasket; and the c) 0.50 mm gasket.

As a calibration point, we compared the performance of our novel reactor design with a commercial electrochemical flow reactor (i.e. Syrris Asia Flux) in the electrochemical oxidation of sulfides, a transformation previously reported by our laboratory.[65] This reaction is particularly interesting as the selectivity towards sulfoxide or sulfone is governed by the applied potential, while hydrogen reduction is observed as cathodic reaction. We recorded voltammograms for this transformation in the two reactors as shown in Figure 2.3. The voltammograms show two similar plateaus, indicating the oxidation towards sulfoxide (1-A) and sulfone (1-B) located respectively between 2.2–2.6 V and 3.3–3.5 V.[65]

In addition, during this experiment, the temperature of the reaction mixture was constantly monitored via a thermocouple at the outlet of the reactor.[66] The temperature remained constant during the entire experiment, which proves that our microreactor dissipates efficiently the generated heat to the environment.

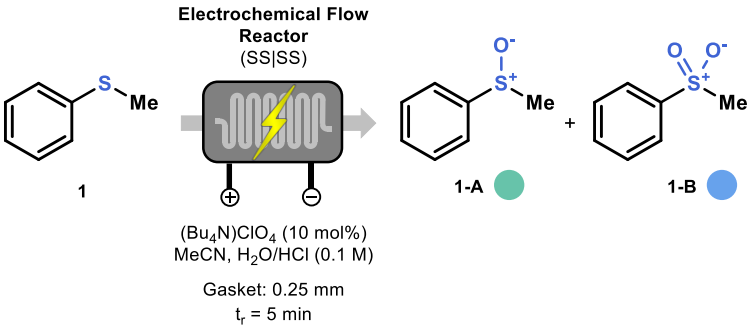

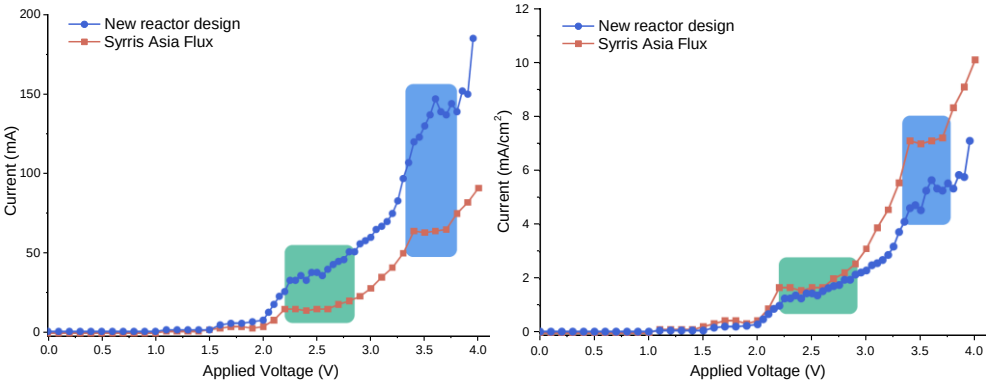

Figure 2.3 Voltammogram comparison for the electrochemical oxidation of thioanisole (1) to the corresponding sulfoxide (1-A) or sulfone (1-B), a with the newly developed electrochemical microreactor and the commercially available Syrris Asia Flux. The two voltammogram represent the same experiment, one with the measured current (b) and the other one with current per surface area.

Next, we carried out a systematic evaluation of different process parameters, i.e. residence time, gasket thickness and electrolyte concentration. The different reaction conditions are listed in Table 2.1.

For each of these conditions, we recorded a voltammogram which is shown in Figure 2.4. The same trend was observed in all cases, particularly at low voltages. The first plateau is visible in all the different experiments (green box, Figure 2.4), while the second plateau (blue box, Figure 2.4) is not visible at a higher electrolyte concentration (Experiment D). This effect is probably caused by a faster degradation of the electrode at higher voltage in the presence of a more conductive solution, corresponding to the higher increment of the current.

Table 2.1 Screening of different parameters (B: Residence Time, C: Gasket Thickness, D: Electrolyte)

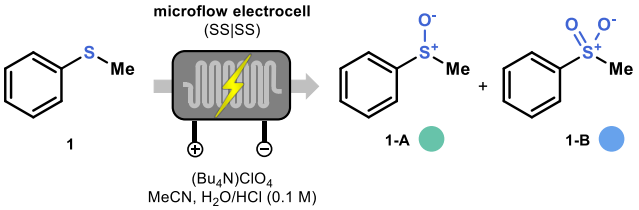

Experiment	Residence Time [min]	Gasket Thickness (d_G) [mm]	Electrolyte [mol%]
A	5	0.25	10
B	**10**	0.25	10
C	5	**0.50**	10
D	5	0.25	**100**

Reagents and conditions: Thioanisole (2 mmol, 0.1 M), Bu_4NClO_4 (10 mol% or 100 mol%), MeCN / HCl (20 mL, 3:1 v/v, with 0.1 M HCl in H_2O), stainless steel as anode/cathode, residence time: 5 min (at a flowrate of 0.15 mL min−1) or 10 min (at a flowrate of 0.075 mL min−1).

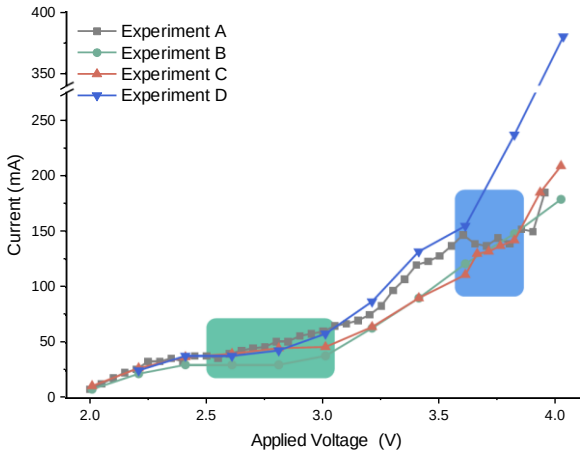

Figure 2.4 Comparison of different voltammograms for the electrochemical oxidation of thioanisole. For the different conditions, see Table 2.1.

Next, the conversion of thioanisole (1) to sulfoxide (1-A) and sulfone (1-B) at different cell voltages was investigated (Figure 2.5 a and b respectively). Experiments A, B and D follow the same trend, with a maximum conversion between 2.8 Vand 3.2 V for sulfoxide and at 3.6 V for sulfone. It should be noted that increasing amounts of electrolyte decreases the

sulfoxide yield (63%, Experiment D). Notably, increasing the residence time (Experiment B) results in a higher conversion to sulfoxide (1-A) at lower voltages. Furthermore, a thicker gasket clearly shifted the respective transformations to higher voltages, even if the voltammogram results were similar to the other experiments. This observation implies that indeed inter-electrode distance plays a key role in electrochemical transformations: not only does an increased inter-electrode distance result in a higher Ohmic resistance but it also exacerbates the mass transfer limitations.

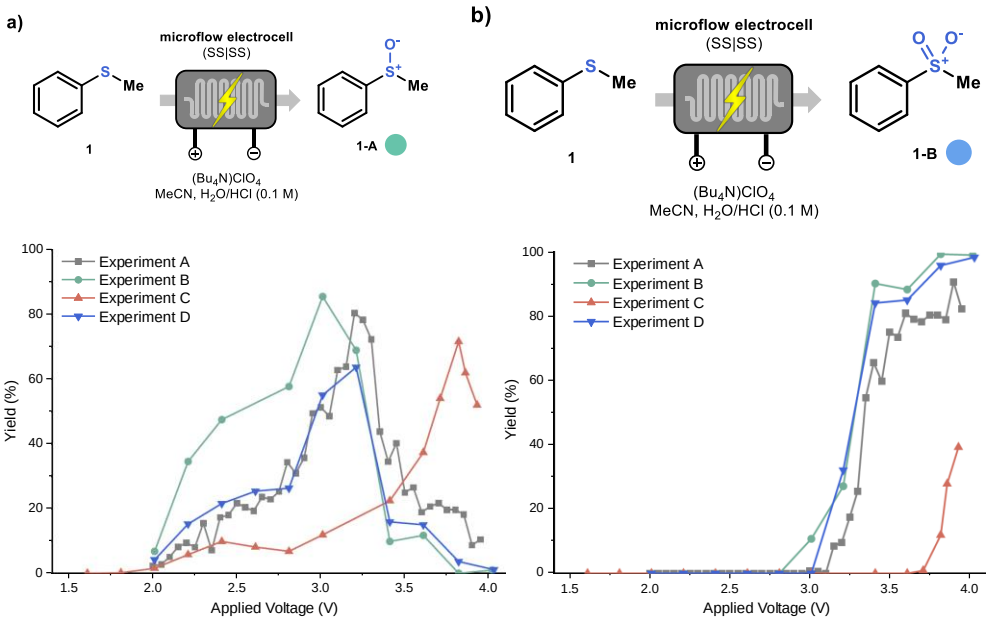

Figure 2.5 Comparison of the yield towards sulfoxide (1-A, a and sulfone (1-B, b for the electrochemical oxidation of thioanisole. For the different conditions, see Table 2.1. Yield etermined by GC-MS with biphenyl as internal standard.

Next, we decided to further explore the inter-dependency of residence time and applied voltage in Experiment B. Therefore, different residence times were evaluated at 2.8 V and 3.1 V respectively (Figure 2.6). At 3.1 V, the production of 1-A increases until about 5 min residence time. At higher residence times, the yield of 1-A drops and product 1-B is formed instead. Interestingly, at 2.8 V a similar trend is observed, with a shifted maximum yield for 1-A at 10 min, while prolonged reaction times affected negatively the selectivity. This result reveals a synergistic effect between reaction time and applied voltage.

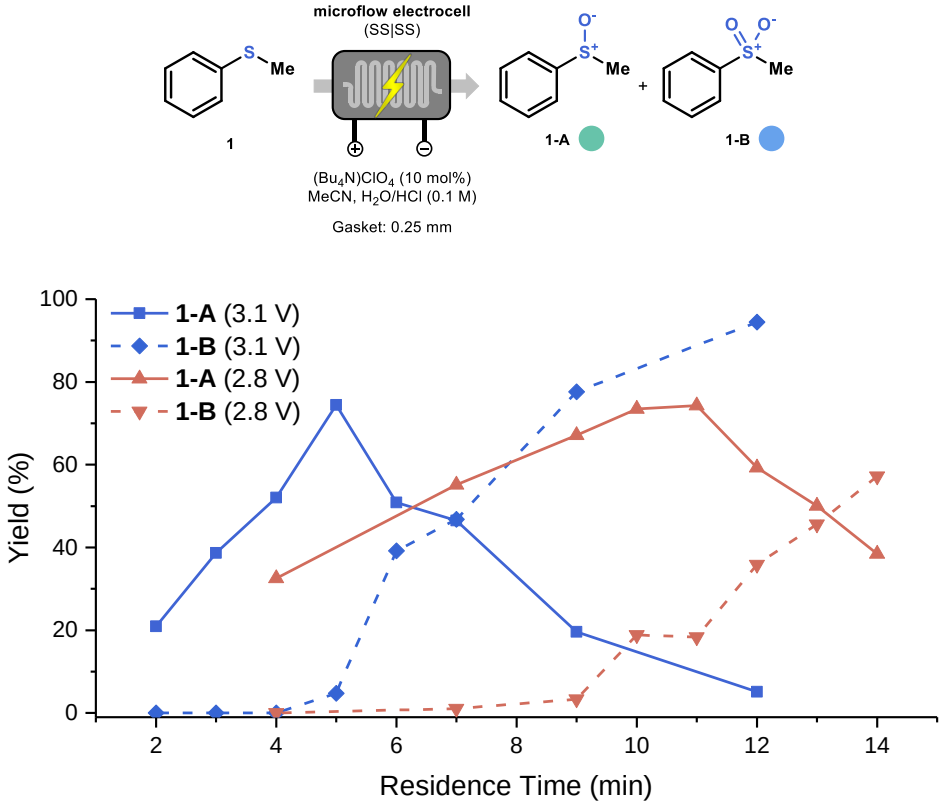

Figure 2.6 The relation between residence time and applied voltage and its impact on the electrochemical oxidation of thioanisole. Yield determined by GC-MS with biphenyl as internal standard.

Next, we set out to analyze the yield differences in the individual channels. A consistent performance is required in each channel if we want to use our reactor as a numbered-up device. Hereto, every channel was fed with the reaction mixture separately. We selected a short residence time of 1.75 min to maximize potential yield variations between the channels (Figure 2.7). To our delight, a consistent performance was observed in all the channels with an average conversion around 14.7% (line orange). Small yield differences can be attributed to the slight variations in channel volumes as discussed above. Notably, this result also demonstrates convincingly that the entire electrode surface is equally active and that the stainless steel electrodes are homogeneously polarized.

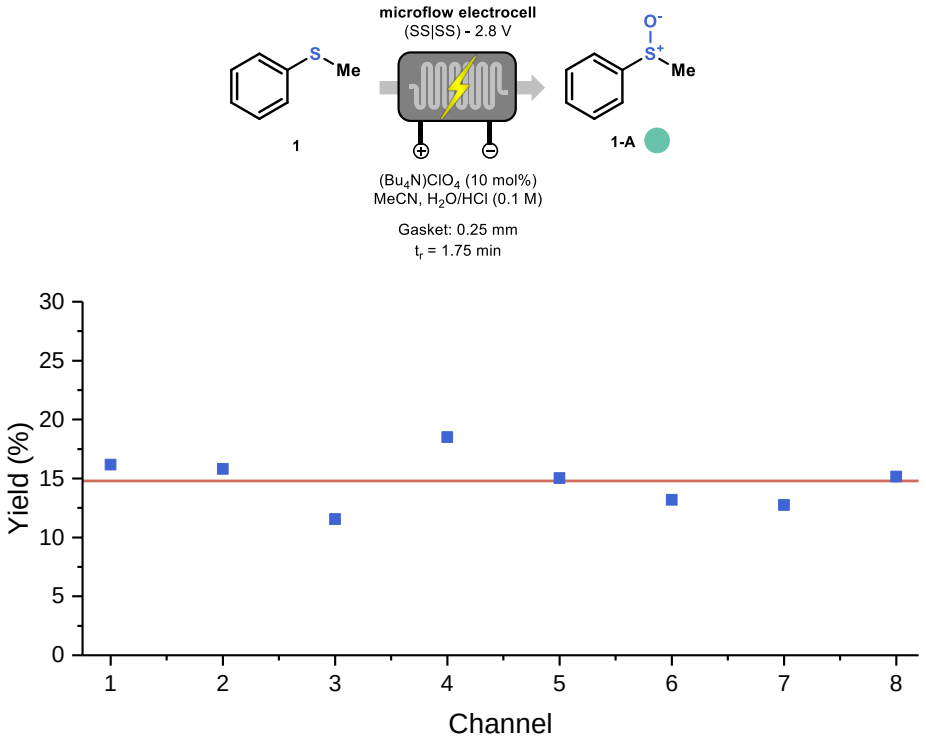

Figure 2.7 Relative deviations of the yield among the different channels in the electrochemical flow reactor. Yield determined by GC-MS with biphenyl as internal standard.

Next, we tested the electrochemical reactor in the serial mode by placing increasing numbers of channels in series. Using this strategy, the reactor volume can be systematically increased by 88 µL/channel, when a gasket of dG = 0.25 mm is used. The non-participating channels were filled with either reaction mixture or acetonitrile. As can be seen from Figure 2.8 a and b, the sulfoxide yield systematically increases with an increasing number of channels, while the current remained stable during the entire experiment when the non-participating channels were filled with reaction mixture (Figure 2.8 b). In contrast, when the non-participating channels were filled with solvent (Figure 2.8 c and d), an increase in current was detected when the number of channels filled with the reaction mixture was increased (Figure 2.8 d). The yield, however, increased similarly in both scenarios.

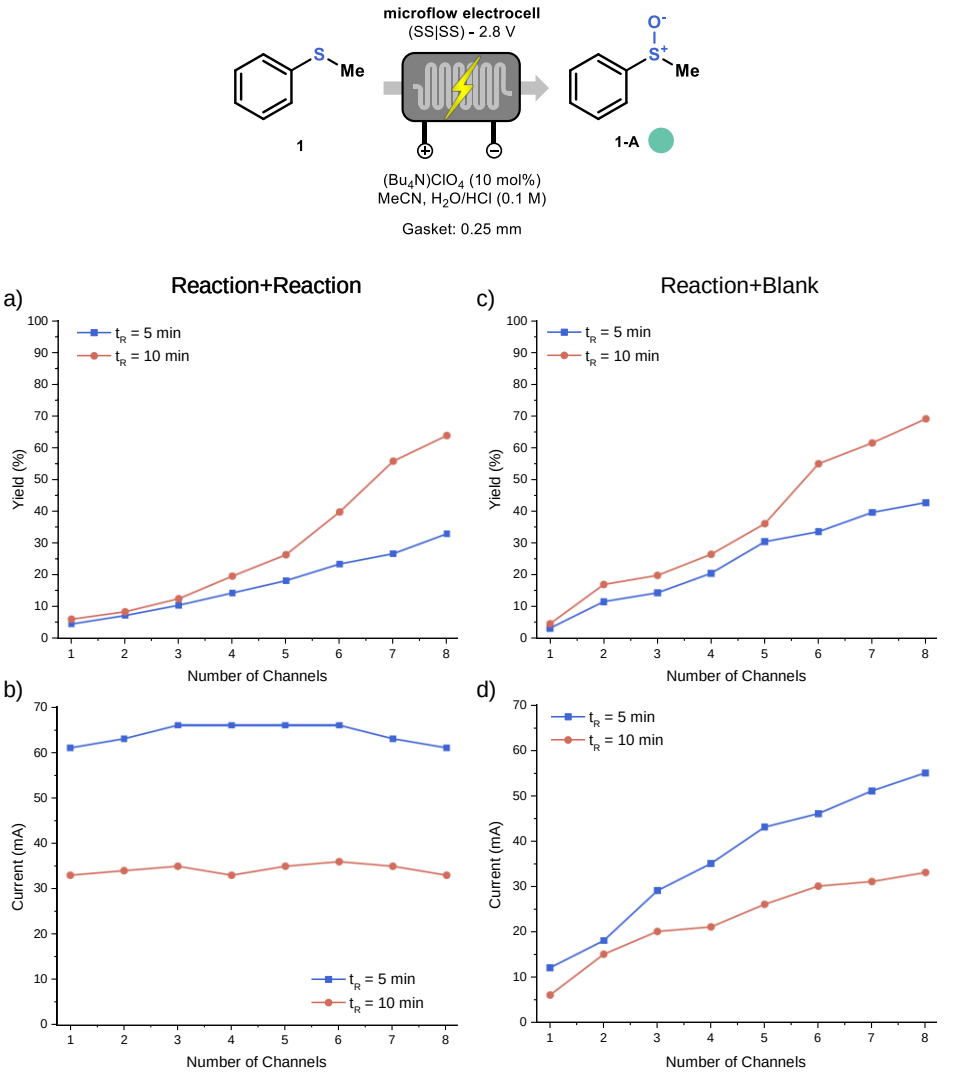

Figure 2.8 Experiment with gradually increasing channel numbers in series. The non-reactive channels are either filled with reaction mixture (a, b) or acetonitrile (c, d). Residence time refers to the 8-channel configuration (last data point in the graph). Yield determined by GCMS with biphenyl as internal standard.

Having established insight in the governing parameters, we set out to probe the synthetic utility of the electrochemical flow cell. The preparative synthesis of compounds 1-A and 1-B was carried out with the 8-channel configuration and the two products could be isolated with respective yields of 98% and 78% at a 6 mmol scale. Furthermore, the bioactive

molecule methionine sulfoxide could be isolated in a 42% yield using a 5 min residence time.

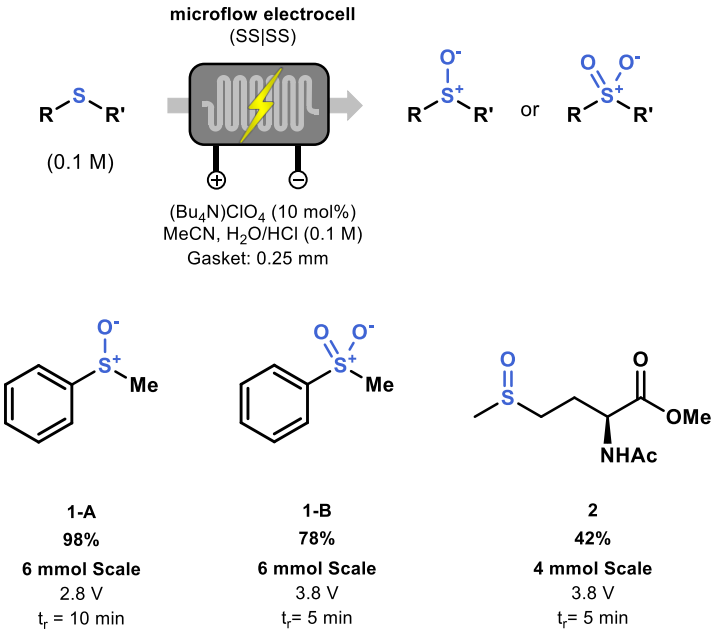

Scheme 2.1 Preparative scale of 1-A and 1-B and 2 via an electrochemical anodic oxidation of thioethers.

In order to further demonstrate the robustness of our electrochemical microreactor, we focused our attention on the electrochemical arene-phenol cross-coupling transformation as developed by Waldvogel et al. (Scheme 2.2).[28, 29] Employing the 8-channel configuration, the corresponding biaryl 5 was obtained in a 52% isolated yield on a 2.3 mmol scale. While slightly lower yields were obtained in comparison with the original report, we were able to use a cheap and easily accessible stainless steel anode instead of the more expensive boron doped diamond anode.[28, 29, 67]

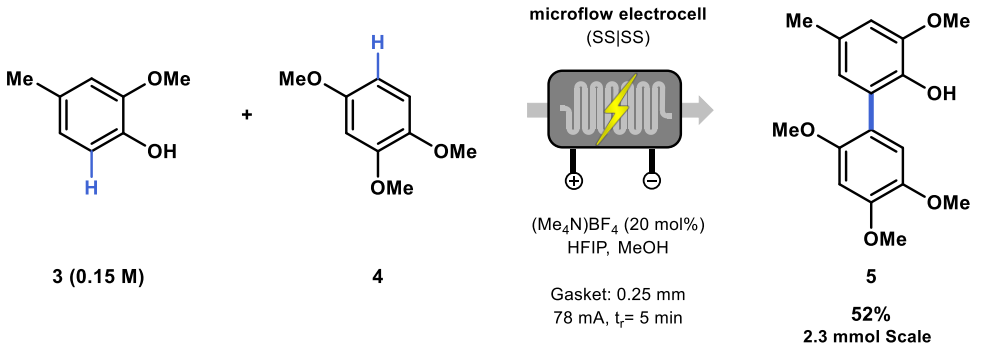

Scheme 2.2 Preparative scale of 5 via an electrochemical arenephenol cross coupling method.

2.3 Conclusion

Herein, we have described and validated a novel, undivided-cell electrochemical flow reactor. The reactor is modular and can be fabricated with straightforward machining techniques. A unique feature of this reactor is the flexible reactor volume which can be used in a serial (volume ranging from 88 µL/ channel up to 704 µL) or parallel mode (i.e. numbering-up). The electrochemical flow reactor was subsequently assessed in two synthetic transformations, which confirms its versatility and scale-up potential. Application of this reactor in other electrochemical transformations is currently pursued in our lab and will be reported in due course.

References

[1] Waldvogel SR, Lips S, Selt M, Riehl B, Kampf CJ (2018). Chem Rev 118:6706–6765

[2] Yan M, Kawamata Y, Baran PS (2018). Angew Chem Int Ed 57: 4149–4155

[3] Sauermann N, Meyer TH, Ackermann L (2018). Chem Eur J. 24: 16209-16217

[4] Wiebe A, Gieshoff T, Möhle S, Rodrigo E, Zirbes M, Waldvogel SR (2018). Angew Chem Int Ed 57:5594–5619

[5] Möhle S, Zirbes M, Rodrigo E, Gieshoff T, Wiebe A, Waldvogel SR (2018). Angew Chem Int Ed 57:6018–6041

[6] Echeverria PG, Delbrayelle D, Letort A, Nomertin F, Perez M, Petit L (2018). Aldrichimica Acta 51:3–19

[7] Yan M, Kawamata Y, Baran PS (2017). Chem Rev 117:13230–13319
[8] Sambiagio C, Sterckx H, Maes BUW (2017). ACS Cent Sci 3:686–688
[9] Horn EJ, Rosen BR, Baran PS (2016). ACS Cent Sci 2:302–308
[10] Nguyen H, Redden A, Moeller KD (2014). Green Chem 16:69–72
[11] Frontana-Uribe BA, Little RD, Ibanez JG, Palma A, VasquezMedrano R (2010). Green Chem 12:2099
[12] Yoshida J-i, Kataoka K, Horcajada R, Nagaki A (2008). Chem Rev 108:2265–2299
[13] Moeller KD (2000). Tetrahedron 56:9527–9554
[14] Degner D, in Topics in Current Chemistry, Vol. 148, 1988, pp. 1–95
[15] Tian C, Massignan L, Meyer TH, Ackermann L (2018). Angew Chem Int Ed 57:2383–2387
[16] Sauermann N, Mei R, Ackermann L (2018). Angew Chem Int Ed 57:5090–5094
[17] Qiu Y, Tian C, Massignan L, Rogge T, Ackermann L (2018). Angew Chem Int Ed 57:5818–5822
[18] Mei R, Sauermann N, Oliveira JCA, Ackermann L (2018). J Am Chem Soc 140:7913–7921
[19] Kawamata Y, Yan M, Liu Z, Bao DH, Chen J, Starr JT, Baran PS (2017). J Am Chem Soc 139:7448–7451
[20] Gieshoff T, Kehl A, Schollmeyer D, Moeller KD, Waldvogel SR (2017). J Am Chem Soc 139:12317–12324
[21] Fu N, Sauer GS, Saha A, Loo A, Lin S (2017). Science 357:575–579
[22] Horn J, Rosen BR, Chen Y, Tang J, Chen K, Eastgate MD, Baran PS (2016). Nature 533:77–81
[23] Herold S, Möhle S, Zirbes M, Richter F, Nefzger H, Waldvogel SR (2016). Eur J Org Chem 2016:1274–1278
[24] Hayashi R, Shimizu A, Yoshida JI (2016). J Am Chem Soc 138: 8400–8403
[25] O'Brien G, Maruyama A, Inokuma Y, Fujita M, Baran PS, Blackmond DG (2014). Angew Chem Int Ed 53:11868–11871
[26] Francke R, Little RD (2014). J Am Chem Soc 136:427–435
[27] Morofuji T, Shimizu A, Yoshida J-i (2013). J Am Chem Soc 135: 5000–5003
[28] Kirste A, Elsler B, Schnakenburg G, Waldvogel SR (2012). J Am Chem Soc 134:3571–3576

[29] Kirste A, Schnakenburg G, Stecker F, Fischer A, Waldvogel SR (2010). Angew Chem Int Ed 49:971–975

[30] Mihelcic J, Moeller KD (2003). J Am Chem Soc 125:36–37

[31] Slomczynska U, Chalmers DK, Cornille F, Smythe ML, Beusen DD, Moeller KD, Marshall GR (1996). J Org Chem 61:1198–1204

[32] Pletcher D, Green RA, Brown RCD (2018). Chem Rev 118: 4573–4591

[33] Gérardy R, Emmanuel N, Toupy T, Kassin V-E, Tshibalonza NN, Schmitz M, Monbaliu J-CM (2018). Eur J Org Chem 2018:2301–2351

[34] Atobe M, Tateno H, Matsumura Y (2018). Chem Rev 118: 4541–4572

[35] Mitsudo K, Kurimoto Y, Yoshioka K, Suga S (2017). Chem Rev 118:5985–5999

[36] Folgueiras-Amador A, Wirth T (2017). J Flow Chem 7:94–95

[37] Watts K, Baker A, Wirth T (2015). J Flow Chem 4:2–11

[38] Roth P, Stalder R, Long TR, Sauer DR, Djuric SW (2013). J Flow Chem 3:34–40

[39] Yoshida J-I (2010). ChemInform 41:40–45

[40] Ahmed-Omer B, Brandt JC, Wirth T (2007). Org Biomol Chem 5: 733–740

[41] Zhao F, Cambié D, Hessel V, Debije MG, Noel T (2018). Green Chem 20:2459–2464

[42] Kuijpers KPL, Bottecchia C, Cambié D, Drummen K, König NJ, Noël T (2018). Angew Chem Int Ed 57:11278–11282

[43] Cambié D, Zhao F, Hessel V, Debije MG, Noël T (2017). Angew Chem Int Ed 56:1050–1054

[44] Straathof NJW, Su Y, Hessel V, Noël T (2015). Nat Protoc 11:10–21

[45] Laudadio G, Govaerts S, Wang Y, Ravelli D, Koolman H, Fagnoni M, Djuric S, Noel T (2018). Angew Chem Int Ed 57:4078–4082

[46] Casnati A, Gemoets HPL, Motti E, Della Ca' N, Noël T (2018). Chem Eur J 24:14079–14083

[47] Borukhova S, Noël T, Hessel V (2016). Org Process Res Dev 20: 568–573

[48] Gemoets PL, Hessel V, Noël T (2014). Org Lett 16:5800–5803

[49] Wolf M, McQuitty S (2011). AMS Rev 1:154–170

[50] Kockmann N, Thenée P, Fleischer-Trebes C, Laudadio G, Noël T (2017). React Chem Eng 2:258–280

[51] Hardwick T, Ahmed N (2018). RSC Adv 8:22233–22249

[52] Plutschack MB, Pieber B, Gilmore K, Seeberger PH (2017). Chem Rev 117:11796–

11893

[53] Noël T, Su Y, Hessel V (2015) Top Organomet Chem, Vol. 57, pp 1–41

[54] Gutmann B, Cantillo D, Kappe CO (2015). Angew Chem Int Ed 54:6688–6728

[55] Gütz C, Stenglein A, Waldvogel SR (2017). Org Process Res Dev 21:771–778

[56] Green RA, Jolley KE, Al-Hadedi AAM, Pletcher D, Harrowven DC, De Frutos O, Mateos C, Klauber DJ, Rincón JA, Brown RCD (2017). Org Lett 19:2050–2053

[57] Folgueiras-Amador A, Philipps K, Guilbaud S, Poelakker J, Wirth T (2017). Angew Chem Int Ed 56:15446–15450

[58] Gütz C, Klöckner B, Waldvogel SR (2016). Org Process Res Dev 20:26–32

[59] Watts K, Gattrell W, Wirth T (2011). Beilstein J Org Chem 7:1108–1114

[60] Yoshida J.-i (2005). Chem Commun (Cambridge, U K):4509

[61] Horcajada R, Okajima M, Suga S, Yoshida J.-i (2005). Chem Commun (Cambridge, U K):1303

[62] Küpper M, Hessel V, Löwe H, Stark W, Kinkel J, Michel M, Schmidt-Traub H (2003). Electrochim Acta 48:2889–2896

[63] Kuijpers PL, van Dijk MAH, Rumeur QG, Hessel V, Su Y, Noël T (2017). React Chem Eng 2:109–115

[64] Su Y, Kuijpers K, Hessel V, Noël T (2016). React Chem Eng 1:73–81

[65] Laudadio G, Straathof NJW, Lanting MD, Knoops B, Hessel V, Noël T (2017). Green Chem 19:4061–4066

[66] Laudadio G, Gemoets HPL, Hessel V, Noël T (2017). J Org Chem 82:11735–11741

[67]. Wiebe A, Riehl B, Lips S, Franke R, Waldvogel SR (2017). Sci Adv 3:1–8

CHAPTER 3

Accelerating sulfonyl fluoride electrosynthesis in flow

This chapter is based on:

Cao, Y.; Adriaenssens, B.; de A. Bartolomeu, A.; Laudadio, G.; de Oliveira, K. T. and Noël, T. Accelerating Sulfonyl Fluoride Synthesis through Electrochemical Oxidative Coupling of Thiols and Potassium Fluoride in Flow. *Journal of Flow Chemistry* **2020**, 10, 191-197.

Abstract

Sulfonyl fluorides are valuable synthetic motifs which are currently of high interest due to the popularity of the sulfur (VI) fluoride exchange (SuFEx) click chemistry concept. Herein, we describe a flow chemistry approach to enable their synthesis through an electrochemical oxidative coupling of thiols and potassium fluoride. The reaction can be carried out at room temperature and atmospheric pressure and the yield of the targeted sulfonyl fluoride, by virtue of the short inter-electrode distance between a graphite anode and a stainless-steel cathode, reached up to 92% in only 5 min residence time compared to 6 to 36 h in batch. A diverse set of thiols (7 examples) was subsequently converted in flow. Finally, a fully telescoped process was developed which combines the electrochemical sulfonyl fluoride synthesis with a follow-up SuFEx reaction.

3.1 Introduction

Click chemistry is a popular synthetic concept which enables the quick and reliable stitching of two molecular building blocks in high yield and selectivity. The concept has been coined by K.B. Sharpless[1] and has been widely employed in drug discovery[2], chemical biology, and material science as it is amenable to high-throughput experimentation. In general, click chemistry is a collection of synthetic methods that are high yielding, fast, easy to perform and produce little to no byproducts. One of the most popular click reactions is the Cu(I)-catalyzed azide-alkyne cycloaddition which yields triazoles.[3] More recently, a new click reaction was developed by Sharpless and coworkers, i.e. sulfur (VI) fluoride exchange (SuFEx) which employs sulfonyl fluorides as stable and robust reagents.[4]

Key to the success of the click chemistry concept is the access to a broad array of structurally diverse click reagents in large quantities.[5] It is general belief that flow chemistry can be particularly helpful in realizing this objective. As an example, the synthesis of azides has been reported by many research groups and has been successfully coupled with the follow-up Cu(I)-catalyzed azide-alkyne cycloaddition (CuAAC).[6–10] The combination of these two steps leads to a significant time reduction and keeps the total inventory of hazardous azides low, thus effectively reducing the safety risks associated with these reagents.[11] Moreover, the use of superheated reaction conditions in combination with copper-based capillaries allows to further reduce the reaction time effectively.[12] Removal of the homogeneous Cu(I)-catalyst can also be achieved in flow leading to almost pure triazole compounds, which meet the stringent product purity requirements needed in the pharmaceutical industry.[13, 14]

While the CuAAC has served as a benchmark reaction for flow chemistry in the past two decades, SuFEx has received much less scrutiny. Recently, our group developed an electrochemical approach to access the key sulfonyl fluoride starting materials.[15] The method involves an anodic oxidation process and uses widely available thiols or disulfides and KF as a cheap, safe and widely available fluorine source. Biphasic reaction conditions (acetonitrile/1 M HCl) are required and the reaction was carried out in batch. However, preliminary studies showed that the use of flow chemistry was of great benefit.[16–20] The reaction time could be reduced to the minute range in flow and no mass transfer limitations

were observed. The reduced reaction time can be attributed to (i) the increased electrode surface-to-volume ratio, (ii) a high interfacial area between the organic and aqueous phase, and (iii) intensified mass transport due to multiphase fluid patterns.

In this manuscript, we provide a full investigation of all relevant process parameters in the flow-enabled electrochemical oxidative coupling of thiols and fluoride yielding sulfonyl fluorides. Moreover, we have for the first time coupled the sulfonyl fluoride synthesis with a subsequent SuFEx click reaction in flow, which represents a particularly useful strategy to handle the most volatile sulfonyl fluoride reagents.

3.2 Results and discussion

Initial experiments were carried out with thiophenol as the benchmark substrate and KF as the fluoride source (Scheme 3.1). It should be noted that all experiments described in this paper are carried out in a home-built electrochemical flow reactor (Figure 1.1).[21] At the cathode, hydrogen is generated as a benign and high value byproduct. In such a scenario, electrodes with a low hydrogen overpotential are typically preferred, e.g. platinum, copper or stainless steel.[22] From our previous experiments in batch, we found that a graphite anode and a stainless steel cathode worked optimal and this proved to be also the case in our flow experiments (Table 3.1, Entry 1). Other electrode materials as cathode, such as copper, graphite or nickel, did not lead to any improvement (Table 3.1, Entries 2–4).

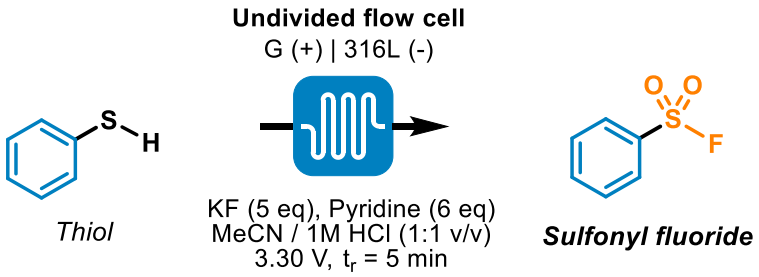

Scheme 3.1 Electrochemical oxidative coupling of thiophenol and KF in flow as a benchmark reaction. The reaction conditions displayed are the optimized parameters.

Table 3.1 Evaluation of different cathode materials in the electrochemical sulfonyl fluoride synthesis in flow.[a]

Entry	Counter electrode (cathode)	Yield (%)[b]
1	**stainless steel**	**92**
2	copper	38
3	graphite	55
4	nickel	46

[a] Reaction conditions: 0.1 M thiophenol, 0.6 M pyridine, 0.5 M KF, 3.30 V, 1 M HCl/CH_3CN (1:1 v/v), total flow rate 150 μL/min, residence time 5 min, graphite anode. [b] GC-yield using GC-FID using an internal standard calibration method (biphenyl).

Next, we investigated the influence of the solvent system (Table 3.2). As the organic phase, acetonitrile was selected as the optimal solvent. Lower yields for the target product were obtained in other common organic solvents, such as THF or methanol (Table 3.2, Entries 6–7). The presence of acid provided in general higher yields compared to non-acidic reaction mixtures (Table 3.2, Entry 1). However, the presence of sulfuric acid proved to be detrimental for the reaction as no product formation was observed (Table 3.2, Entry 2).

Next, we investigated the influence of the fluoride source on the reaction outcome (Table 3.3). As shown in our previous work,[15] the reaction worked well with alkali fluorides but also with Selectfluor. The use of Selectfluor was not further considered due to low atom efficiency and its higher price compared to alkali fluorides. The reaction worked best with 5 equivalents of KF (Table 3.3, Entry 4). While only one equivalent is needed for the reaction, the remaining 4 equivalents served as a cheap supporting electrolyte. Increasing the amount of KF did not lead to further improvements (Table 3.3, Entries 6–7).

The electrochemical oxidative coupling of thiols and potassium fluoride requires the addition of pyridine to obtain high yields. It is possible that pyridine functions either as an electron mediator[23] or a as phase transfer catalyst. From our mechanistic investigations,[15] we believe that at least pyridine functions partly as a phase transfer catalyst (Table 3.4). Screening the concentration of pyridine, we found that the best results were obtained with 0.6–0.7 M

pyridine (Table 3.4, Entries 6 and 9). Other phase transfer catalysts, such as tetrabutylammonium bromide and chloride were less effective (Table 3.4, Entries 7–8).

Table 3.2 Influence of the solvent system on the electrochemical sulfonyl fluoride synthesis in flow.[a]

Entry	Aqueous solvent	Organic solvent	Yield (%)[b]
1	H_2O	CH_3CN	78
2	0.5 M H_2SO_4	CH_3CN	--
3	0.6 M HCl	CH_3CN	81
4	0.8 M HCl	CH_3CN	84
5	**1.0 M HCl**	**CH_3CN**	**92**
6	1.0 M HCl	THF	39
7	1.0 M HCl	CH_3OH	33
8	1.2 M HCl	CH_3CN	62
9	1.4 M HCl	CH_3CN	50

[a] Reaction conditions: 0.1 M thiophenol, 0.6 M pyridine, 0.5 M KF, 3.30 V, inorganic solvent/organic solvent (1:1 v/v), total flow rate 150 μL/min, residence time 5 min, graphite anode and stainless steel cathode [b] GC-yield using GC-FID with internal standard (biphenyl).

Electrochemical transformations can be carried out either potentiostatic (constant potential) or galvanostatic (constant current). Under both scenarios, excellent yields could be obtained in flow as can been seen from Figure 3.1. However, the highest yield and the most stable operation was observed under potentiostatic reaction conditions with GC yields up to 92%. Galvanostatic reactions provide a constant current and thus the reaction rate is constant until complete conversion is obtained. In contrast, potentiostatic operation keeps the cell potential constant and is of high interest to obtain high and tunable reaction selectivity.[24] While galvanostatic operation is preferred in batch, potentiostatic reaction conditions in flow are in our experience equally fast.[25, 26] We believe this has to do with the fact that the conversion increases along the channel length and thus a constant supply of electrons is maintained the entire time. Indeed, during a four-hour stability test, we saw that the current remained

constant between 400 and 500 mA (Figure 3.2). This is in contrast with batch potentiostatic experiments where the supply of electrons decreases when the conversion increases (less product needs to be converted, thus higher potential and lower current). This leads to slower reaction rates towards the end of the reaction and thus full conversion is harder to reach. In batch, this is often solved by adding large amounts of supporting electrolyte.

Table 3.3 Amount of fluoride needed for the electrochemical sulfonyl fluoride synthesis in flow.[a]

Entry	Fluoride source	Yield (%)[b]
1	0.1 M KF	23
2	0.3 M KF	71
3	**0.5 M KF**	**92**
4	0.5 M NaF	--
5	0.5 M CsF	67
6	0.7 M KF	65
7	0.9 M KF	54

[a] Reaction conditions: 0.1 M thiophenol, 0.6 M pyridine, 3.30 V, 1 M HCl / CH_3CN (1:1 v/v), total flow rate 150 µL/min, residence time 5 min, graphite anode and stainless steel cathode. [b] GC-yield using GC-FID with internal standard (biphenyl).

While the reaction required 24–36 h in batch to reach full conversion,[15] the reaction can be completed in only 5 min in flow (Figures 3.3 and 3.4). Such intensified reaction conditions can be attributed to the short diffusion distances to the electrode surface, the intensified mass transport due to multiphase flow patterns and the increased interfacial area.

Next, we investigated the scalability of our flow protocol. Since electrochemical transformations are surface reactions, scale-up in batch can be regarded as very challenging. Typically, the electrode size is increased, and larger amounts of supporting electrolyte are required to cope with the increase in Ohmic drop. Therefore, nearly all industrial electrochemical processes are carried out as flow processes in narrow-gap cells (inter-electrode gap = 0.5–10 mm) which are numbered up depending on the targeted throughput.[16]

Table 3.4 Importance of the Phase Transfer Catalyst in the electrochemical sulfonyl fluoride synthesis in flow.[a]

Entry	Phase Transfer Catalyst	Yield (%)[b]
1	0.1 M pyridine	60
2	0.2 M pyridine	67
3	0.3 M pyridine	78
4	0.4 M pyridine	83
5	0.5 M pyridine	87
6	**0.6 M pyridine**	**92**
7	0.6 M n-Bu_4NBr	35
8	0.6 M n-Bu_4NCl	66
9	0.7 M pyridine	91
10	0.8 M pyridine	85

[a] Reaction conditions: 0.1 M thiophenol, 0.5 M KF, 3.30 V, 1 M HCl / CH_3CN (1:1 v/v), total flow rate 150 µL/min, residence time 5 min, graphite anode and stainless steel cathode.
[b] GC-yield using GC-FID with internal standard (biphenyl).

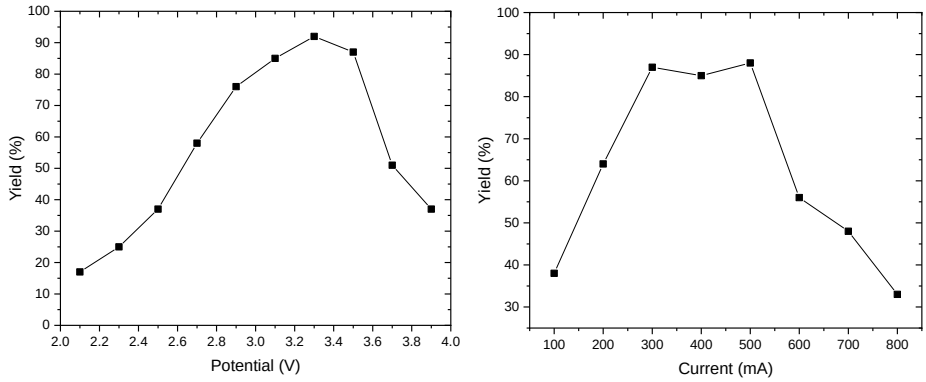

Figure 3.1 Electrochemical sulfonyl fluoride synthesis in flow. (left) Potentiostatic reaction conditions, (right) galvanostatic reaction conditions. GC-yield using GC-FID with internal standard (biphenyl).

As can be seen from Figure 3.4, the GC and isolated yields remained constant from 2 mmol to 10 mmol scale, showing proof that the reaction is scalable but also provides stable output for longer periods of time.

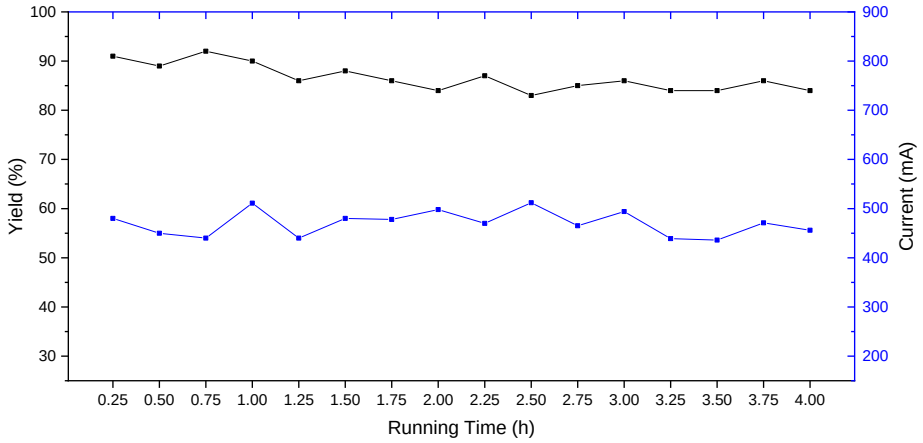

Figure 3.2 Stability test (4 h operation time) for the reaction (conditions are those from Scheme 3.1) with a 5 min residence time. GC-yield using GC-FID with internal standard (biphenyl).

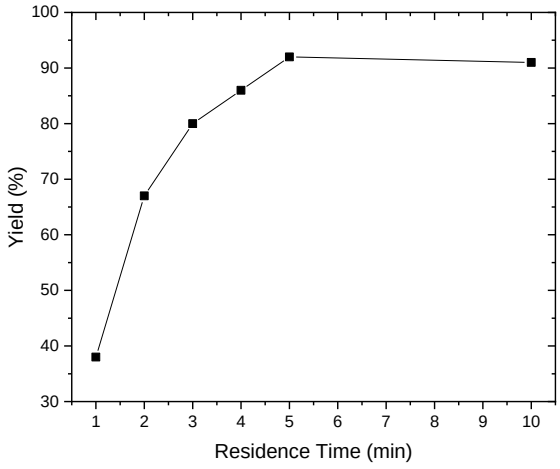

Figure 3.3 Influence of the residence time on the electro-oxidative fluorination of thiophenol to benzenesulfonyl fluoride. GC-yield using GC-FID with internal standard (biphenyl).

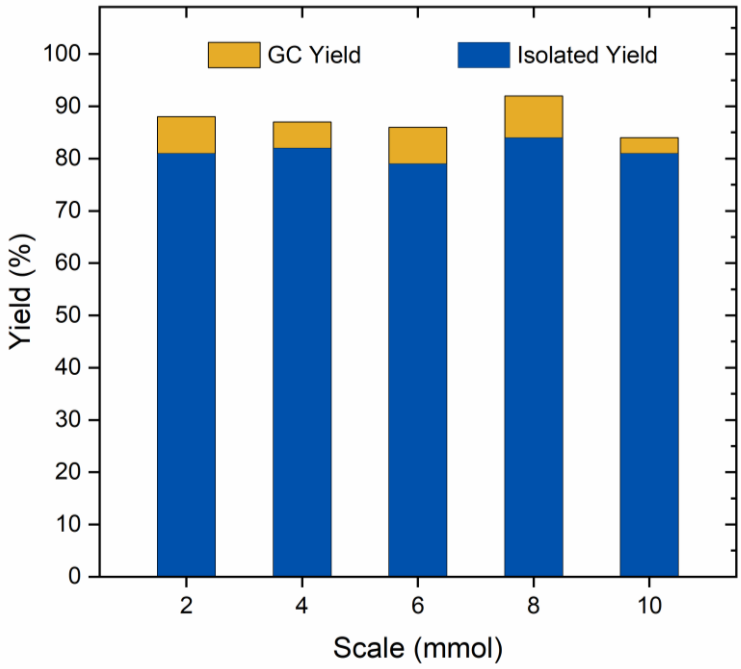

Figure 3.4 Scale-up test (2 mmol to 10 mmol scale) for the reaction with 5 min residence time. Conditions, see Scheme 3.1. Yields reported are those of isolated products.

With the optimal reaction conditions in hand, we commenced evaluating the flow protocol for the conversion of a diverse set of thiols (Scheme 3.2). In most scenarios, the yields were comparable with the batch protocol. It should be noted that no individual optimization was carried out, this explains that in some cases a slightly lower yield was obtained compared to individually optimized batch examples. Nevertheless, the results shown in Scheme 3.2 show clearly that the batch protocols can be seamlessly translated to flow.

Some of the corresponding sulfonyl fluorides presented in Scheme 3.2 are volatile and therefore difficult to isolate on small scale. Immediate conversion of these compounds in a followup SuFEx-type transformation is therefore recommended. In flow, this can be easily achieved by combining the individual steps in a single, uninterrupted flow protocol.[27] Hereto, the sulfonyl fluoride product (92% GC yield, 82% isolated yield) exiting the electrochemical reactor is first quenched with a saturated $NaHCO_3$ solution as the SuFEx reaction requires to

be carried out at neutral pH (Scheme 3.3). Sampling points were added in our design to verify the yield of the sulfonyl fluoride (Scheme 3.3, Sampling point 1) and the pH (Scheme 3.3, Sampling point 2). Next, the neutralized reaction stream was merged with a reagent stream containing phenol and a stream containing additional Cs_2CO_3. Within 30 s, we observed a clean conversion to the corresponding phenyl sulfonate derivative (73% isolated yield) using this telescoped flow process. Moreover, this example highlights the clear advantage of combining the reagent synthesis and the subsequent SuFEx click reaction in a telescoped fashion in terms of isolation, time and labor reduction. Further, we believe this process should be amenable to applications in high throughput experimentation.[28, 29]

Scheme 3.2 Flow synthesis of sulfonyl fluorides and comparison with the batch protocol. Reaction conditions in flow: 0.1 M thiol, 0.6 M pyridine, 0.5 M KF, 3.30 V, 1 M HCl/ CH_3CN (1:1 v/v), total flow rate 150 µL/min, residence time 5 min; Reaction conditions in batch: 2 mmol thiol, 10 mmol KF, 8 mmol pyridine, 10 mL CH_3CN, 10 mL 1 M HCl, 3.20 V. Yields reported are those of isolated products.

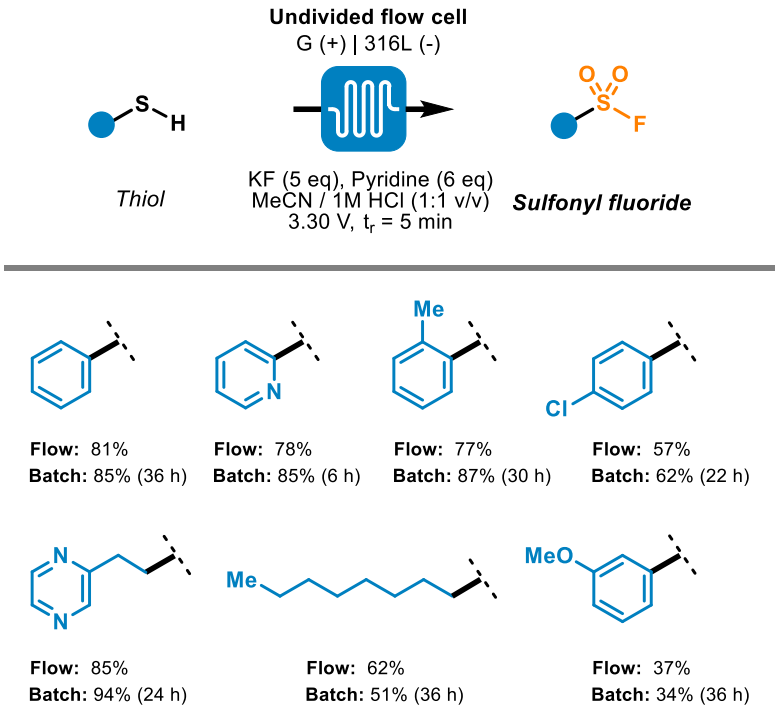

Scheme 3.3 Multistep reaction sequence in flow combining the electrochemical sulfonyl fluoride synthesis with the follow-up SuFEx reaction to yield phenyl sulfonate derivatives.

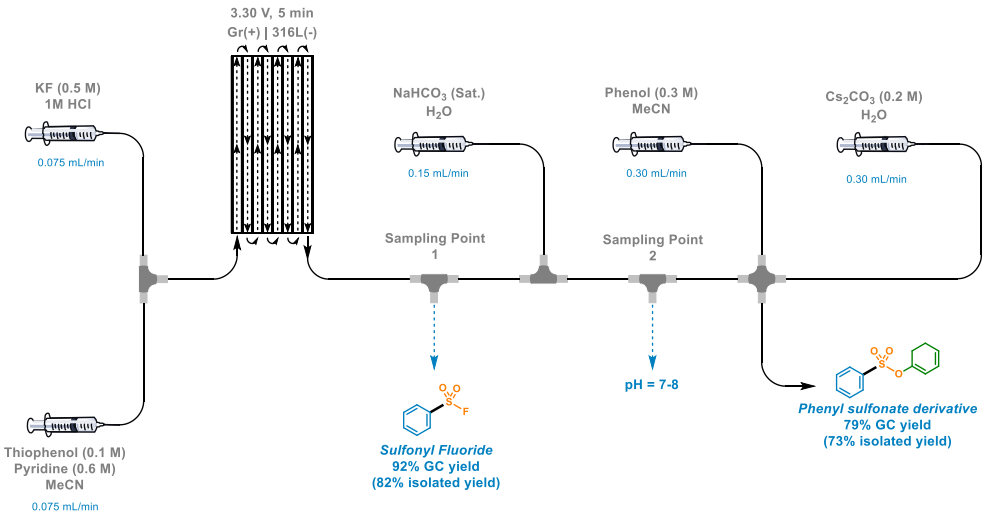

In conclusion, a continuous-flow protocol for the electrochemical oxidative coupling of thiols and KF to prepare sulfonyl fluorides was developed. The flow protocol leads to significant shorter reaction times (5 min in flow vs. 6–36 h in batch) and proves to be scalable (up to 10 mmol). Moreover, the flow sulfonyl fluoride synthesis can be readily telescoped into a SuFEx follow up reaction, without the need for intermediate purification. Ultimately, we believe that this flow protocol will be useful for those in academia and industry, interested in SuFEx click chemistry.

References

[1] Kolb HC, Finn MG, Sharpless KB (2001). Angew Chemie Int Ed 40:2004–2021

[2] Noël T, Cao Y, Laudadio G (2019). Acc Chem Res 52:2858–2869

[3] Borukhova S, Noël T, Metten B, de Vos E, Hessel V (2013). ChemSusChem 6:2220–2225

[4] Cao Y, Noël T (2019). Org Process Res Dev 23:403–408

[5] Bogdan AR, Sach NW (2009). Adv Synth Catal 351:849–854

[6] Varas AC, Noël T, Wang Q, Hessel V (2012). ChemSusChem 5:1703–1707

[7] Vural Gürsel I, Aldiansyah F, Wang Q, Noël T, Hessel V (2015). Chem Eng J 270:468–

475
[8] Pletcher D, Green RA, Brown RCD (2018). Chem Rev 118:4573–4591
[9] Atobe M, Tateno H, Matsumura Y (2018). Chem Rev 118:4541–4572
[10] Mitsudo K, Kurimoto Y, Yoshioka K, Suga S (2018). Chem Rev 118:5985–5999
[11] Laudadio G, de Smet W, Struik L, Cao Y, Noël T (2018). J Flow Chem 8:157–165
[12] Thirumurugan P, Matosiuk D, Jozwiak K (2013). Chem Rev 113:4905–4979
[13] Folgueiras-Amador AA, Wirth T (2017). J Flow Chem 7:94–95
[14] Couper AM, Pletcher D, Walsh FC (1990). Chem Rev 90:837–865
[15] Francke R, Little RD (2014). Chem Soc Rev 43:2492–2521
[16] Laudadio G, Straathof NJW, Lanting MD, Knoops B, Hessel V, Noël T (2017). Green Chem 19:4061–4066
[17] Laudadio G, Barmpoutsis E, Schotten C, Struik L, Govaerts S, Browne DL, Noël T (2019a). J Am Chem Soc 141:5664–5668
[18] Pieber B, Gilmore K, Seeberger PH (2017). J Flow Chem 7:129–136
[19] Fleming GS, Beeler AB (2017). J Flow Chem 7:124–128
[20] Mennen SM, Alhambra C, Allen CL, Barberis M, Berritt S, Brandt TA, Campbell AD, Castañón J, Cherney AH, Christensen M, Damon DB, Eugenio de Diego J, García-Cerrada S, García-Losada P, Haro R, Janey J, Leitch DC, Li L, Liu F, Lobben PC, MacMillan DWC, Magano J, McInturff E, Monfette S, Post RJ, Schultz D, Sitter BJ, Stevens JM, Strambeanu II, Twilton J, Wang K, Zajac MA (2019). Org Process Res Dev 23:1213–1242
[21] Liang L, Astruc D (2011). Coord Chem Rev 255:2933–2945
[22] Dong J, Krasnova L, Finn MG, Sharpless KB (2014). Angew Chemie Int Ed 53:9430–9448
[23] Meng G, Guo T, Ma T, Zhang J, Shen Y, Sharpless KB, Dong J (2019). Nature 574:86–89
[24] Hatit MZC, Reichenbach LF, Tobin JM, Vilela F, Burley GA, Watson AJB (2018). Nat Commun 9:4021
[25] Kockmann N, Thenée P, Fleischer-Trebes C, Laudadio G, Noël T (2017). React Chem Eng 2:258–280
[26] Fuchs M, Goessler W, Pilger C, Kappe CO (2010). Adv Synth Catal 352:323–328
[27] Bogdan AR, James K (2010). Chem – A Eur J 16:14506–14512
[28] Borukhova S, Noël T, Metten B, de Vos E, Hessel V (2016). Green Chem 18:4947–

4953

[29] Laudadio G, Bartolomeu A de A, Verwijlen LMHM, Cao Y, de Oliveira KT, Noël T (2019b). J Am Chem Soc 141:11832–11836

CHAPTER 4

Efficient electrocatalytic reduction of furfural to furfuryl alcohol

This chapter is based on:

Cao, Y. and Noël, T. Efficient Electrocatalytic Reduction of Furfural to Furfuryl Alcohol in a Microchannel Flow Reactor. *Organic Process Research & Development* **2019**, 23 (3), 403-408.

Abstract

Furfural is considered to be an essential biobased platform molecule. Recently, its electrocatalytic hydrogenation is regarded as a more environmentally friendly process compared to traditional catalytic hydrogenation. In this study, a new, continuous-flow approach enabling furfural electrocatalytic reduction was developed. In an undivided multichannel electrochemical flow reactor at ambient temperature and pressure in basic reaction conditions, the yield of furfuryl alcohol reached up to 90% in only 10 min residence time. Interestingly, the faradaic efficiency was 90%, showing a good effectiveness of the consumed electrons in the generation of the targeted compound. Furthermore, the innovation lies in the direct electrolysis using the green solvent ethanol without the need for membrane separation or catalyst modification, which offers further proof for continuous and sustainable production in industry.

4.1 Introduction

Furfural is one of the most significant industrial biobased chemicals, which is obtained via dehydration of sugars, as obtained from a variety of agricultural products such as corncobs and wheat bran.[1] It possesses extensive application prospects as a renewable, nonpetroleum-based platform molecule.[1–6] Consequently, furfuryl alcohol is widely used as a monomer for the synthesis of furan resins.[5] These polymers are used in thermoset polymer matrix composites, cements, adhesives, and coatings. It is also recognized as a valuable intermediate in the fields of agriculture, medicine, and dyes.[6] Compared to conventional high-pressure hydrogenation processes, the electrolysis of furfural offers not only a promotion for agricultural waste utilization[7] but also constitutes an energy-saving green process.[8] Li's group recently reported an interesting electrocatalytic reduction of furfural to furfuryl alcohol in a divided cell using a cation exchange membrane.[9] Recently, Koper et al. reviewed the state of the art for furfural electroreduction.[10] The majority of the electrochemical reduction reactions were performed either with noble metal catalysts in batch electrochemical cells or required long residence times in flow-through electrochemical cells.[11] Arguably, the remaining problems lie in the discontinuity of the batch process, the complexity of the utilized electrodes, and the limitation of the use of divided cells.

The electrocatalytic reduction is an intriguing example which enables the hydrogenation of molecules using adsorbed hydrogen at the electrode which originates from H+ or H_2O via the Volmer reaction (Scheme 4.1).[12] Hence, the reaction can be carried out at very mild reaction conditions (room temperature, atmospheric pressure, no H_2 needed) and does not require expensive first or second row transition-metal-based catalysts. However, despite these apparent advantages in favor of electrocatalytic reductions, there are some challenges with regard to nonproductive competitive reactions (Scheme 4.1). One is the occurrence of hydrogen evolution where adsorbed hydrogen is consumed via the so-called Tafel and Heyrovsky reactions,[13] which lowers the Faradaic efficiency of the transformation significantly.[14] Another competitive transformation is the electroreduction of the carbonyl moiety to generate the respective radical. These radicals can consume another electron to generate the targeted furfuryl alcohol or can dimerize to generate undesired diols. Hence, efficient electrocatalytic reduction transformations require a careful balancing of all the

different parameters (e.g., electrode material, reaction conditions) to favor the desired transformation over these unproductive pathways.

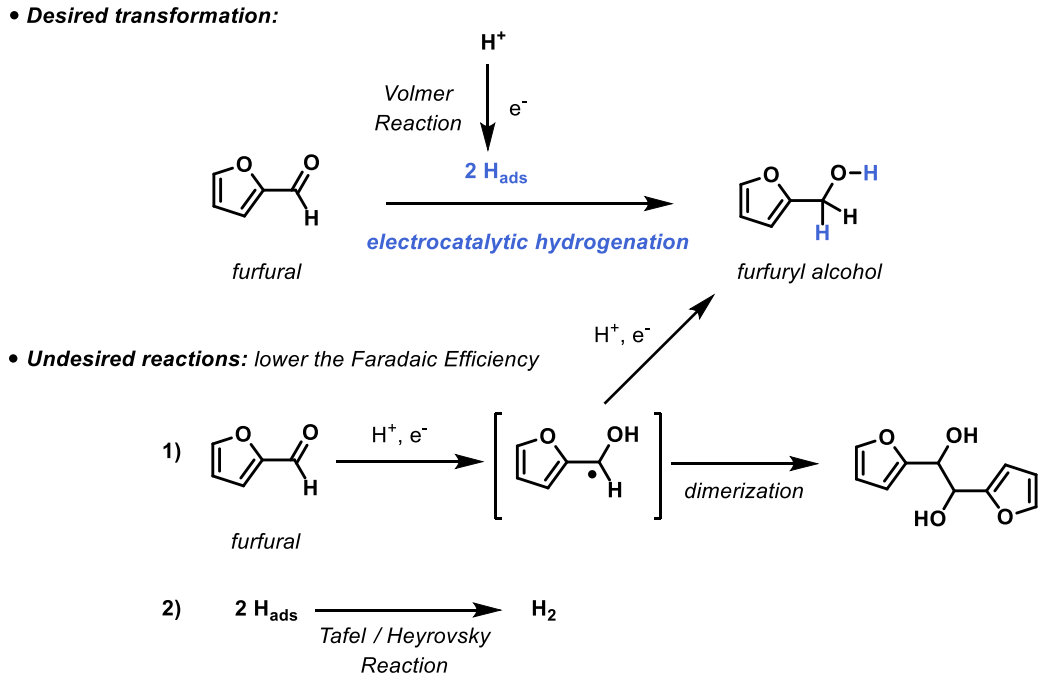

Scheme 4.1 Desired electrocatalytic hydrogenation of furfural towards furfuryl alcohol versus undesired reactions.

Herein, we report a continuous-flow direct electrolysis approach for electroreduction of furfural to address the above-mentioned issues using an electrochemical flow reactor developed in our group (Figure 4.1).[15] Key in the design of this electrochemical reactor is its flexible reactor volume, enabling two different operation modes, i.e. a serial (volume ranging from 88 µL/channel up to 704 µL) or a parallel mode (numbering-up or parallel screening of reaction conditions) (Figure 4.2).[16] In this reactor, we screened both basic and acidic reaction conditions, and our results indicate that a basic environment is optimal not only to obtain a high yield of the targeted furfuryl alcohol but also to obtain high Faradaic efficiencies.

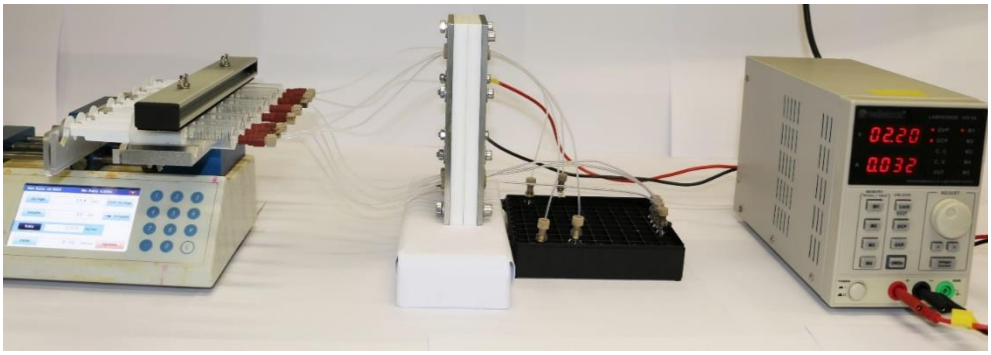

Figure 4.1 Continuous multichannel electrochemical flow reactor which allows for a rapid screening of key reaction conditions in parallel.

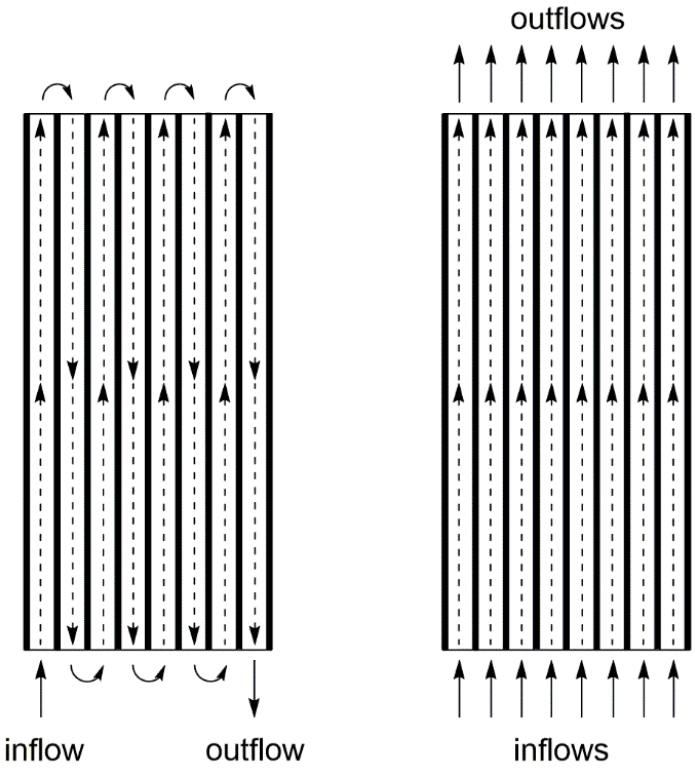

Figure 4.2 Serial mode (left) or parallel mode (right) operation of the electrochemical flow reactor.

4.2 Experimental section

General information

For the chemicals, furfural (99%), furfuryl alcohol (98%), 3-furancarboxaldehyde (97%), furan-3-methanol (99%), potassium hydroxide pellets (85%), potassium ethoxide (95%), sodium hydroxide pellets (98%), and tetrabutylammonium bromide (99%), were purchased from Sigma-Aldrich and used as received. Hydrochloric acid (37%), ethanol (99.5%), and acetonitrile (99%) were bought from VWR. Sulfuric acid (98%) was obtained from Merck. Ammoeng 110 Poly[oxy(methyl-1,2-ethanediyl)], a-[2-(diethylmethylammonio)ethyl]-w-hydroxy-,chloride (1:1), 95% was gained from Iolitec. One molar HCl and 0.5 M H_2SO_4 solution were prepared by dilution with deionized water (18.2 MΩ·cm).

Flow setup

For the flow setup, microsyringe pumps (Fusion 720, Chemyx) were used to infuse the liquid solutions. Before each set of experiments, stock solutions were prepared according to the different conditions as described herein. The liquids were taken up into disposable plastic syringes (10 mL, BD Discardit II) and mounted on the syringe pumps. Microfluidic connections between the electrochemical flow reactor and the syringes consisted of perfluoroalkoxy capillary tubing (ID 0.75 mm or 1.58 mm, PFA) and were attained from APT. Microfluidic connectors (LT-115X) and ferrules (P-259X) were procured from IDEX. Electric power (0−30 V, 0−5 A) was delivered by a LABPS3005D power supply. Electrode material (i.e., stainless steel 316L, copper Cu-DHP, and graphite) were bought at Salomon's Metalen B.V. The reactor body (reinforced iron plates and PTFE supporting containers) was manufactured by Equipment & Prototype Center at Eindhoven University of Technology. It should be noted that the electrodes did not display any corrosion under the given reaction conditions.[15,17]

Voltammogram

Prior to each experiment, a voltammogram was acquired which determines the suitable electrochemical reaction conditions.18 As shown in Figure 4.3, a plateau appeared at 2.80−3.00 V in acidic electrolyte, while it situated at 2.10−2.30 V in basic electrolyte. Therefore, 2.90 and 2.20 V were respectively chosen for subsequent optimization.

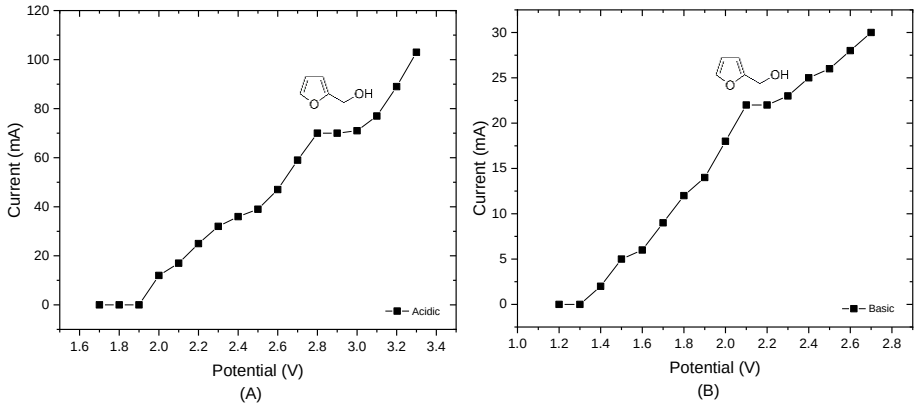

Figure 4.3 Voltammogram of furfural at a residence time of 10 min in acidic (A) or basic (B) reaction conditions.

4.3 Results and discussion

We commenced our investigations toward the electroreduction of furfural in 0.5 M sulfuric acid in combination with acetonitrile using a copper/stainless steel electrode pair (Table 4.1, entry 1). However, only a yield of 8% was obtained for the targeted furfuryl alcohol. When switching to a more protic solvent such as ethanol, an increase in yield toward 29% was witnessed (Table 4.1, entry 2). Interestingly, a further improvement was observed in the presence of hydrochloric acid (Table 4.1, entries 3 and 4). In contrast, changing the electrode material did not result into a further increase in yield (Table 4.1, entries 5−8), indicating that the combination of stainless steel/copper is optimal. Finally, we also checked the need for supporting electrolytes which are required to minimize the Ohmic drop in electrochemical processes. It is often claimed that microreactors do not require any supporting electrolytes due to small interelectrode gap.[19,20] However, in our case, small amounts of electrolyte (0.05 M), such as the ionic liquid Ammoeng 110 or n-Bu_4NBr, were beneficial to increase the overall yield.

Next, we turned our attention to basic reaction conditions using potassium ethoxide in ethanol.[21,22] Interestingly, a substantial increase in the reaction yield was observed (Table 4.2). Varying the electrode material showed that the best results were obtained with a copper/graphite couple (Table 4.2, entry 3) yielding the targeted furfuryl alcohol in 90%. Other bases, such as NaOH and KOH, did not lead to any further improvement (Table 4.2, entries 6 and 7).

Table 4.1 Optimization for furfuryl alcohol production in acidic environment[a]

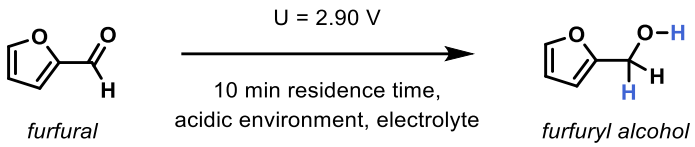

furfural *furfuryl alcohol*

Entry	Electrolyte[d]	Working Electrode[c]	Counter Electrode	Solvent	Supporting Electrolyte	Yield (%)[b]
1	H_2SO_4	Copper	Stainless Steel	CH_3CN	--	8
2	H_2SO_4	Copper	Stainless Steel	EtOH	--	29
3	HCl	Copper	Stainless Steel	CH_3CN	--	33
4	HCl	Copper	Stainless Steel	EtOH	--	41
5	HCl	Stainless Steel	Stainless Steel	EtOH	--	14
6	HCl	Graphite	Stainless Steel	EtOH	--	22
7	HCl	Copper	Graphite	EtOH	--	1
8	HCl	Copper	Copper	EtOH	--	10
9	HCl	Copper	Stainless Steel	EtOH	Ammoeng 110	55
10	HCl	Copper	Stainless Steel	EtOH	n-Bu_4NBr	55

[a] Reaction conditions: 0.1 M furfural, 0.1 M H^+, 0.05 M supporting electrolyte, 10 % H_2O, flow rate 0.075 mL/min, residence time 10 min. [b] GC-yield using GC-FID with external standard calibration. [c] The SAE international stainless steel type is 316L, the copper type is Cu-DHP. [d] The molar concentration of HCl is 0.1 mol/L, the molar concentration of H_2SO_4 is 0.05 mol/L in stock solution.

Table 4.2 Optimization for furfuryl alcohol production in basic environment[a]

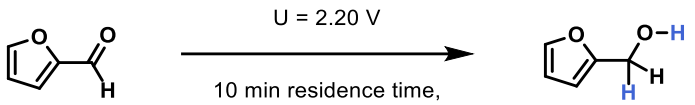

furfural *furfuryl alcohol*

Entry	Electrolyte	Working Electrode[c]	Counter Electrode	Yield (%)[b]
1	C_2H_5OK	Graphite	Graphite	25
2	C_2H_5OK	Stainless Steel	Graphite	46
3	C_2H_5OK	Copper	Graphite	90
4	C_2H_5OK	Copper	Stainless Steel	43
5	C_2H_5OK	Copper	Copper	10
6	NaOH	Copper	Graphite	41
7	KOH	Copper	Graphite	78

[a] Reaction conditions: 0.1 M furfural, 0.05 M electrolyte, ethanol solvent, flow rate 0.075 mL/min, residence time 10 min. [b] GC-yield using GC-FID with external standard calibration. [c] The SAE international stainless steel type is 316L, the copper type is Cu-DHP. The counter electrode is graphite.

Given the importance of the use of acids or bases to effect the desired transformation, we next turned our attention to scan a wide variety of different concentrations (Table 4.3). For this specific experiment, our homemade electrochemical reactor design provided a clear and unique advantage as eight reaction conditions can be screened simultaneously in parallel in the eight different channels. Hence, we rapidly found that 0.10 M HCl and 0.05 M C_2H_5OK provided optimal results for electroreduction of furfural.

Having determined the relative importance of the reaction partners, we investigated the influence of the reaction time (Figure 4.3). Interestingly, in both acidic and basic media, the optimal residence time to reach full conversion is only 10 min. We believe this very short residence time can be attributed to the large electrode surface-to-volume ratio and the short

diffusion distances observed in the electrochemical microreactor. Indeed, when we carried out the reaction in a batch electrochemical cell, the yield dropped to 18% in acidic medium and 31% in basic conditions and requires 6 h of reaction time.

Table 4.3 Optimization of electrolyte via 8-channel simultaneously parallel reactions

Channel[a]	Electrolyte	Yield (%)[c]	Channel[b]	C_2H_5OK (%)	Yield (%)[c]
1	0.05 M HCl	22	1	0.01 M	38
2	0.07 M HCl	35	2	0.02 M	50
3	0.09 M HCl	46	3	0.03 M	62
4	0.10 M HCl	55	4	0.04 M	82
5	0.11 M HCl	53	5	0.05 M	90
6	0.13 M HCl	49	6	0.06 M	88
7	0.15 M HCl	46	7	0.07 M	86
8	0.17 M HCl	45	8	0.08 M	83

[a] Reaction conditions: 0.1 M furfural, 2.90 V, 10% H_2O, ethanol solvent, flow rate 0.075 mL/min, residence time 10 min. [b] Reaction conditions: 0.1 M furfural, 2.20 V, ethanol solvent, flow rate 0.075 mL/min, residence time 10 min. [c] GC-yield using GC-FID with external standard calibration.

Next, we tested the influence of constant current or constant potential electrolysis conditions (Figure 4.4). Constant potential electrolysis offers a more stable and tunable selectivity,[17] while constant current electrolysis provides a more controlled and constant reaction conversion.[23] However, for the electroreduction of furfural, almost similar behavior was observed under these two operational regimes. This gives us a high level of flexibility: if higher selectivity is required, one can use the constant potential conditions, while galvanostatic conditions are preferred to establish an adequate chemical conversion in shorter time scales. However, it must be noted that even though we did use potentiostatic reaction conditions, the flow processing enables us the keep the conversion time very short as described above (t_R = 10 min, see Figure 4.5).

Having the optimal reaction conditions for the electroreduction of 2-furfural in hand (Table 4.4, entries 1 and 2), we investigated if the conditions were also applicable to 3-furfural

(Table 4.4, entries 5 and 6). Interestingly, the same trend was observed for 3-furfural with the most optimal conversion and yield observed in basic media (Table 4.4, entry 6). In addition, for all the different conditions, we calculated the Faradaic efficiency: high Faradaic efficiencies were obtained for the basic reaction conditions (90−92%), while in acidic media, very poor Faradaic efficiencies were observed (18−19%). This can be attributed to the generation of higher amounts of hydrogen, as the hydrogen evolution reaction competes more efficiently with the electrocatalytic hydrogenation reaction in acidic reaction conditions. Interestingly, the corresponding batch conditions were not only considerably slower but also provided lower yields and Faradaic efficiencies (Table 4.4, entries 3 and 4). We surmise that the slower reaction times are due to mass transfer limitations and lower electrode surface-to-volume ratios and give more time for the undesired hydrogen formation reaction to occur.

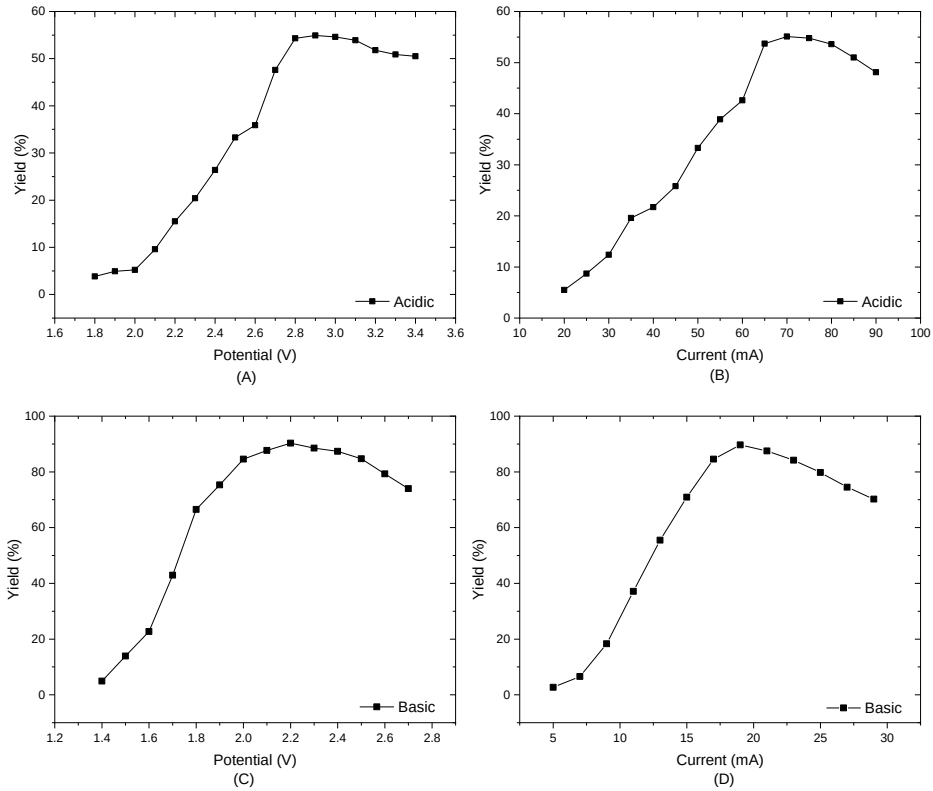

Figure 4.4 Constant-potential (A)(C) vs constant-current (B)(D) electrolysis.

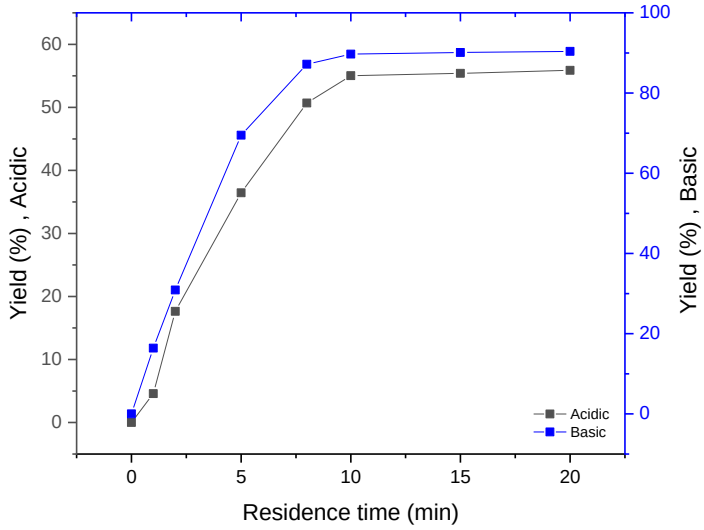

Figure 4.5 Influence of the residence time on the electroreduction of furfural to furfuryl alcohol in acidic and basic media.

Table 4.4 Scope for furfural electroreduction in flow & comparison with batch reaction conditions.

Entry	Reactor Type	Substrate	Electrolyte	Yield (%)[e]	Faradaic Efficiency (%)
1[a]	Flow	furfural (2-furaldehyde)	HCl	55	19
2[b]	Flow	furfural (2-furaldehyde)	C_2H_5OK	90	90
3[c]	Batch	furfural (2-furaldehyde)	HCl	18	12
4[d]	Batch	furfural (2-furaldehyde)	C_2H_5OK	31	60
3[a]	Flow	3-furfural (3-furaldehyde)	HCl	40	18
4[b]	Flow	3-furfural (3-furaldehyde)	C_2H_5OK	78	92

[a] Reaction conditions: 0.1 M furfural, 2.90 V, 0.1 M electrolyte, 10% H_2O, ethanol solvent, flow rate 0.075 mL/min, residence time 10 min. [b] Reaction conditions: 0.1 M furfural, 2.20 V, 0.05 M electrolyte, ethanol solvent, flow rate 0.075 mL/min, residence time 10 min. [c] Reaction conditions: 0.1 M furfural, 2.90 V, 0.1 M electrolyte, 10% H_2O, ethanol solvent, residence time 300 min. [d] Reaction conditions: 0.1 M furfural, 2.20 V, 0.05 M electrolyte, ethanol solvent, residence time 300 min [e] GC-yield using GC-FID with external standard calibration.

Finally, we investigated the steady state production of 2-furfuryl alcohol under these acidic and basic reaction conditions. We took reaction samples every 5 min and analyzed the obtained yield via GC-FID. The overall observed trend for both conditions showed a decline in yield over time. This decline can be attributed to erosion of the electrode efficiency. It was noteworthy, however, that the efficacy of the electrodes could be restored by incorporating an adequate cleaning and surface treatment step (Figure 4.6). This indicates that the reduced yield is caused by a deposition on the electrode surface which can be washed away effectively.[24] To keep the reaction yield constant, we could place two reactors in parallel: one of them is in operation mode while the other one is in cleaning mode. When the yield drops, the modes can be switched and a "continuous" production of electrocatalytic reduction of furfural can be simulated.

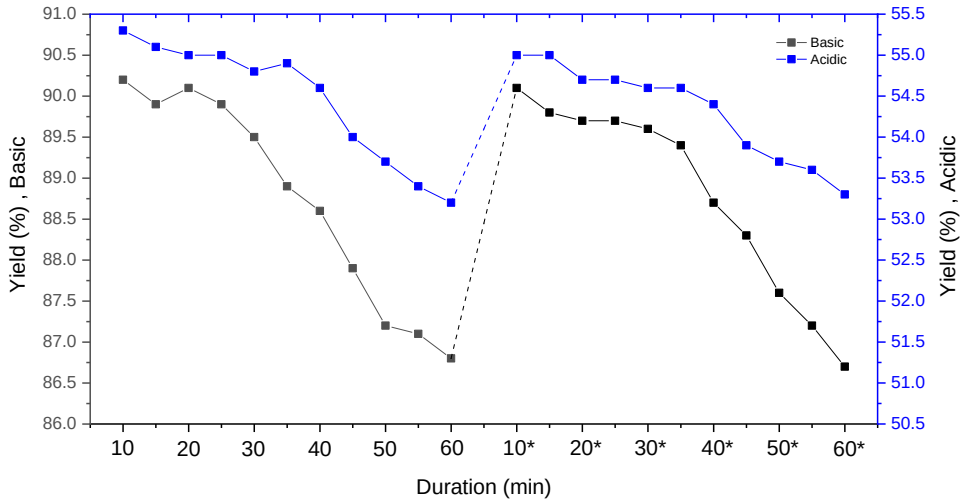

Figure 4.6 Two runs of stability test (60 min) for reactions (Table 4.4, entries 1 and 2) with 10 min residence time.

4.4 Conclusion

In conclusion, we developed a continuous-flow protocol for the electrocatalytic reduction of furfural. Both acidic and basic reaction conditions were evaluated. We found that the basic reaction conditions delivered the highest yield for the targeted furfuryl alcohol and provided

a high Faradaic efficiency. The reaction could be completed in only 10 min and required only a minimum amount of supporting electrolyte, highlighting the benefits of the microreactor environment. While an efficient process was established in flow, a reduced efficiency was observed due to pollution of the electrodes. However, we found that a cleaning step could alleviate this issue effectively.

References

[1] Mariscal R, Maireles-Torres P, Ojeda M, Sádaba I, López Granados M (2016). Energy Environ Sci 9:1144–1189

[2] LaForge FB (1923). Ind Eng Chem 15:499–502

[3] Riera FA, Alvarez R, Coca J (1991). J Chem Technol Biotechnol 50:149–155

[4] Sánchez C, Serrano L, Andres MA, Labidi J (2013). Ind Crops Prod 42:513–519

[5] Gandini A, Belgacem MN (1997). Prog Polym Sci 22:1203–1379

[6] Eseyin EA, Steele HP (2015). Int J Adv Chem 3:2

[7] Möhle S, Zirbes M, Rodrigo E, Gieshoff T, Wiebe A, Waldvogel SR (2018). Angew Chemie Int Ed 57:6018–6041

[8] Chamoulaud G, Floner D, Moinet C, Lamy C, Belgsir EM (2001). Electrochim Acta 46:2757–2760

[9] Chadderdon XH, Chadderdon DJ, Matthiesen JE, Qiu Y, Carraher JM, Tessonnier J-P, Li W (2017). J Am Chem Soc 139:14120–14128

[10] Kwon Y, Schouten KJP, van der Waal JC, de Jong E, Koper MTM (2016). ACS Catal 6:6704–6717

[11] Parpot P, Bettencourt AP, Chamoulaud G, Kokoh KB, Belgsir EM (2004). Electrochim Acta 49:397–403

[12] Guena T, Pletcher D (1998). Acta Chem Scand 52:23–31

[13] de Chialvo MRG, Chialvo AC (1994). J Electroanal Chem 372:209–223

[14] Yuan H, He Z (2017). Chem Rec 17:641–652

[15] Laudadio G, de Smet W, Struik L, Cao Y, Noël T (2018). J Flow Chem 8:157–165

[16] Pletcher D, Green RA, Brown RCD (2018). Chem Rev 118:4573–4591

[17] Laudadio G, Straathof NJW, Lanting MD, Knoops B, Hessel V, Noël T (2017). Green Chem 19:1–6

[18] Nicholson RS, Shain I (1964). Anal Chem 36:706–723

[19] Folgueiras-Amador AA, Philipps K, Guilbaud S, Poelakker J, Wirth T (2017). Angew Chemie - Int Ed 56:15446–15450

[20] Folgueiras-Amador AA, Wirth T (2017). J Flow Chem 7:94–95

[21] Bradley DC (1959). Metal-Organic Compounds, 2–10

[22] Msayiband KJ, Almost I, Szwarcl M, Ion A (1992). Chem Soc Rev 21:237−243

[23] Wiebe A, Riehl B, Lips S, Franke R, Waldvogel SR (2017). Sci Adv 3: eaao3920

[24] Somerville L, Bareño J, Jennings P, McGordon A, Lyness C, Bloom I (2016). Electrochim Acta 206:70–76

CHAPTER 5

Paired electrochemical conversion of furfural in flow

This chapter is based on:

Cao, Y.; Knijff, J.; Delparish, A.; Neira d'Angelo, M. F. and Noel, T. A Divergent Paired Electrochemical Process for the Conversion of Furfural Using a Divided-Cell Flow Microreactor. *ChemSusChem* **2021**, 14 (2), 590–594.

Abstract

Furfural is a prominent, non-petroleum-based chemical feedstock material, derived from abundantly available hemicellulose. Hence, its derivatisation into other useful biobased chemicals is a subject of high interest in contemporary academic and industrial research activities. While most strategies to convert furfural require energy-intensive reaction routes, the use of electrochemical activation allows to provide a sustainable and green alternative. Herein, we report a disparate approach for the conversion of furfural based on a divergent paired electrochemical conversion, enabling the simultaneous production of 2(5H)-furanone via an anodic oxidation, and the generation of furfuryl alcohol and/or hydrofuroin via a cathodic reduction. Using water as solvent and NaBr as supporting electrolyte and electron-mediator, a green and sustainable process was developed which maximizes productive use of electricity and minimizes byproduct formation

5.1 Introduction

Furfural is one of the most prominent biobased molecules, registered as a top 30 biomass-derived platform molecule by the US Department of Energy.[1] It is obtained by hydrolysis and dehydration of xylan, which is abundantly available from hemicellulose. Furfural is currently produced on a 300 kTon per annum scale and about 70% of its production is carried out in China.[2]

The establishment of furfural as a commodity chemical spurs academic and industrial interest to develop new synthetic routes for its further derivatisation into useful chemicals, materials and biofuels.[3–5] Amongst the different strategies used to convert furfural (e.g. pyrolysis, gasification, thermo-catalytic processes), the use of electrochemical activation enables a green and sustainable alternative to these often high-energy-demanding processes.[6–10] Notably, electrochemistry allows to convert green electricity, derived from wind and solar energy, directly into useful chemicals and kinetic barriers are overcome by applying a suitable potential over the electrodes. Hence, no additional reagents are required to enable the reduction[11–14] and oxidation processes,[15] which can aid to further reduce fossil fuel consumption (e.g. hydrogen is often derived from natural gas via the water-gas shift reaction).[16]

While several useful electrochemical strategies for the conversion of furfural have been developed, the focus so far was almost exclusively on the optimization of a single electrode reaction. However, when both electrode reactions are harmonized to produce value-added products, a green and sustainable synthesis can be obtained which maximizes productive use of electricity, minimizes waste generation and reduces energy consumption.[17–20] Such a coupled process, also called “paired electrolysis”, would be of great added value for the conversion of furfural, where the economical margins are often low.

Herein, we describe such a divergent paired electrochemical conversion of furfural where the cathodic and anodic reactions are separated by a membrane and are productively used to generate valuable derivatives (Figure 5.1 A). To further increase the utility and scalability of the process,[21] the reactions are carried out in a continuous-flow electrochemical reactor with a narrow inter-electrode gap (Figure 5.1 B).[22–26] The selectivity can be increased in such

reactors due to the large electrode surface-to-volume ratio and due to a meticulous control over the residence time and the cell potential. Using such intensified reaction conditions, the reaction time is typically reduced significantly compared to batch cells and, thus, the products are only briefly exposed to the electrochemical conditions, efficiently avoiding undesired follow-up reactions.[27–29] In this work, we show that a divergent paired electrochemical flow strategy enables the simultaneous production of 2(5H)-furanone via an anodic oxidation, and the generation of furfuryl alcohol and/or hydrofuroin via a cathodic reduction (Figure 5.1 A). It should be noted that these three biobased compounds derived from furfural have great synthetic and practical value. 2(5H)-furanone can readily be reduced to generate γ-butyrolactone,[30,31] a valuable biobased solvent, synthetic intermediate and monomer for the synthesis of poly(γ-butyrolactone).[32] Furfuryl alcohol is mainly used as a raw material to produce furan-based foundry resins,[13] while hydrofuroin can be utilized as a jet-fuel precursor.[33]

5.2 Results and discussion

We commenced our investigations by repurposing our original electrochemical flow reactor design (Figure 5.1B).[34] An ion exchange membrane was used to separate the anodic and the cathodic electrolysis half-cells.[35] Both cation- (Nafion XL) and anion-exchange (Fumasep FAS-50) membranes[36] were purchased and could be readily sandwiched between two Teflon reaction channel spacers as shown in Figure 5.1B. The reaction solution was introduced into the two half-cells of the electrochemical flow reactor using syringe pumps (Fusion 200, Chemyx). The catholyte and anolyte were separately collected and analysed by GC-FID.

Prior to the optimization studies, a voltammogram was recorded to establish the operational windows for the electrolysis of furfural (Figure 5.2). Two clear plateaus can be distinguished at 2.3–2.5 V and 2.8–3.0 V for both the cation- and the anion-exchange membrane. The current is higher at any given potential for the cation exchange membrane, suggesting a lower resistance for ion transport compared to the anion-exchange membrane.

Based on these results (Figure 5.2), we decided to use our flow cell in a constant-potential or potentiostatic operation mode and set the cell potential at either 2.4 V or 2.9 V (Table 5.2). In our experience, a potentiostatic mode in combination with a continuous-flow operation

allows to obtain high selectivities for a targeted compound without the need to extend the reaction times.[29,37,38]

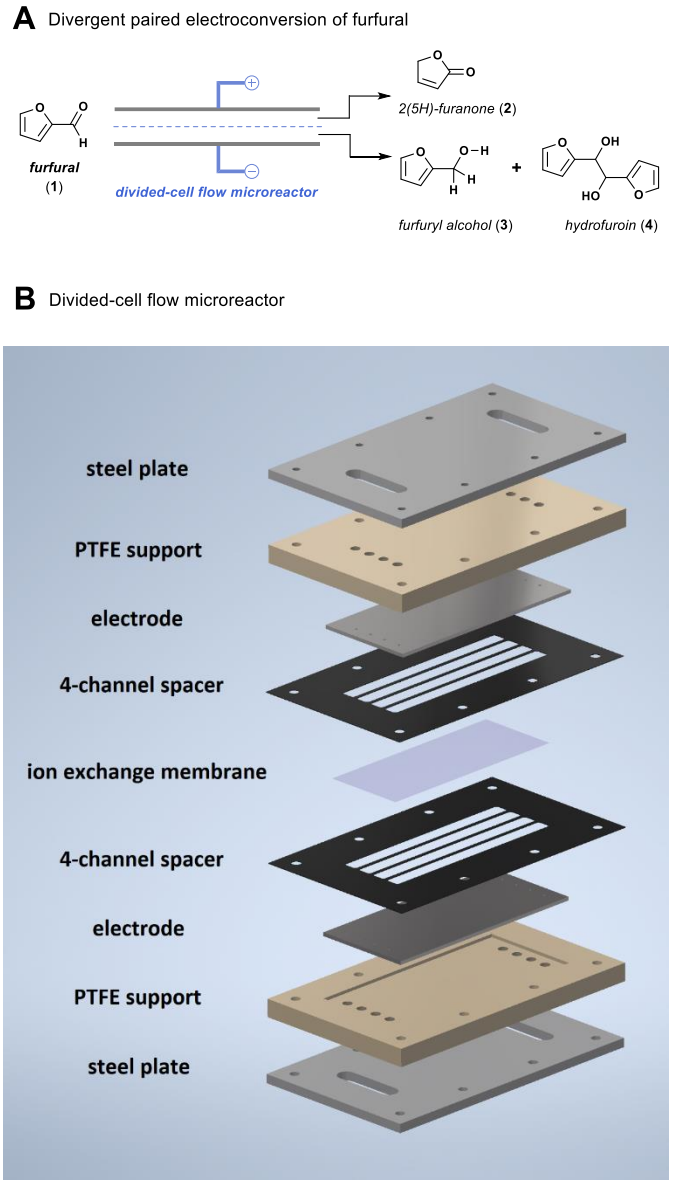

Figure 5.1 (A) Processes based on a divergent paired electrolysis of furfural allows to obtain useful derivatives of both cathodic and anodic processes simultaneously. (B) Schematic representation of the divided-cell flow microreactor design using an ion-exchange membrane

to separate the anodic and the cathodic electrolysis half-cells.

Extended reaction times, observed with potentiostatic electrochemical transformations, is an often encountered problem in batch electrolysis as the current decreases with increasing conversions.[39] However, in flow, high substrate concentrations are encountered at the entrance of the reactor and low concentrations at the exit, leading to an average current density over the entire reactor length. This phenomenon in combination with the high electrode surface-to-volume ratio results in significantly reduced reaction times in flow.[22] An aqueous mixture of furfural and NaBr, as supporting electrolyte and potentially as anodic electron mediator[40] facilitating the oxidation process,[41,42] was infused into the reactor. The two half-cells are separated by a Fumasep FAS-50 anion-exchange membrane and graphite was initially selected as anode and lead as the cathode, which has a high hydrogen overpotential (Table 5.1, Entry 1).[43] Suppression of the hydrogen evolution reaction is important to ensure high Faradaic efficiencies[44,45] and to avoid gas formation which leads to a higher Ohmic drop.[46] As can be seen from Table 5.1, within 5 min residence/reaction time, good yields are obtained for 2(5H)-furanone at the anodic half-cell and furfuryl alcohol and hydrofuroin at the cathodic half-cell. At a cell potential of 2.4 V, a higher selectivity is observed for furfuryl alcohol at the cathode (Table 5.1, Entry 1). A higher yield for both 2(5H)-furanone and hydrofuroin are observed at a cell potential of 2.9 V, respectively 77% and 71% (Table 5.1, Entry 1). This result demonstrates that small changes in cell potential allow to fine-tune the selectivity of the electrochemical redox process. Other electrode materials, such as Ni, 316 L stainless steel, Monel 400, copper, showed a reduced efficacy to generate the targeted compounds (Table 5.1, Entries 2-9).

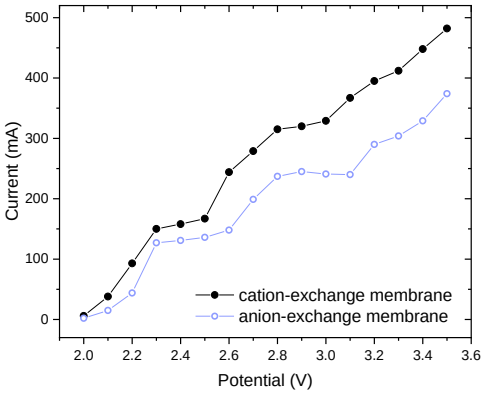

Figure 5.2 Voltammogram of furfural in the divided-cell flow microreactor design using an anion- or a cation-exchange membrane.

Table 5.1 Screening of electrode materials for the paired electrolysis of furfural.[a]

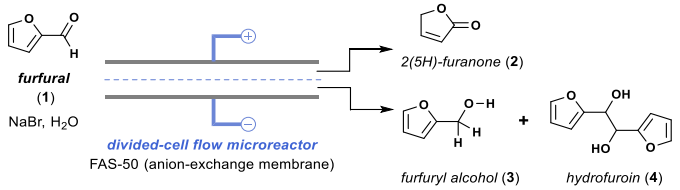

Entry	Anode	Cathode	Yield 2 [%][b]		Yield 3 [%][b]		Yield 4 [%][b]	
			2.4 V	2.9 V	2.4 V	2.9 V	2.4 V	2.9 V
1	**G**	**Pb**	**46**	**77**	**58**	**20**	**29**	**71**
2	Ni	Pb	Trace	11	54	17	18	46
3	316L	Pb	Trace	10	45	10	9	32
4	Monel 400	Pb	14	23	60	26	12	55
5	G	Cu	40	73	56	24	25	64
6	G	Monel 400	36	70	47	9	23	62
7	G	Ni	32	65	51	17	17	49
8	G	G	32	69	28	Trace	20	20
9	G	316L	27	49	34	Trace	Trace	33

[a] Reaction conditions: 0.1 M furfural, 0.1 M NaBr, H_2O, 5 min residence time, Fumasep FAS-50 as an anion exchange membrane. [b] GC-yield using GC-FID with internal standard (toluene).

An investigation of the yield and selectivity in function of the residence/reaction time was carried out for both the cation- and the anion-exchange membrane configuration (Figure 5.3). For the anodic half-cell (Figure 5.3 A), the highest yield for 2(5H)-furanone (77% GC yield) is observed at 5 min for the anion-exchange membrane after which it reaches a plateau. At 5 min residence/reaction time, the yield at the cation-exchange membrane is only 62% for the targeted compound (Figure 5.3 A). Interestingly, at the cathodic half-cell, better results are obtained with the cation-exchange membrane for the production of furfuryl alcohol and hydrofuroin. However, the difference in performance between the two membranes is less pronounced than for the anodic half-cell; e.g. at 5 min 75% hydrofuroin and 14 % furfuryl

alcohol is obtained for the cation-exchange membrane versus 67% hydrofuroin and 26% furfuryl alcohol for the anion-exchange membrane. Hence, we selected the anion-exchange membrane for our further studies.

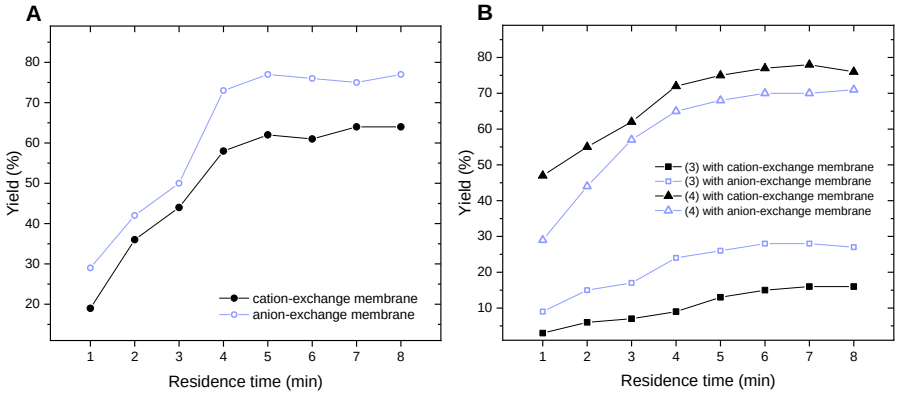

Figure 5.3 Residence Time Screening for the (A) anodic half-cell yielding 2(5H)-furanone (2), and (B) cathodic half-cell yielding furfuryl alcohol (3) and hydrofuroin (4). Reaction conditions: 0.1 M furfural, 0.1 M NaBr, H_2O, graphite anode | lead cathode, cell potential 2.9 V. Yields obtained with GC-FID and internal standard calibration (toluene).

Next, we investigated the effect of various halide sources on the reaction outcome (Table 5.2). The best results were obtained with bromide salts (Table 5.2, Entry 1 versus Entry 2). It is known that bromide ions enable mild and indirect anodic oxidations via either hypobromite (BrO-) or bromonium (Br+) intermediates.[47–50] Other alkali bromide sources were also effective but the best results were obtained with cheap and abundantly available NaBr (Table 5.2, Entries 1, 3-7). Addition of small quantities (10 vol %) of organic solvents did not lead to any significant improvement and was even less effective in the cases of methanol and THF (Table 5.2, Entries 8-10). Interestingly, in the absence of a membrane, a much-reduced reaction efficiency was noticed (Table 5.2, Entry 11); this observation demonstrates that the presence of a suitable membrane to separate the two half reactions is crucial to obtain high yields and selectivities.

In order to scale up this paired electrolysis of furfural, we wondered if it was possible to increase the concentration of the starting material without compromising the yield and the

selectivity (Figure 5.4). A higher concentration would result in a higher throughput whilst keeping the residence time constant. Indeed, the concentration could be increased up to 0.6 M furfural without reducing the efficacy of the electrochemical process. Higher concentrations were not possible due to the limited solubility of furfural in water.

Table 5.2 Influence of halide sources, solvent and control experiment for the paired electrolysis of furfural.[a]

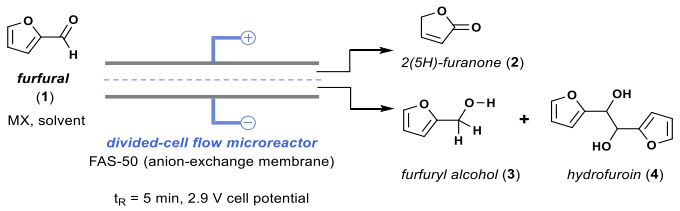

Entry	MX	Solvent	Yield 2 [%][b]	Yield 3 [%][b]	Yield 4 [%][b]
1	**NaBr**	**H_2O**	**77**	**20**	**71**
2	NaCl	H_2O	Trace	Trace	Trace
3	LiBr	H_2O	64	10	32
4	KBr	H_2O	59	26	55
5	CsBr	H_2O	61	25	67
6	$MnBr_2$	H_2O	15	7	27
7	TBAB	H_2O	38	24	29
8	NaBr	H_2O + CH_3CN[c]	77	27	66
9	NaBr	H_2O + CH_3OH[c]	58	33	41
10	NaBr	H_2O + THF[c]	52	12	22
11[d]	NaBr	H_2O	Trace	16	11

[a] Reaction conditions: 0.1 M furfural, 0.1 M MX, graphite anode|lead cathode, residence time 5 min, cell potential 2.9 V, full conversion with anion exchange membrane [b] Yields obtained with GC-FID and internal standard calibration (toluene). [c] The solvent consists of 90 vol% H_2O and 10 vol% organic solvent. [d] The reaction was done with the same conditions as Entry 1 but in an undivided electrochemical flow cell.

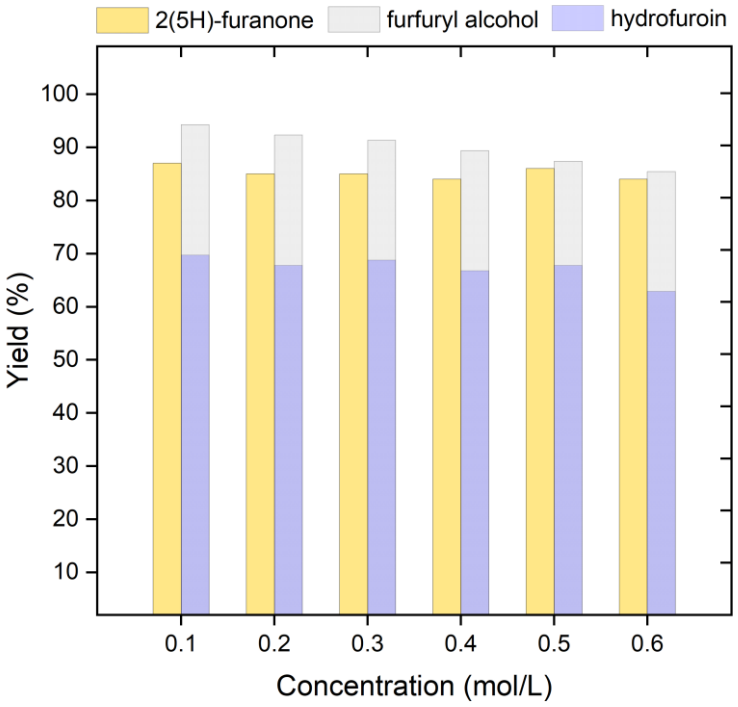

Figure 5.4 Concentration effect on the divergent paired electrolysis of furfural. Reaction conditions: x M furfural, 0.1 M NaBr, H_2O, 5 min residence time, Fumasep FAS-50 as an anion exchange membrane. [b] GC-yield using GC-FID with internal standard (toluene).

Based on the experimental observations, a plausible mechanism is suggested in Figure 5.5. In the anodic half-cell, the C5 chemical furfural is converted into the C4 building block 2(5H)-furanone in excellent yield. Based on recent work from Song, Han and coworkers,[51] we suggest that a hydroxyl-radical-induced C–C bond cleavage generates the corresponding 2-hydroxyfuran and formic acid. Subsequent isomerization of 2-hydroxyfuran generates the observed 2(5H)-furanone. In the cathodic half-cell, furfural is reduced to generate the corresponding radical.[44] These radicals can dimerize to yield the C10 compound, hydrofuroin. Competitively, the radical can consume another electron to generate furfuryl alcohol.

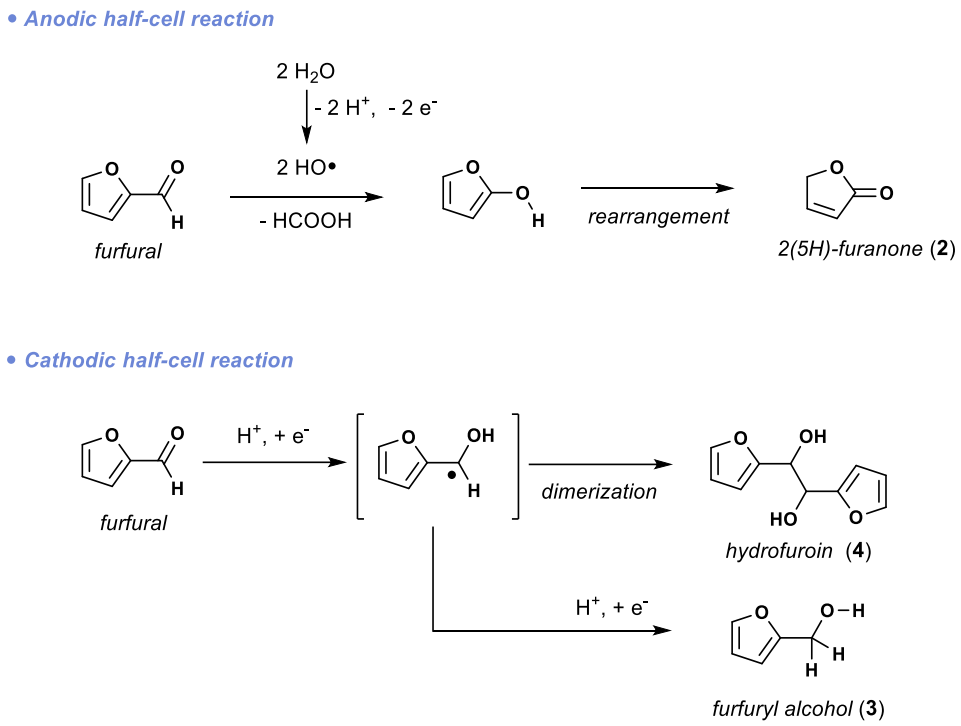

Figure 5.5 Proposed mechanism for the divergent paired electrolysis of furfural.

5.3 Conclusion

We have developed a divergent, paired continuous-flow electrolysis of furfural yielding useful bio-based chemicals; this includes 2(5H)-furanone via an anodic oxidation and furfuryl alcohol and hydrofuroin at the cathodic half-cells. We have shown that it is key to separate the two half-cell reactions from each other with a membrane to obtain high yields and selectivities. Interestingly, the reactions can be carried out in water as a green solvent and only require NaBr as supporting electrolyte and electron-mediator. We believe that this paired electrochemical process to convert furfural into useful bio-based derivatives will be of great added value from the vantage point of an increased productive use of electricity, and a reduction of waste generation and energy consumption.

References

[1] Noël T, Cao Y, Laudadio G (2019). Acc Chem Res 52:2858–2869

[2] White J, Werpy T, Petersen G, Holladay J (2004) Top Value Added Chemicals from Biomass, Vol.1: Results of screening for potential candidates from sugars and synthesis gas. U.S. Department of Energy

[3] Kingston C, Palkowitz MD, Takahira Y, Vantourout JC, Peters BK, Kawamata Y, Baran PS (2020). Acc Chem Res 53:72–83

[4] Cao Y, Noël T (2019). Org Process Res Dev 23:403–408

[5] May AS, Biddinger EJ (2020). ACS Catal 10:3212–3221

[6] Lam CH, Deng W, Lang L, Jin X, Hu X, Wang Y (2020). Energy & Fuels 34:7915–7928

[7] Yan K, Wu G, Lafleur T, Jarvis C (2014). Renew Sustain Energy Rev 38:663–676

[8] Wang Y, Zhao D, Rodríguez-Padrón D, Len C (2019). Catalysts 9:796

[9] Holade Y, Tuleushova N, Tingry S, Servat K, Napporn TW, Guesmi H, Cornu D, Kokoh KB (2020). Catal Sci Technol 10:3071–3112

[10] Garedew M, Lin F, Song B, DeWinter TM, Jackson JE, Saffron CM, Lam CH, Anastas PT (2020). ChemSusChem 13:4214–4237

[11] Paddon CA, Atobe M, Fuchigami T, He P, Watts P, Haswell SJ, Pritchard GJ, Bull SD, Marken F (2006). J Appl Electrochem 36:617

[12] Ibanez JG, Frontana-Uribe BA, Vasquez-Medrano R (2016). J Mex Chem Soc 60:247–260

[13] Martínez NP, Isaacs M, Nanda KK (2020). New J Chem 44:5617–5637

[14] Laudadio G, de Smet W, Struik L, Cao Y, Noël T (2018). J Flow Chem 8:157–165

[15] Mariscal R, Maireles-Torres P, Ojeda M, Sádaba I, López Granados M (2016). Energy Environ Sci 9:1144–1189

[16] Chadderdon XH, Chadderdon DJ, Pfennig T, Shanks BH, Li W (2019). Green Chem 21:6210–6219

[17] Gérardy R, Debecker DP, Estager J, Luis P, Monbaliu J-CM (2020). Chem Rev 120:7219–7347

[18] Pletcher D, Green RA, Brown RCD (2018). Chem Rev 118:4573–4591

[19] Atobe M, Tateno H, Matsumura Y (2018). Chem Rev 118:4541–4572

[20] Nicholls TP, Schotten C, Willans CE (2020). Curr Opin Green Sustain Chem 26:100355

[21] Elsherbini M, Wirth T (2019). Acc Chem Res 52:3287–3296

[22] Laudadio G, Straathof NJW, Lanting MD, Knoops B, Hessel V, Noël T (2017). Green Chem 19:4061–4066

[23] Li X, Jia P, Wang T (2016). ACS Catal 6:7621–7640

[24] Maljuric S, Jud W, Kappe CO, Cantillo D (2020). J Flow Chem 10:181–190

[25] Schwarz W, Schossig J, Rossbacher R, Pinkos R, Höke H (2019). Ullmann's Encycl. Ind. Chem. 1–7

[26] Li X, Wan W, Chen JG, Wang T (2018). ACS Sustain Chem Eng 6:16039–16046

[27] Hong M, Chen EY-X (2016). Nat Chem 8:42–49

[28] Shang X, Yang Y, Sun Y (2020). Green Chem 22:5395–5401

[29] Xu T (2005). J Memb Sci 263:1–29

[30] Varcoe JR, Atanassov P, Dekel DR, Herring AM, Hickner MA, Kohl PA, Kucernak AR, Mustain WE, Nijmeijer K, Scott K, Xu T, Zhuang L (2014). Energy Environ Sci 7:3135–3191

[31] Oseka M, Laudadio G, van Leest NP, Dyga M, de Andrade Bartolomeu A, Goossen L, de Bruin B, Thiago de Oliveira K, Noel T (2020). Chem 7:255-266

[32] Gütz C, Klöckner B, Waldvogel SR (2016). Org Process Res Dev 20:26–32

[33] Chen S, Wojcieszak R, Dumeignil F, Marceau E, Royer S (2018). Chem Rev 118:11023–11117

[34] Inokuchi T, Matsumoto S, Torii S (1991). J Org Chem 56:2416–2421

[35] Cao Y, Adriaenssens B, de A. Bartolomeu A, Laudadio G, de Oliveira KT, Noël T (2020). J Flow Chem 10:191–197

[36] Francke R, Little RD (2014). Chem Soc Rev 43:2492–2521

[37] Laudadio G, Barmpoutsis E, Schotten C, Struik L, Govaerts S, Browne DL, Noël T (2019). J Am Chem Soc 141:5664–5668

[38] Leech MC, Garcia AD, Petti A, Dobbs AP, Lam K (2020). React Chem Eng 5:977–990

[39] Heard DM, Lennox AJJ (2020). Angew Chemie Int Ed 59:18866–18884

[40] Velázquez-Olvera S, Salgado-Zamora H, Campos-Aldrete M-E, Reyes-Arellano A, Pérez-González C, Velázquez-Ponce M (2014). Green Chem Lett Rev 7:296–300

[41] Cao Y, Soares C, Padoin N, Noël T (2021). Chem Eng J 406:126811

[42] Jacquet F, Gaset A, Simonet J, Lacoste G (1985). Electrochim Acta 30:477–484

[43] Torii S, Inokuchi T, Mishima S, Kobayashi T (1980). J Org Chem 45:2731–2735

[44] Yoshida J, Nakai R, Kawabata N (1980). J Org Chem 45:5269–5273

[45] Xu C, Paone E, Rodríguez-Padrón D, Luque R, Mauriello F (2020). Chem Soc Rev 49:4273–4306

[46] Li H, Li W, Guo Z, Gu D, Cai S, Fujishima A (1995). Collect Czechoslov Chem Commun 60:928–934

[47] Wu H, Song J, Liu H, Xie Z, Xie C, Hu Y, Huang X, Hua M, Han B (2019). Chem Sci 10:4692–4698

[48] Pollok D, Waldvogel SR (2020). Chem Sci 11: 12386-12400

[49] Du L, Shao Y, Sun J, Yin G, Du C, Wang Y (2018). Catal Sci Technol 8:3216–3232

[50] Prabhu P, Wan Y, Lee J-M (2020). Matter 3:1162–1177

[51] Schotten C, Nicholls TP, Bourne RA, Kapur N, Nguyen BN, Willans CE (2020). Green Chem 22:3358–3375

CHAPTER 6

CFD study on gas bubble effects in Taylor flow electrochemistry

This chapter is based on:

Cao, Y.; Soares, C.; Padoin, N. and Noel, T. Gas Bubbles Have Controversial Effects on Taylor Flow Electrochemistry. *Chemical Engineering Journal* **2021**, 406, 126811

Abstract

Electrochemistry is currently resurging in popularity amongst synthetic chemists due to the unique opportunities it provides to activate organic molecules. Simultaneously, continuous-flow technology has been used to enable scalability and to increase the efficiency of the developed electrochemical processes. Many of these processes involve a gaseous reagent or byproduct generated during the electrochemical process. The presence of a gas phase in flow reactors may lead to the generation of a so-called Taylor flow regime, where gas bubbles and liquid segments alternate. While Taylor flow has almost exclusive positive effects in flow chemistry due to increased mass and heat transfer, we show herein that the ramifications of gas bubbles on flow electrochemistry are essentially negative. Computational fluid dynamics (CFD) was used to gain a detailed understanding of the effects induced by the gas phase on the electrochemical process, taking the reduction of furfural to furfuryl alcohol carried out in an in-house developed electrochemical reactor as benchmark. We show that the gas bubble presents a local situation with infinite electrical resistance leading to a temporary passivation of the electroactive surface, while its presence also intensifies the mixing in the liquid slug reducing mass transfer limitations. Essentially, the larger the bubble, the higher the energy losses become and the less efficient the reactor is used. This results in a higher overall energy consumption for the electrochemical process. Moreover, we investigated the residence time distribution in the liquid slug, and the effect of different operational conditions (bubble size, gas holdup, interelectrode distance, electrolyte velocity and species concentration) on the overpotential and current density, providing guidelines for reactor design and operation. Based on the results described herein, we also discuss potential solutions to increase the efficiency of the electrochemical flow reactor.

6.1 Introduction

Due to the increased availability of green electricity, the use of electrons as energy carrier has permeated a wide variety of different applications, including the electrification of the transport and the energy sector.[1,2] Similarly, the chemical industry is interested in using electrons for chemical activation, not only from a sustainability perspective but also due to its ability to establish new reaction pathways and to provide higher selectivities compared to conventional, nonelectrochemical synthetic pathways.[3,4]

Most electroorganic transformations are carried out under homogeneous reaction conditions (single-phase), where all reagents, products and electrolytes are in solution. However, multiphase reactions, such as hydrogenations and oxidations as common gas-liquid transformations, are mainstay in the chemical industry. Also, in electrochemistry, reactions with gaseous reagents and/or byproducts are often observed,[5] e.g. when hydrogen evolution occurs at the cathode.[6]

In general, gas–liquid reactions are challenging transformations due to gravity-driven segregation of the gas and the liquid phase. Microreactors have been embraced by the community to carry out such reactions as they provide high surface-to-volume ratios, short diffusion distances, high and reproducible interfacial areas.[7,8] The most popular flow regime is the so-called Taylor flow[9] which is characterized by alternating gas and liquid segments (Figure 6.1).[10,11] In those segments, toroidal fluid circulation patterns are observed which allow for increased radial heat and mass transfer and minimized axial dispersion effects.[12] Consequently, Taylor flow has been widely employed for a variety of applications, including the improved irradiation for photochemical applications (Figure 6.1 A)[13], the prevention of microchannel clogging,[14] the enhancement of catalysis in wallcoated catalytic microreactors[15] (Figure 6.1 B) and the preparation of monodisperse nanoparticles.[16] In most of these transformations, the addition of a gas phase results in net-positive effects.[17] The thin liquid film (also called lubricating film) that surrounds the gas bubble plays an important role in the observed transport phenomena, allowing for a fast local gas saturation of the liquid, which is beneficial when the gas is a reagent.[18] In photochemistry, this layer is suspected to receive the highest photon flux and displays thus the highest reaction kinetics.[19,20] However,

we wondered what the effect of an additional gas phase would be on electrochemical transformations carried out in a microreactor operating under Taylor flow?[21] Bubbles are known to influence the mass and energy transport phenomena[22] and several studies in the past have been focused on the understanding of their impact on electrochemical systems.[23,27] These studies centred mainly around the effects of attached bubbles at the electrode surface, or gas flowing in a region close to the surface, including the investigation of the mechanisms of bubble formation, growth and detachment.[28] In these works, there is consensus that bubbles disturb the electrical behaviour of electrochemical reactors.[30,32] However, to the best of our knowledge, electrochemical conditions where a Taylor flow is established in a microchannel carrying out organic transformations was never investigated before.

Some authors have proposed models to describe and investigate electrochemical system with gas evolving from the electrodes.[29,31,33–37,41] These works range from 1D to 2D approaches with different degrees of complexity where essentially electrolyzers were evaluated under bubbly flow conditions. A model describing gas–liquid flow in electrochemical reactors carrying out organic synthesis with Taylor flow pattern through CFD techniques is essentially hitherto not reported, and it is the subject of this study. In contrast to most other chemical processes (Figure 6.1), we show that the presence of a gas bubble completely shuts down the electrochemical transformation in the film region. Also, we investigate the mixing behavior in the Taylor slugs found in such devices. We believe the insights provided in this manuscript will be helpful for the design of future electrochemical reactors and the execution of flow electrochemical transformations.

6.2 Method

For the setup, the micro flow electrochemical reactor (Figure 6.2) was designed by our group and described in detail elsewhere.[38] The reinforcement part was made of stainless steel (SAE international type 316L), offering adequate force for a closed plate and frame system with polytetrafluoroethylene (PTFE) spacer that provided chemical resistance and appropriate elastic modulus (proper stiffness for mechanical strength, suitable elastic deformation to prevent leakages). The insulated spacer partitioned the reactive chamber into 8 channels. The electrode plates were made of super fine graphite AC-K800 (anode) and phosphorus

deoxidized copper Cu-DHP (cathode).

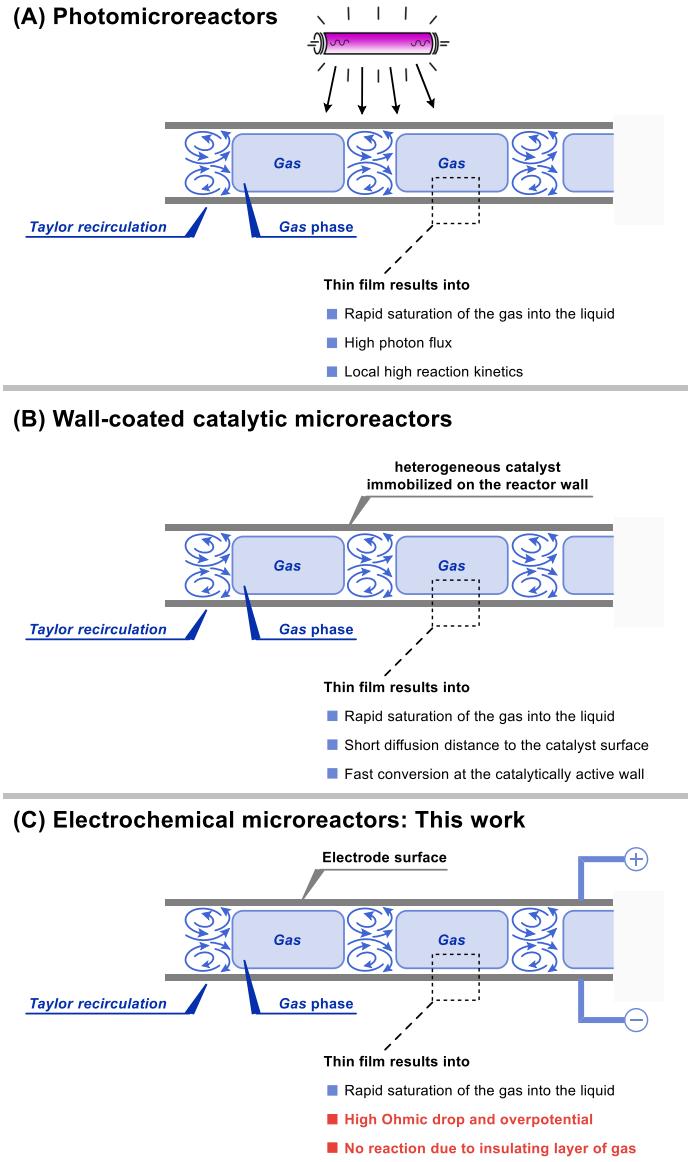

Figure 6.1 Influence of Taylor flow regime on different reaction types: (A) Photomicroreactors, (B) Wall-coated catalytic microreactors, (C) Electrochemical microreactors. In the case of A & B, the addition of gas has positive impact on the reaction.

As the benchmark reaction, the electrocatalytic hydrogenation of furfural was studied for experimental validation of the electrochemical gas–liquid reactive flow.[39] Syringe pumps (Fusion 720, Chemyx) were used to introduce the liquid reagents into the reactor. For the nonreactive gas–liquid ratio test, the bubble effect was correlated to the gas–liquid ratio. It should be noted that the calculated gas–liquid flow effects therefore reflects the actual flow regime of the electrochemical microsystem.

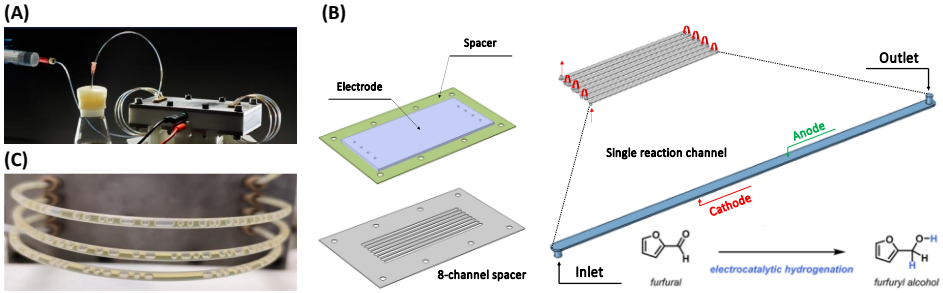

Figure 6.2 Experimental setup: (A) overview of the electrochemical reactor and the tubing,[21] (B) detailed view of the standard configuration, composed by 8 interconnected channels, and (C) view of the gas-liquid flow established in the tubing when furfural electrocatalytic hydrogenation to form furfuryl alcohol takes place in the reactor.

6.3 Mathematical modeling

The gas–liquid Taylor flow inside the electrochemical device was represented by a 2D model, as depicted in Figure 6.3. The full domain (Figure 6.3 A) is composed by two flow development zones and an active zone. In particular, the active zone represents the region where the bubbles are located, generating recirculation of the liquid flow within the slug and reactive mass transfer of the model chemical species. Also, this active zone contains the electrodes (cathode at the bottom wall and anode at the upper wall). The interelectrode distance (H) was set as 250 µm, representing the reference experimental setup.[38] The reactive zone was composed by an array of six bubbles, with unit cell features depicted in Figure 6.3 B. The reference bubble length (L_B) was set as $L_B = 2H$. Moreover, the slug half-length was defined as $L_S/2 = 0.667H$. Therefore, the length of the reactive zone was 5.0 mm, while each

of the flow development zones had a length of 1.67 mm. A liquid film with reference thickness = 5 µm was considered. The bubble was the reference frame in all the simulations, thus it was assumed to be fixed while at the electrodes (bottom and upper walls) a negative velocity was imposed, equal to the bubble velocity (U_B). The regions representing the gas bubbles were empty in the model.

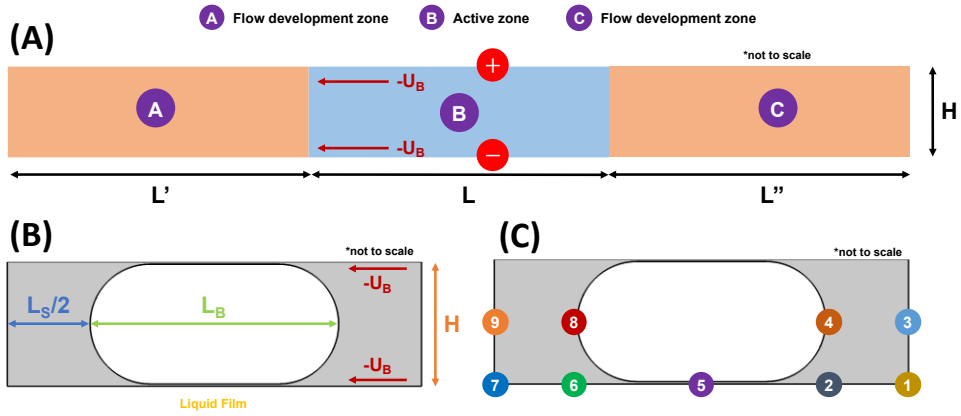

Figure 6.3 The CFD model: (A) an overview of the computational domain, (B) details of an unit cell, and (C) points where the concentration of furfural was recorded along time (5.0 s in total).

Based on the reference experimental setup, ethanol was selected as the liquid flowing in the system, while furfural was used as model species. Since furfural was diluted in the mixture, the transport properties of ethanol were assumed as effective and used in all the simulations. In addition, a reference diffusivity (D_{AB}) of 10^{-9} m^2/s was adopted.

The mathematical model consists of a set of nonlinear differential equations describing the two-dimensional, steady-state, single-phase (electrolyte domain) and incompressible problem. It should be highlighted that the assumption of steady state and single-phase flow (solving the electrolyte domain) was possible due to the approach adopted herein, considering the bubble as reference frame. Table 6.1 presents the mass, momentum and species conservation equations solved in the computational domain.

Table 6.1 Governing equations solved in the computational domain.

Mass conservation

$$\frac{\partial v_x}{\partial x} + \frac{\partial v_y}{\partial y} = 0 \tag{1}$$

Momentum conservation

$$\rho\left(v_x\frac{\partial v_x}{\partial x} + v_y\frac{\partial v_x}{\partial y}\right) = -\frac{\partial P}{\partial x} - \left[\frac{\partial \tau_{xx}}{\partial x} + \frac{\partial \tau_{yx}}{\partial y}\right] \tag{2}$$

$$\rho\left(v_x\frac{\partial v_y}{\partial x} + v_y\frac{\partial v_y}{\partial y}\right) = -\frac{\partial P}{\partial y} - \left[\frac{\partial \tau_{xy}}{\partial x} + \frac{\partial \tau_{yy}}{\partial y}\right] \tag{3}$$

$$\tau_{xx} = -\mu\left[2\frac{\partial v_x}{\partial x}\right] + \frac{2}{3}\mu\left(\frac{\partial v_x}{\partial x} + \frac{\partial v_y}{\partial y}\right) \tag{4}$$

$$\tau_{yy} = -\mu\left[2\frac{\partial v_y}{\partial y}\right] + \frac{2}{3}\mu\left(\frac{\partial v_x}{\partial x} + \frac{\partial v_y}{\partial y}\right) \tag{5}$$

$$\tau_{xy} = \tau_{yx} = -\mu\left[\frac{\partial v_y}{\partial x} + \frac{\partial v_x}{\partial y}\right] \tag{6}$$

Species conservation

$$v_x\frac{\partial C_i}{\partial x} + v_y\frac{\partial C_i}{\partial y} - \frac{\partial J_{i,x}}{\partial x} - \frac{\partial J_{i,y}}{\partial y} = 0 \tag{7}$$

$$J_{i,x} = -D_{AB}\frac{\partial C_i}{\partial x} \tag{8}$$

$$\boldsymbol{J_{i,y} = -D_{AB}\frac{\partial C_i}{\partial y}} \tag{9}$$

6.4 Boundary conditions

To solve the set of partial differential equations that represents this system, boundary conditions must be properly specified. In particular, the problem can be divided into three sub-problems: 1) fluid flow, 2) species transport and 3) electrochemistry, all of them coupled and nonlinear.

To solve the Taylor flow, an iterative procedure was adopted to set the proper boundary conditions. Initially, the velocity profile of ethanol flowing in a channel with the same height

H was obtained in the fully developed zone, considering an average entrance velocity of 1.436 mm/s (which yields an average residence time of 10 min in the experimental setup of reference) and lab reference frame (fixed walls with no-slip condition and $v_x = v_y = 0$). Then, we found the velocity $-U_B$ imposed at the channel bottom and upper walls (under no-slip condition and according to the scheme presented in Figure 6.3) that results in the same velocity profile ($U_{TP} = U_B + U_L$, where U_{TP} is the velocity of the two-phase flow, U_B is the bubble velocity and U_L is the liquid velocity) in the fully developed flow zone of the domain containing the bubbles. Null pressure difference (P = 0) was considered at the ends of the domain. At the gas–liquid interface (bubble walls), a slip condition was imposed (i.e., the gas and liquid velocities are the same at each point of the gas–liquid interface).

For the reactive gas, a saturation concentration (C_{sat} = 0.1 M, based on the experimental reference setup) of the model species was imposed at the entire surface of each bubble. The species reaching the bottom wall surface was reduced through concentration-dependent Butler Volmer kinetics expressed according to Eqs. (10) and (11)

$$r_i'' = \frac{\nu_i \cdot i_{loc}}{n \cdot F} \tag{10}$$

$$i_{loc} = i_0 \left[C_R \cdot exp\left(\frac{\alpha_a F \eta}{RT}\right) - C_O \cdot exp\left(\frac{-\alpha_c F \eta}{RT}\right) \right] \tag{11}$$

where r_i'' is the rate of reduction of species i at the cathode's surface (mol/m^2·s), ν_i is the stoichiometric coefficient (= -1, dimensionless), i_{loc} is the local current density (A/m^2), n is the number of electrons participating in the reaction (= 2, dimensionless), F is the Faraday constant (= 96485.3 C/mol), i_0 is the exchange current density (A/m^2), C_R and C_O are the concentration of reduced (= 0) and oxidized (= C_i/C_{sat}, dimensionless), respectively, α_a and α_c are the anodic and cathodic transfer coefficients (both = 0.5, dimensionless), respectively, R is the universal gas constant (= 8.314 J/mol·K), T is the temperature (= 293.15 K) and η is the overpotential (= $\phi_{s,ext} - \phi_l - E_{eq}$ in V; $\phi_{s,ext}$ is the external potential applied to the electrode, equal to -2.2 V, ϕ_l is the electrolyte potential and E_{eq} is the equilibrium potential, equal to -1.23 V). The value of the exchange current density parameter (i_0) was set as 1.0 A/m^2.

At the surface of the anode (upper wall), a linearized Butler-Volmer kinetics was imposed,

according to Eq. (12).

$$i_{loc} = i_0 \left[\frac{(\alpha_a + \alpha_c)F}{RT} \right] \eta \tag{12}$$

This condition arises from the naturally fast oxidation reactions that eventually results in gas evolution at the anode. Different values for the exchange current density (i_0) were evaluated (10, 1.0 and 0.1 A/m^2; 10 A/m^2 taken as reference). A scenario in which the anode kinetics is neglected was also considered, assuming that the electrolyte potential is zero at the electrode surface.

In the case of inert gas, the saturation concentration was imposed at the upper surface (along the entire channel). This condition was chosen based on the verification that the concentration of the model species varies insignificantly at this region along the active zone. Moreover, this condition represents a proper scenario for the assumption of steady state in the system under study.

A complementary study was carried out considering that a catalyst is deposited at the bottom wall of the reactor, resulting in the consumption of the model species by a first order kinetics ($r_i'' = kC_i$). The specific reaction rate k was chosen to be equal to $2 \cdot 10^{-6}$ m/s in order to match the averaged k-value coming from the concentration-dependent Butler-Volmer kinetics at the cathode surface. Null gradient of species i was assumed at the domain ends.

6.5 Computational procedure

All the numerical simulations were carried out with the finite element-based commercial code COMSOL® Multiphysics. The entire computational domain was discretized in a total of ~3.6×10^5 elements. Boundary layer elements (in a total of eight) were specified at the electrode surfaces and at the gas–liquid interface (bubble's surfaces). A mesh independence study was carried out to ensure that the results are independent of the grid refinement level.

As previously mentioned, the bubble reference frame was adopted in this study since the system under investigation presents steady state features. A system in which only a liquid

phase is present between the two electrodes was also investigated, in order to provide an overview of the phenomena when no bubbles are present. In this particular case, the lab reference frame was adopted, i.e., the walls were fixed and a no-slip boundary condition with $v_x = 0$ at the wall surfaces was adopted. The same operational conditions (concentration and velocity) were adopted. Two cases were investigated: 1) concentration-dependent Butler-Volmer kinetics at the cathode's surface and linearized Butler-Volmer kinetics at the anode's surface with i_0 = 10 A/m^2 and 2) concentration-dependent Butler-Volmer kinetics at the cathode's surface and negligible kinetics at the anode surface (null electrolyte potential at this wall). The reaction was allowed to occur throughout the entire channel, but a selected window at the center of the channel (with the same length of a bubble unit cell, i.e., $L_B + L_S$) was chosen for better visualization.

A complementary time-dependent study was carried out to investigate the fate of the model species departing from the surface of a single bubble. In this case, the entire computational domain was initially free from furfural, and the fluid flow of ethanol was solved in steady state, providing the velocity field in the system. Next, a rectangular pulse of furfural (0 mol/m^3 → 100 mol/m^3, i.e. C_{sat} → 0 mol/m^3) was introduced at the surface of the chosen bubble (an internal one in the array, allowing to properly capture the effect of the recirculation at the bubble nose and rear) from 0.1 s to 0.3 s (with a transition zone of 0.1 s). The fate of the species in the system, under the absence of chemical reaction, was monitored during 5.0 s in total. The concentration of furfural at the bubble's surface, at the middle of the liquid film close to the cathode surface and near the bubble nose and rear was then recorded at the points indicated in Figure 6.3 C.

6.6 Results and discussion

Initial assessment

We commenced our investigations by calculating an electrochemical situation in the absence of any gas. The reactor channel geometry is based on an in-house developed electrochemical flow cell with an interelectrode distance of 250 µm.[38,40,42] Further, we assumed a fully developed laminar flow profile and thus potential entrance effects are neglected. Under such conditions, a uniform electric field is obtained with normal current density and potential

profiles (Figure 6.4 A & B). The starting material is gradually consumed at the working electrode (Figure 6.4 C & E) and the entire electrode surface is active and productively used for the electrochemical process (Figure 6.4 D) as the absolute current density is constant over the entire surface.

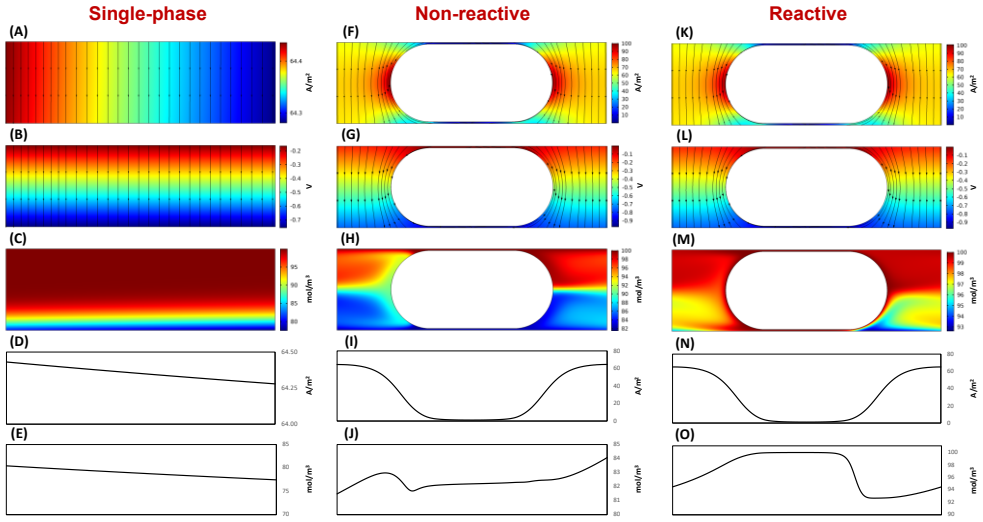

Figure 6.4 Calculated properties for single-phase flow electrochemistry: (A) electrolyte current density, (B) electrolyte potential, (C) concentration of the starting material, (D) absolute current density profile at the electrode surface, and (E) concentration profile of starting material. Calculated properties for gas-liquid flow electrochemistry in the Taylor flow regime using a non-reactive gas: (F) electrolyte current density, (G) electrolyte potential, (H) concentration of the starting material, (I) absolute current density profile at the electrode surface, and (J) concentration profile of starting material. Calculated properties for gas-liquid flow electrochemistry in the Taylor flow regime using a reactive gas: (K) electrolyte current density, (L) electrolyte potential, (M) concentration of the starting material, (N) absolute current density profile at the electrode surface, and (O) concentration profile of starting material.

Next, we investigated a scenario where inert gas is added to the reaction mixture (Figure 6.4 F-J). Inert gasses, such as nitrogen, are sometimes added to increase the mixing efficiency or they are formed as a byproduct at the counter electrode, e.g. formation of hydrogen or oxygen.

We specifically computed the scenario where a fully developed Taylor-flow regime is established. This is the most common regime for gas–liquid reaction conditions in microchannels and a stable Taylor flow can be established for a wide range of different gas and liquid velocities.

The presence of the gas bubble presents a local situation with infinite electrical resistance,[32] which increases the overall energy losses of the flow cell (Figure 6.4 F–J).[43] Notably, the gas bubble imposes a severe deformation of the electric field and the associated potential and current density in the electrolyte (Figure 6.4 F & G). Indeed, the region of the liquid film becomes a critical zone, where a minimum current density (Figure 6.4 I) and reaction rate is observed (Figure 6.4 H). As a consequence, the electrochemical reduction only happens along the length of the liquid slug at the cathode surface, and not in the liquid film (Figure 6.4 J).

As both the gas and liquid phase are moving forward, the electrochemical surface displays an on-again/off-again electrochemical activity.[44] If the gas bubble and liquid slug are of similar length, it can be easily understood that the electrochemical surface is only half of the time active. Hence, the remaining uncovered surface has to produce a higher current density to compensate for the loss of electroactive area. Consequently, an increase in overpotential and kinetic losses are observed, thus representing a sub-optimal operation of the reactor. Increasing the electrical conductivity of the liquid, e.g. by increasing the amount of electrolyte, leads to a higher current density and consequently reaction rate in the liquid slug, but it does not alleviate the non-reactive behavior in the liquid film.

Finally, a scenario with a reactive gas is considered (Figure 6.4 K–O), which is relevant for electrochemical transformations, such as CO_2 reduction and fuel cells.[45] While the application of gaseous reagents in electrochemical synthetic organic chemistry is currently limited,[21] an increase in research can be anticipated given the surging popularity of synthetic electrochemistry. Under these conditions, the reactive species first dissolves in the liquid phase after which it diffuses to the electrode surface and is able to react. Similar to what was found for an inert gas bubble, the current density is almost depleted in the region of the liquid film and thus low reaction rates are observed (Figure 6.4 K–M). This observation appears to be general for a variety of different diffusivities and liquid film thicknesses.

However, it should be noted that the film region is crucial for the mass transfer of the gas to the liquid phase, i.e. the overall gas-to-liquid mass transfer is dominated by the contribution from the gas bubbles to the film. This causes a saturation of the reactant in the film region due to the reduced reaction rate occurring in this zone. Interestingly, a fraction of the molecules dissolved in the liquid are pushed back to the slug ahead of the gas bubble due to the flow pattern in this region, where they have another chance to diffuse and react at the surface of the electrode.

Given these conditions, different concentration profiles are observed when taking into account non-reactive and reactive gas scenarios (clearly noticed when comparing Figure 6.4 H, M or J, O). In the case of reactive bubbles, the species is consumed in the liquid slug portion ahead of the bubble, but its concentration increases along the liquid film region, as previously mentioned. Then, the species is consumed again in the liquid slug portion behind the bubble. This behavior is repeated periodically for each bubble inside the reactor (leading to equal concentrations at the ends of a line crossing the unit cell in the midpoint of the bottom liquid film, i.e. Figure 6.4 O). In case of a non-reactive gas a distinct behavior can be noticed. When looking to Figure 6.4 J (also representing the concentration profile along a line crossing the unit cell in the midpoint of the bottom liquid film), one can observe that the species is consumed in the liquid slug ahead of the bubble and its concentration slightly changes along the liquid film. In the liquid slug portion behind the bubble there is a slight increase in the species concentration due to the fast mixing arising from the Taylor recirculation associated with the concentration gradient existing between the upper and bottom portions of the interelectrode space. As one moves in counterflow direction, more pronounced is the concentration jump behind the bubble since the concentration gradient is higher between the upper and the bottom portions of the interelectrode distance. Finally, the species concentration decreases along the liquid slug behind the non-reactive bubble, as expected.

Residence time distribution in the liquid slug

Molecules reaching the liquid film have a small chance to react, but display an excellent residence time distribution (RTD) (see Figure 6.5 A, point 5). Molecules reaching the slug close to the rear interface of the gas bubble have a higher chance to react and show some

non-ideality in the RTD. The recirculation pattern in this region intensifies the mixing, as we can notice especially in points 7, 8 and 9 of Figure 6.5 A. In contrast, the core of the slug exhibits improved current densities but is less accessible to the molecules coming from the gas bubbles. These molecules are transported via convection in a complex recirculating flow pattern and witness a relatively poor RTD, as we can notice particularly in point 9 of Figure 6.5 A. Interestingly, the opposite behavior is observed at the bubble nose. Here, the region close to the cathode presents a relatively poor RTD compared to the slug core. Again, we can notice the mixing induced by the recirculation pattern in the region (clear in points 1 and 2 of Figure 6.5 A). Figure 6.5 B shows contours of the model species concentration time-dependent evolution in an interval of 5 s (supported by the video available in this link), considering a single bubble as a source. The mixing induced by the recirculation in the liquid slug can be clearly noticed from Figure 6.5 B.

Sensitivity analysis

We also investigated the effect of operational parameters, namely electrolyte velocity, bubble size, gas holdup, interelectrode distance and concentration, on the performance of the electrochemical reactor.

Figure 6.6 presents the overpotential for (A) larger and (B) smaller reactive bubbles, and (C) larger and (D) smaller non-reactive bubbles, and the current density for (E) larger and (F) smaller reactive bubbles, and (G) larger and (H) smaller non-reactive bubbles, both as a function of the electrolyte velocity and the concentration. In all cases the interelectrode distance (250 μm) and the gas holdup (~0.5) were kept constant. Larger bubbles correspond to a length LB, while smaller bubbles have length $L_B/2$. The effect of varying the electrolyte velocity is represented herein by the operator β, a multiple of the velocity adopted in the reference experimental setup.

An increase in the electrolyte velocity tends to increase the current density and decrease the overpotential in all cases, with a more pronounced effect when lower concentrations are considered. Moreover, the impact of the electrolyte velocity on the system performance within the species concentration space is more pronounced in the case of nonreactive bubbles.

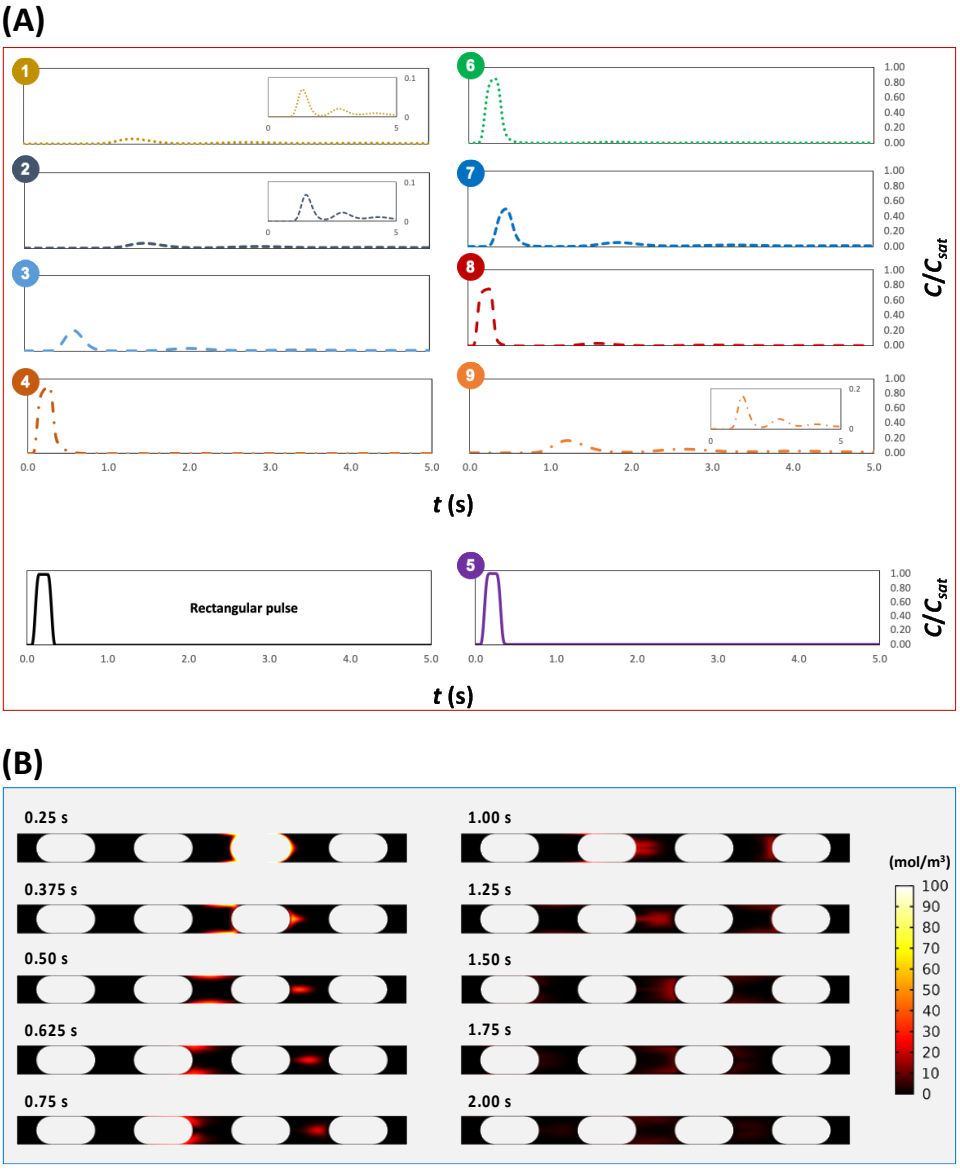

Figure 6.5 (A) Concentration profiles of the model species obtained at the points indicated in Figure 6.3 C in the interval of 5.0 s. (B) Concentration map of the model species after a rectangular pulse at the gas-liquid interface. The color bar expresses the concentration of the model species in mol/m^3. More details in the video available in this link showing the evolution of the model species concentration in an interval of 5.0 s.

Higher electrolyte velocities result in more intense recirculation in the liquid slug. However, as the electrolyte velocity reaches a certain limit, a further increase does not result in a significant decrease in the overpotential and an increase in the current density as the mass transfer limitations are minimized. This behavior is more pronounced for lower concentrations, where the effect of mass transfer limitations is expected to be indeed more relevant.

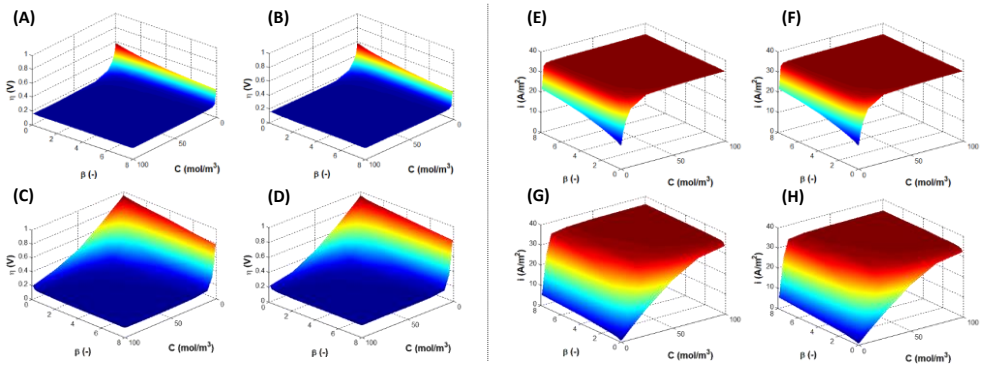

Figure 6.6 Overpotential as a function of the electrolyte velocity and concentration for (A) larger and (B) smaller reactive bubbles, and (C) larger and (D) smaller nonreactive bubbles. Current density as a function of the electrolyte velocity and concentration for (E) larger and (F) smaller reactive bubbles, and (G) larger and (H) smaller non-reactive bubbles. In all cases a gas holdup of ~0.5 is considered.

The same dependence on the electrolyte velocity and concentration is noticed when the interelectrode distance is varied, according to Figure 6.7, i.e., the overpotential tends to decrease while the current density tends to increase as the electrolyte velocity is increased, keeping the bubble size (larger bubble) and the gas holdup (~0.5) constant.

When the interelectrode gap is increased according to the path 0.5H → H → 2H (with H = 250 µm being the reference interelectrode distance), the average current density calculated at the cathode and the overpotential tends to decrease, both for reactive and non-reactive bubbles. Interestingly, the extent of the variation of these quantities with the electrolyte velocity is higher within the concentration space for reduced interelectrode distances (i.e.,

the sensitiveness is inversely proportional to the interelectrode gap). Particularly in the case of reactive bubbles, the dependence of the overpotential and the current density with the electrolyte velocity is relevant for very diluted solutions when the interelectrode gap 2H is considered.

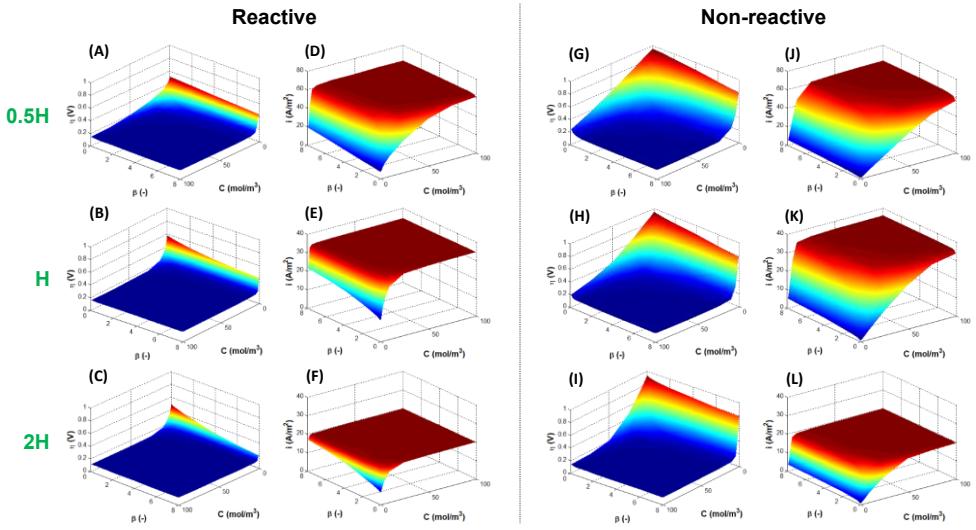

Figure 6.7 Effect of the interelectrode distance on the overpotential and current density under different values of electrolyte velocity and concentration for reactive and non-reactive bubbles: (A)-(C) overpotential and (D)-(F) current density for interelectrode distances of 0.5H, H and 2H and reactive bubbles; (G)-(I) overpotential and (J)-(L) current density for interelectrode distances of 0.5H, H and 2H and non-reactive bubbles. The interelectrode distance H corresponds to 250 µm (experimental reference). In all cases a condition of larger bubbles and gas holdup of ~0.5 is considered.

The effect of varying the gas holdup for a given reactive bubble size (larger bubble) and interelectrode distance (250 µm) was also investigated. Figure 6.8 shows (A) overpotential and (B) current density as a function of electrolyte velocity and concentration for a gas holdup of ~0.5, and (C) overpotential and (D) current density as a function of electrolyte velocity and concentration for a gas holdup of ~0.25.

Overall, the current density and the overpotential increased when the gas holdup decreased.

Within a given gas holdup, the behavior previously noticed is also observed, i.e., the overpotential decreases while the current density increases as the electrolyte velocity is increased, reaching a plateau for higher electrolyte velocities. The effect of varying the electrolyte velocity in the concentration space is more pronounced as the gas holdup is decreased. A higher current density is observed for the case of lower gas holdup since in this case the disturbance induced by the gas bubbles on the electric field is diminished. Also, at lower gas holdups the length of the liquid slug is higher and consequently the mixing effect induced by the recirculation is less pronounced, resulting in lower sensitivity for the overpotential and the current density when the electrolyte velocity is varied in the concentration space, i.e. higher electrolyte velocities are required to reach a plateau where the mass transfer limitations vanish, especially at lower concentrations.

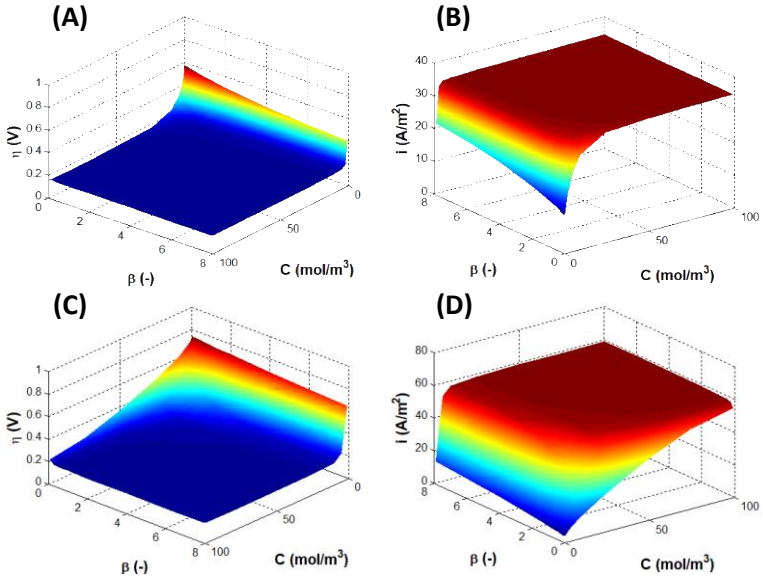

Figure 6.8 (A) overpotential and (B) current density as a function of electrolyte velocity and concentration for a gas holdup of ~0.5; (C) overpotential and (D) current density as a function of electrolyte velocity and concentration for a gas holdup of ~0.25. In all cases, reactive larger bubbles and an interelectrode distance H are considered.

Finally, an assessment of the bubble-induced mixing on the performance of the

electrochemical reactor was performed, complementing the results reported in Figures 6.6-6.8. Figure 6.9 presents the (A) overpotential and the (B) current density as a function of the electrolyte velocity and the concentration for larger non-reactive bubbles under fixed gas holdup (~0.5) and interelectrode distance (250 µm). Moreover, a complementary study was carried out in a condition of no flow in the absence of bubbles in the same computational domain. Figure 6.9 (C) and (D) presents the overpotential and the current density for this case. In all the scenarios studied, the concentration is indexed 1–4 corresponding to 1 mol/m^3, 10 mol/m^3, 50 mol/m^3 and 100 mol/m^3, respectively.

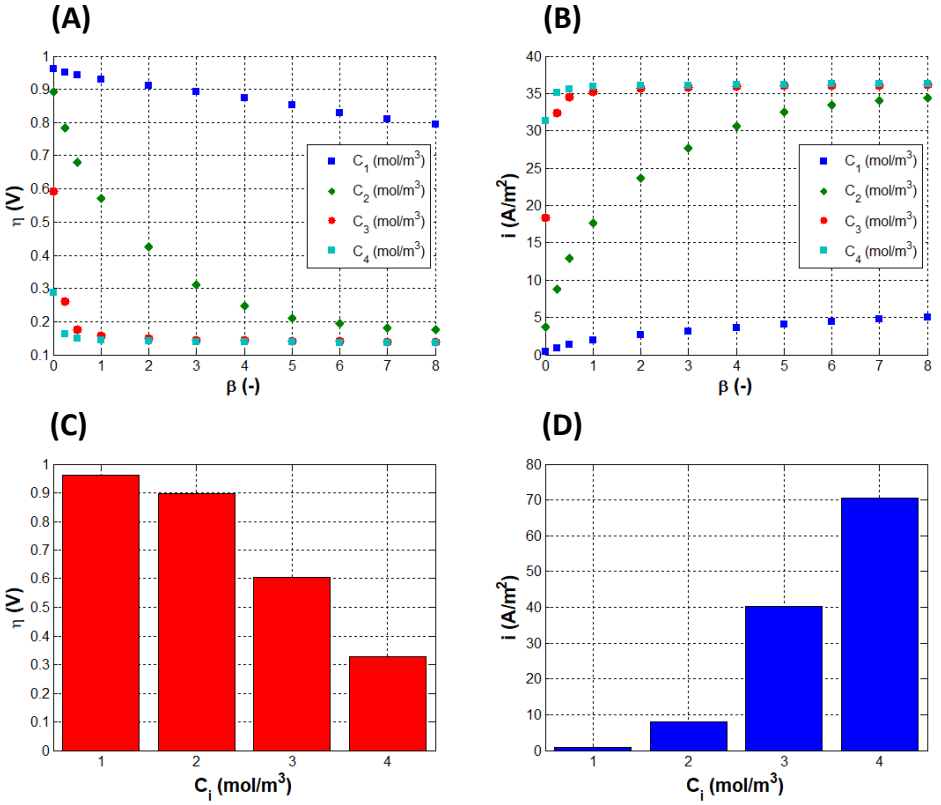

Figure 6.9 (A) overpotential and (B) current density as a function of the electrolyte velocity and the concentration for larger non-reactive bubbles under fixed gas holdup (~0.5) and interelectrode distance (250 µm); (C) overpotential and (D) current density for a condition of no flow in the same computational domain in the absence of bubbles. The concentration equals to 1 mol/m3, 10 mol/m3, 50 mol/m3 and 100 mol/m3 for indexes 1–4, respectively.

From Figure 6.9 (A) and (B), we can observe that as the electrolyte velocity approaches zero, the overpotential of the system containing bubbles approximates to the condition of no bubbles, although always remains slightly higher for the homogeneous case (absence of bubbles). Similarly, the current density follows the same trend when the electrolyte velocity is close to zero, although the values calculated for the homogenous channel are always significantly higher than those recorded for the domain containing bubbles (~2x higher), in accordance with the previous discussion. As the electrolyte velocity increases, there is a decrease in the overpotential and an increase in the current density tending to a plateau in the region where the mass transfer limitations vanish. Therefore, increasing the electrolyte velocity induces a more intense mixing in the liquid slug contributing to improve the performance of the system containing bubbles, up to a certain limit. Clearly, the plateau reached for the current density is not as high as the value for the channel with absence of bubbles due to the disturbances that the bubbles induce in the electrical field.

Mitigation mechanisms and outlook

Using computational fluid dynamics, we calculated different scenarios for a gas–liquid Taylor flow regime in an electrochemical microflow reactor. This flow regime has proven its value in a variety of chemical applications. However, our results show convincingly that Taylor flow complicates the electrochemical process when carried out in microreactors.

The gas bubble acts as an insulator resulting in a high energy loss, which prevents any reaction to occur in the bubble region. As the bubble moves over the electrode surface, this leads to an on-again/off-again operation of the local electrochemical surface. The larger the bubble becomes the less efficient the reactor is used, resulting in a higher overall energy consumption for the electrochemical process. As an extreme case, we can consider annular flow or pipe flow where the gas flows at a higher velocity in the centre of the microchannel and the liquid lubricates the electrodes and the reactor walls. It is evident that such a scenario should be avoided at all costs.

While Taylor flow still leads to an increase in mass transfer in flow electrochemistry, we have shown that this advantage does not outweigh the disadvantages as described herein. Following previous contributions in the literature that propose ways to overcome this issue,

we propose three potential solutions.

A first option is to apply elevated pressures which increases the solubility of the gas in the liquid and reduces the average volume of the bubbles.[46] However, this has to be evaluated on a case-by-case scenario as elevated pressures can shift the chemical equilibria (Le Chatelier's principle) and thus can give rise to byproduct formation.[32,47]

A second solution to overcome the limitations of Taylor gas–liquid flow could be the use of gas-diffusion electrodes. These porous electrodes enable efficient contact between the gas, the liquid phase and the electroactive surface.[48] The electrodes can be installed in such a way that the interelectrode gap is filled with the conducting electrolyte solution, while the gas phase is flowing on the opposite side.[49] Hence, an intimate contact between the gas and the liquid is established without passivating the electroactive surface. Also, in the case of gaseous byproduct formation, the gasses can be effectively removed through the gas-permeable electrode by applying a vacuum.

Third, surfactants can be added to the reaction solution, which lowers the surface tension. For gas-evolving reactions (e.g. hydrogen evolution), this leads not only into a faster detachment of the gas from the electrodes but it also results in a reduction of the average bubble size of the gas phase.[50] In addition, it has been shown that a reduction of the bubble size is accompanied by a significant improvement of the current efficiency.[51]

6.7 Conclusions

We investigated the effect of gas bubbles in Taylor-flow regimes in electrochemical microreactors using a computational fluid dynamics model. We have shown that the presence of the gas bubbles in Taylor flow has controversial effects. From the electrochemical stance, the presence of bubbles results in disturbances in the current distribution. However, due to Taylor vortices, the presence of bubbles intensifies the mixing efficiency in the liquid slug allowing to minimize mass transfer limitations. We have studied different scenarios, including the absence and presence of both reactive and unreactive gases. Furthermore, an indepth analysis was performed taking into account the residence time distribution of molecules in the liquid slug and the effect of different operational variables (bubble size, gas

holdup, interelectrode distance, electrolyte velocity and concentration) on the overpotential and current density. Finally, a discussion about strategies to overcome these issues was presented.

We anticipate that the insights gained herein will be of importance to the community to develop improved and more energy-efficient gas–liquid electrochemical flow cells. We believe the results are also significant for the large-scale electrochemical production of chemicals as these are often carried out in narrow-gap flow cells.[21]

References

[1] Noël T, Cao Y, Laudadio G (2019). Acc Chem Res 52:2858–2869
[2] Obama B (2017). Science (80-) 355:126–129
[3] Haase S, Murzin DY, Salmi T (2016). Chem Eng Res Des 113:304–329
[4] Cao Y, Noël T (2019). Org Process Res Dev 23:403–408
[5] Sobieszuk P, Aubin J, Pohorecki R (2012). Chem Eng Technol 35:1346–1358
[6] Padoin N, Dal'Toé ATO, Rangel LP, Ropelato K, Soares C (2014). Int J Heat Mass Transf 73:239–249
[7] Cambié D, Bottecchia C, Straathof NJW, Hessel V, Noël T (2016). Chem Rev 116:10276–10341
[8] Poe SL, Cummings MA, Haaf MP, McQuade DT (2006). Angew Chemie Int Ed 45:1544–1548
[9] Karim A, Bravo J, Gorm D, Conant T, Datye A (2005). Catal Today 110:86–91
[10] Sebastian Cabeza V, Kuhn S, Kulkarni AA, Jensen KF (2012). Langmuir 28:7007–7013
[11] Günther A, Jensen KF (2006). Lab Chip 6:1487–1503
[12] Casnati A, Gemoets HPL, Motti E, Della Ca' N, Noël T (2018). Chem – A Eur J 24:14079–14083
[13] Nakano M, Nishiyama Y, Tanimoto H, Morimoto T, Kakiuchi K (2016). Org Process Res Dev 20:1626–1632
[14] Armaroli N, Balzani V (2011). Energy Environ Sci 4:3193–3222
[15] Laudadio G, de Smet W, Struik L, Cao Y, Noël T (2018). J Flow Chem 8:157–165
[16] Roibu A, Van Gerven T, Kuhn S (2020). ChemPhotoChem 4:5193–5200

[17] Sequeira CAC, Santos DMF, Šljukić B, Amaral L (2013). Brazilian J Phys 43:199–208
[18] Angulo A, van der Linde P, Gardeniers H, Modestino M, Fernández Rivas D (2020). Joule 4:555–579
[19] Botter W (1991). J Electrochem Soc 138:1028
[20] Han J-H, Hwang K, Jeong H, Byeon S-Y, Nam J-Y, Kim C-S, Kim H, Yang S, Choi JY, Jeong N (2019). J Appl Electrochem 49:517–528
[21] Gabrielli C, Huet F, Keddam M, Macias A, Sahar A (1989). J Appl Electrochem 19:617–629
[22] Bongenaar-Schlenter BE, Janssen LJJ, Van Stralen SJD, Barendrecht E (1985). J Appl Electrochem 15:537–548
[23] Taqieddin A, Nazari R, Rajic L, Alshawabkeh A (2017). J Electrochem Soc 164:E448–E459
[24] Křišťál J, Kodým R, Bouzek K, Jiřičný V (2008). Electrochem commun 10:204–207
[25] Yan M, Kawamata Y, Baran PS (2017). Chem Rev 117:13230–13319
[26] Maljuric S, Jud W, Kappe CO, Cantillo D (2020). J Flow Chem 10:181–190
[27] Jha K, Bauer GL, Weidner JW (2000). J Appl Electrochem 30:85–93
[28] Zhao X, Ren H, Luo L (2019). Langmuir 35:5392–5408
[29] Drake JA, Radke CJ, Newman J (2001a). Ind Eng Chem Res 40:3109–3116
[30] Drake JA, Radke CJ, Newman J (2001b). Ind Eng Chem Res 40:3117–3126
[31] Mandin P, Hamburger J, Bessou S, Picard G (2005). Electrochim Acta 51:1140–1156
[32] Drake JA, Radke CJ, Newman J (2001c). Chem Eng Sci 56:5815–5834
[33] Mandin P, Aissa AA, Roustan H, Hamburger J, Picard G (2008). Chem Eng Process Process Intensif 47:1926–1932
[34] Křišťál J, Kodým R, Bouzek K, Jiřičný V (2011). Electrochem commun 13:750
[35] Wiebe A, Gieshoff T, Möhle S, Rodrigo E, Zirbes M, Waldvogel SR (2018). Angew Chemie Int Ed 57:5594–5619
[36] Cao Y, Adriaenssens B, de A. Bartolomeu A, Laudadio G, de Oliveira KT, Noël T (2020). J Flow Chem 10:191–197
[37] Laudadio G, Barmpoutsis E, Schotten C, Struik L, Govaerts S, Browne DL, Noël T (2019). J Am Chem Soc 141:5664–5668
[38] Qian K, Chen ZD, Chen JJJ (1998). J Appl Electrochem 28:1141–1145
[39] Polezhaev P, Slouka Z, Lindner J, Přibyl M (2018). Microelectron Eng 194:89–95

[40] Jhong H-R “Molly,” Ma S, Kenis PJA (2013). Curr Opin Chem Eng 2:191–199

[41] Mazloomi SK, Sulaiman N (2012). Renew Sustain Energy Rev 16:4257–4263

[42] Jud W, Kappe CO, Cantillo D (2020). ChemElectroChem 7:2777–2783

[43] Higgins D, Hahn C, Xiang C, Jaramillo TF, Weber AZ (2019). ACS Energy Lett 4:317–324

[44] Whipple DT, Finke EC, Kenis PJA (2010). Electrochem Solid-State Lett 13:B109

[45] Marken F, Wadhawan JD (2019). Acc Chem Res 52:3325–3338

[46] Eng JAC, Asari M, Hormozi F (2014). J Adv Chem Eng 04:1–5

[47] Folgueiras-Amador AA, Jolley KE, Birkin PR, Brown RCD, Pletcher D, Pickering S, Sharabi M, de Frutos O, Mateos C, Rincón JA (2019). Electrochem commun 100:6–10

[48] Tang S, Liu Y, Lei A (2018). Chem 4:27–45

[49] Mallia CJ, Baxendale IR (2016). Org Process Res Dev 20:327–360

[50] Atobe M, Tateno H, Matsumura Y (2018). Chem Rev 118:4541–4572

[51] Gupta R, Fletcher DF, Haynes BS (2010). J Comput Multiph Flows 2:1–31

Chapter 6

CHAPTER 7

CFD study on liquid-liquid Taylor flow electrochemistry

This chapter is based on:

Cao, Y.; Padoin, N.; Soares, C. and Noel, T. On the Performance of Liquid-Liquid Taylor Flow Electrochemistry in a Microreactor – A CFD Study. *submitted for publication.*

Abstract

A comprehensive understanding of the underlying phenomena (coupled fluid flow, charge transfer, mass transfer and chemical reaction) is fundamental for a proper design, analysis and scale-out of chemical reactors when carrying out multiphase electro-organic transformations. In this study, we have explored the novel combination of organic electrochemical synthesis and computational fluid dynamics (CFD) to perform a systematic theoretical investigation concerning the effect of different operational parameters on the performance of organic-aqueous Taylor flow in electrochemical microreactors. The results indicate that operating at high concentrations of the rate-limiting species (>5 mol·m^{-3} for $D_i \geq 10^{-9}$ m^2·s^{-1}; 500 mol·m^{-3} for $D_i \sim 10^{-10}$ m^2·s^{-1}) is beneficial for the reactor's performance. However, excessively high concentrations (>500 mol·m^{-3}) do not result in a further improvement in mass transfer and current/voltage relation. Higher diffusivities are also beneficial, but even in this scenario limiting current densities can be found when working at low concentrations. Overall, keeping an internal:external phase electrical conductivity ratio >1 improves the reactor performance. Working at lower velocities can be beneficial in some scenarios, since higher limiting current densities can be obtained. However, the velocity impact on the reactor performance is not significant in some operating conditions (e.g., at higher concentrations and diffusivities). Finally, working with higher cell potentials is beneficial, but limiting current densities can be encountered at lower concentrations and diffusivities. Variables such as internal phase volume fraction, droplet length and interelectrode distance also have relevant impact on the reactor performance, but are subjected to the same conditioning factors previously mentioned. A comprehensive potential balance was also conducted, showing the relative importance of the activation, Ohmic and concentration overpotentials under different operating conditions. We believe the insights gained herein will be of interest to researchers in both academia and industry to develop more efficient electrochemical flow reactors for liquid-liquid transformations.

7.1 Introduction

There is no doubt about the urgent need for an in-depth assessment of the current industrial standards for chemical transformations to enable greener and more efficient synthetic routes. Smart chemical plants will be required, which use automation and artificial intelligence to adjust the processes in real time, thus establishing highly selective and productive transformations.[1,2] In addition, the sustainability goals of the chemical industry can -at least partially- be achieved through the maxims of process intensification (PI).[3–9]

Multifunctional reactors[10-12], including monolithic designs[13-15], and micro-flow[16, 17] devices are the current standards for intensifying chemical transformation plants at the equipment level. Monolithic structures have been applied in electrochemical[18-20], photochemical[21] and thermally-activated catalytic reactions[22, 23]. Environmental protection, power plants and bulk chemicals can be listed among several sectors in which this technology has already been implemented, carrying out monophasic or multiphase flows.[23] Similarly, micro-flow chemistry, driven by photochemical[24,25] or electrochemical[26] activation modes, has attracted a great deal of attention in recent years due to the potential to use renewable energy sources. Microreactors have widely been recognized as a key equipment for Process Intensification as they provide high surface-to-volume ratios, short diffusion distances, high and reproducible interfacial areas.[27] Therefore, the combination of microreactors with photo-/electrochemistry is a perfect match to enable green process development focused on high efficiency with a reduction of the negative side effects to our planet.

The increased availability of green electricity has driven smart technologies in several areas, including transportation and the energy sector.[28,29] This fact has also pushed academia and industry towards a renewed interest in developing micro-flow electrochemical methodologies.[30] Electron-driven chemical activation is attractive not only from a sustainability perspective but also as a strategy to establish new synthetic transformations and to provide higher selectivities in conventional synthetic pathways.[31,32] While most of the electroorganic transformations are conducted in single-phase flow (i.e., with all species in solution), multiphase applications involving gas-liquid[33,34] and liquid-liquid flow,[35-37] often leading to the so-called Taylor flow,[38-40] are also encountered. The segmented flow regime

occurring in these devices leads to toroidal fluid circulation patterns,[39,40] allowing for increased radial heat and mass transfer while minimizing axial dispersion effects.

The theoretical understanding of the transport phenomena and the charge transfer processes occurring in multiphase micro-flow electrochemistry is of paramount importance for proper design, analysis and scale-out purposes. In a previous study[41] we have used computational fluid dynamics (CFD), a powerful tool for simulating the coupled nonlinear phenomena taking place in micro-flow chemistry,[42-48] to investigate the effect of mixing and charge transfer in gas-liquid micro-flow electro-organic transformations. Our calculations have shown that gas bubbles have controversial effects on the performance of these devices. This means that, while the presence of the bubbles intensify the mixing efficiency,[49-53] the gas bubbles also block the charge transfer and, thus, the chemical reaction shuts down around the gas bubble. -

Despite the fact that the fluid dynamics[54-57] and the associated heat[58-62] and mass[63-65] transport mechanisms of liquid-liquid flow processes are quite established, theoretical and/or experimental investigations of liquid-liquid electrochemical systems are hitherto only rarely reported.[66-69]

To the best of our knowledge, a systematic theoretical investigation of Taylor flow with coupled mass transfer, charge transfer and chemical reaction in liquid-liquid electro-organic transformations is currently missing. More specifically, we were interested in the charge and mass transfer behavior in such liquid-liquid micro-flow systems and the influence of different electrical conductivity ratios. Could the presence of an aqueous phase have a positive effect on electro-organic transformations in comparison to an equivalent homogeneous (single-phase) system? How different would the coupled nonlinear phenomena behave in liquid-liquid electro-organic systems when compared to the gas-liquid ones?

These questions have stimulated us to perform a study focused on the novel combination of CFD and liquid-liquid electro-organic transformations. The effect of different operational variables (electrical conductivity ratio, mass diffusivity, velocity, concentration, cell potential, internal phase volume fraction, internal phase length and inter-electrode distance) were systematically studied using CFD calculations. The investigation was mainly based on the

analysis of a potential distribution in the electrochemical microreactor (considering the contribution of ohmic, concentration and activation overpotential) and polarization curves. The electrochemical oxidative coupling between thiophenol and fluoride yielding sulfonyl fluorides[70,71]) was selected as a benchmark reaction and a typical modular electrochemical microreactor configuration was considered.[72] We believe that the insights provided herein will aid in the future design, analysis and scale-out of electrochemical flow reactors and the execution of micro-flow electro-organic transformations.

7.2 Electrochemical reactor and benchmark reaction

The micro-flow electrochemical reactor (Figure 1A) designed by our group and described in detail elsewhere[72] was considered for modeling purposes. In summary, the reactor comprises eight channels (allowing for different reactor configurations in series and parallel and consequent variable reaction volume) with an interelectrode distance of 250 μm and a width of 3 mm (Figure 7.1B).[71-73] This device represents a typical electrochemical microreactor for organic transformations, serving as a reference for the interelectrode distances and velocities adopted in our numerical investigations.

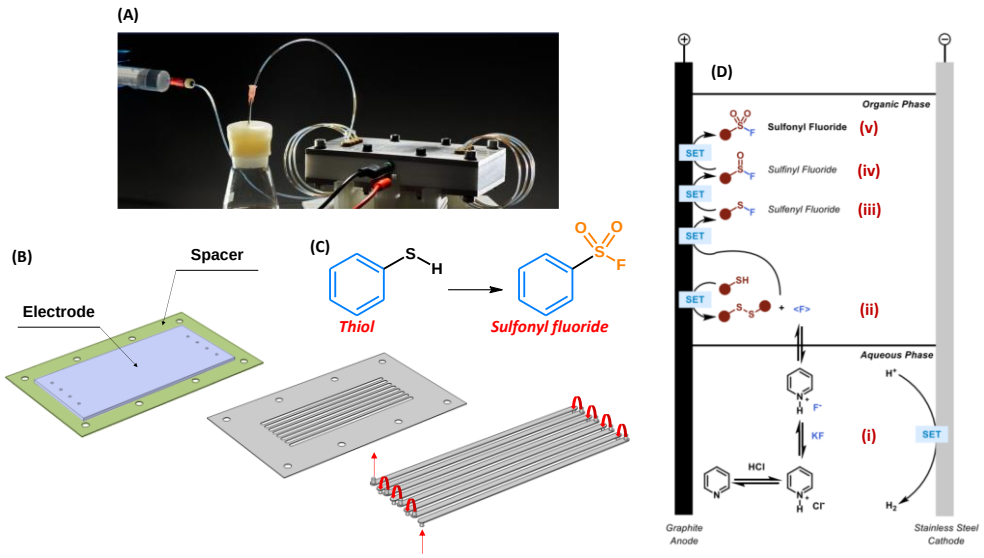

Figure 7.1 Overview of the reaction environment: (A) electrochemical reactor – external

view, (B) electrochemical reactor – internal view, (C) chemical transformation under study, and (D) reaction mechanism (reaction *ii* represents the rate limiting step at the anode's surface, since the steps *iii*-*v* represent click reaction mechanisms; step *i* represents KF dissociation, mediated by pyridine, and fluoride interfacial transfer from the aqueous to the organic phase).

Moreover, as a benchmark reaction with the kinetics at the anode as the rate-limiting step, the electrochemical oxidative coupling of thiophenol and fluoride yielding sulfonyl fluoride was considered (Figure 7.1C).[71] The reaction medium consists of a biphasic mixture composed of aqueous HCl solution and an organic CH_3CN phase. Thiophenol is used as the substrate, while KF was the fluoride source. Moreover, pyridine is added to produce high yields since it may act as a phase transfer catalyst and electron mediator, according to the mechanism illustrated in Figure 7.1D.

Following the mechanism proposed, reaction (ii) represents the rate-limiting step at the anode[70,74,75] while the other steps are considered to be fast as we were never able to isolate or observe those intermediates under the given reaction conditions. Furthermore, step (i) represents KF association with pyridine and fluoride interfacial transfer from the aqueous to the organic phase. The fluoride phase transfer occurs in the form of $C_5H_5NH^+$-F^- and controls the supply of this reagent to the anode surface. The optimal reaction condition is achieved with a residence time of 5-10 min and a cell potential of 3.30 V.[71] Again, this reaction environment was taken as a reference for the parametric study carried out numerically herein, considering the effects of different scenarios on the performance of liquid-liquid electrochemical transformations in micro-flow.

7.3 Mathematical modeling and computational procedure

Computational domain

The liquid-liquid flow inside the electrochemical microreactor can be represented by the scheme shown in Figure 7.2A, where Ω_1 is the internal (dispersed) phase and Ω_2 is the external (continuous) phase.

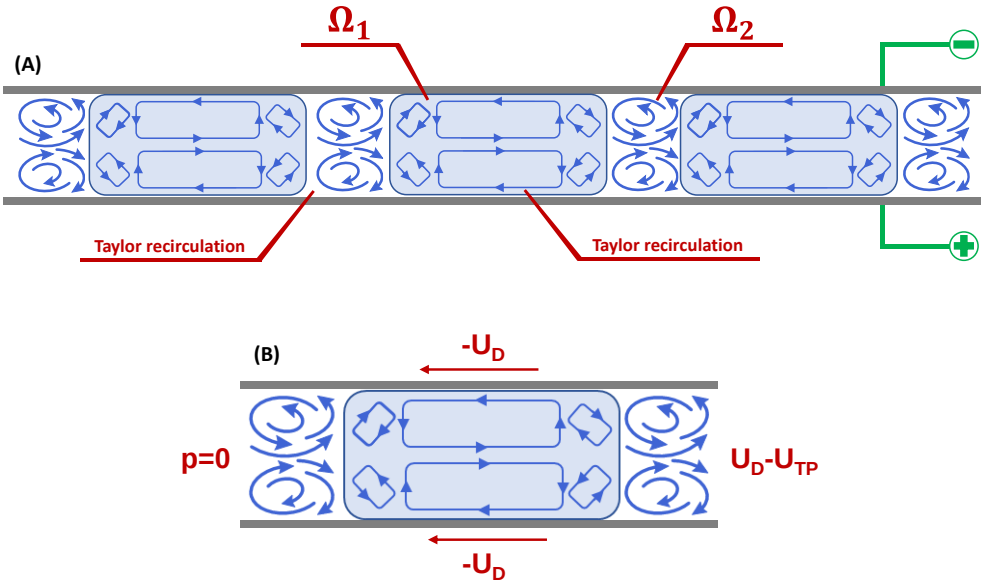

Figure 7.2 Biphasic flow occurring in the electrochemical reactor: (A) segmented flow (internal phase Ω_1 and external phase Ω_2 flowing periodically between the electrodes), and (B) a scheme of the unit cell considered in this work, with an indication of the boundary conditions adopted.

Taylor recirculation occurs in the external and internal phases. The subdomain Ω_1 repeats periodically along the reactor. Moreover, each subdomain Ω_1 represents a source for the limiting-rate species *i*. The two-phase flow occurs in the interelectrode gap (cathode placed at the upper plate and anode placed at the bottom plate). The electrochemically-driven chemical transformation occurs only at the anode surface.

The full domain was reduced to a 2D unit cell (UC) for modeling purposes, representing the periodical Taylor flow occurring throughout the reactor, depicted in Figure 7.2B. This unit cell was modeled, taking the disperse phase as the reference frame. Therefore, the droplet velocity U_D was imposed at the walls, while a relative velocity ($U_D - U_{TP}$; U_{TP} corresponding to the average two-phase velocity) and null gauge pressure were prescribed at the inlet and the outlet, respectively.

Fluid flow

The multiphase flow in the electrochemical device was calculated through the moving mesh Arbitrary Lagrangian–Eulerian (ALE) formulation[76-79] in COMSOL® Multiphysics. This enables precise flux calculations at fluid-fluid interfaces. Moreover, it allows a straightforward implementation of fluxes at fluid-fluid interfaces. Working with the moving mesh approach also provides an easy implementation of a known saturation concentration or a partition coefficient at the interface. Moreover, growth or shrinkage of the dispersed phase due to mass transfer at the interface can be easily implemented in COMSOL® Multiphysics using the moving mesh approach. Given the advantages of this method for the current and future investigations in this field, we have opted to use this approach in our simulations as an alternative to traditional multiphase models (e.g., level-set, phase field, etc.).

The two-dimensional, Newtonian, transient, laminar and incompressible flow occurring in the micro-electrochemical device was modeled according to Eqs. 1 and 2 (momentum and overall mass conservation, respectively):

$$\rho\left[\frac{\partial \boldsymbol{u}}{\partial t} + (\boldsymbol{u}_c \cdot \nabla)\boldsymbol{u}\right] = \nabla \cdot [-p\boldsymbol{I} + \mu(\nabla \boldsymbol{u} + (\nabla \boldsymbol{u})^T)] \quad (1)$$

$$\nabla \cdot \boldsymbol{u} = 0 \quad (2)$$

where $\boldsymbol{u}_c$ (m·s^{-1}) is the convective velocity, defined as the difference of material velocity and mesh velocity, and $\boldsymbol{u}$ (m·s^{-1}) is the mesh velocity. The gravitational force was neglected. (since viscous forces and surface tension are predominant, $Bo = \Delta\rho g D^2/\sigma = 0.13$).

At the inlet, fully developed laminar flow was adopted, while at the outlet, null gauge pressure was specified. At the upper and bottom walls, a tangential velocity was specified according to Eq. 3.

$$\boldsymbol{u} = U_w \boldsymbol{t} \quad (3)$$

where U_w (m·s^{-1}) is the velocity imposed at these boundaries and $\boldsymbol{t}$ (dimensionless) is the tangential vector at the walls.

At the liquid-liquid interface, the finite stresses are calculated according to Eq. 4 [10].

$$\boldsymbol{n} \cdot \boldsymbol{\tau}_1 = \boldsymbol{n} \cdot \boldsymbol{\tau}_2 + \boldsymbol{f}_{st} \quad (4)$$

where $\boldsymbol{\tau}_1$ (N·m^{-2}) and $\boldsymbol{\tau}_2$ (N·m^{-2}) are the total stress tensors in each phase (internal and external, respectively) at the interface, while $\boldsymbol{n}$ (dimensionless) is the normal of the interface. The term $\boldsymbol{f}_{st}$ (N·m^{-2}) corresponds to the force per unit area related to the surface tension, expressed in Eq. 5 [10].

$$\boldsymbol{f}_{st} = \sigma(\nabla_s \cdot \boldsymbol{n})\boldsymbol{n} - \nabla_s \sigma \quad (5)$$

where σ is the surface tension coefficient (N·m^{-1}) and ∇_s is the surface gradient operator, given by Eq. 6.[66]

$$\nabla_s = (\boldsymbol{I} - \boldsymbol{n} \cdot \boldsymbol{n}^T)\nabla \quad (6)$$

Two components (normal and tangential) can be written for the surface tension, according to Eqs. 7 and 8, respectively.[66]

$$(\boldsymbol{n} \cdot \boldsymbol{\tau}_1 - \boldsymbol{n} \cdot \boldsymbol{\tau_2}) \cdot \boldsymbol{n} = \sigma\kappa \cdot \boldsymbol{n} \quad (7)$$

$$(\boldsymbol{n} \cdot \boldsymbol{\tau}_1 - \boldsymbol{n} \cdot \boldsymbol{\tau_2}) \cdot \boldsymbol{t} = 0 \quad (8)$$

where κ (dimensionless) is the curvature of the interface. Moreover, continuity of the velocity field is considered at the interface, according to Eq. 9.[66]

$$\boldsymbol{u}_1 = \boldsymbol{u}_2 \quad (9)$$

where $\boldsymbol{u}_1$ (m·s^{-1}) and $\boldsymbol{u}_2$ (m·s^{-1}) are the velocity of the internal and external phase, respectively, at the interface.

Mass transfer and chemical reaction

The transport of species *i* in the micro-electrochemical reactor was modeled through the

steady-state convection-diffusion equation (Eq. 10), neglecting any bulk chemical reaction and considering Fickian diffusive flux.

$$(\boldsymbol{u}_c \cdot \nabla) c_i = \nabla \cdot (D_i \nabla c_i) \tag{10}$$

where $\boldsymbol{u}_c$ (m·s^{-1}) is the convective velocity, c_i (mol·m^{-3}) is the species *i* molar concentration and D_i (m^2·s^{-1}) is the species *i* mixture diffusivity (assumed as constant).

A finite flux was taken into account for species *i*, dependent on the local current density, at the anode's surface (Eq. 11), while the diffusive flux was assumed as negligible at the cathode's surface (Eq. 12).

$$-r_i'' = \frac{\nu_i i_{loc}}{nF} \tag{11}$$

$$-\boldsymbol{n} \cdot \boldsymbol{J}_i = 0 \tag{12}$$

where $-r_i''$ is the rate of species *i* consumption per unit of the anode's surface area (mol·m^{-2}·s^{-1}), ν_i is the stoichiometric coefficient (dimensionless), i_{loc} is the position-dependent current density (A·m^{-2}), n is the number of electrons involved in the chemical transformation (dimensionless), F is the Faraday constant (C·mol^{-1}) and $\boldsymbol{n}$ is the normal vector (dimensionless).

Periodicity was assigned at the unit cell's lateral boundaries, as described by Eqs. 13 and 14, i.e., both the species *i* concentration and normal convective flux are equal at these frontiers.

$$c_{i_{src}} = c_{i_{dst}} \tag{13}$$

$$-\boldsymbol{n}_{src} \cdot (\boldsymbol{J}_i + \boldsymbol{u} c_i)_{src} = \boldsymbol{n}_{dst} \cdot (\boldsymbol{J}_i + \boldsymbol{u} c_i)_{dst} \tag{14}$$

where $c_{i_{src}}$ and $c_{i_{dst}}$ are the species *i* concentration (mol·m^{-3}) at the source and destination boundaries, respectively; $\boldsymbol{n}_{src}$ and $\boldsymbol{n}_{dst}$ (dimensionless) are the normal vectors at the source and destination boundaries, respectively. The source and destination boundaries for the species transport model are equivalent to the inlet and outlet boundaries, respectively, of

the fluid flow model.

Moreover, the concentration of species *i* was imposed as the saturation concentration at the fluid-fluid interface, according to Eq. 15.

$$c_i = c_{i,int} = c_{i,sat} \tag{15}$$

where $c_{i,sat}$ is the species *i*'s saturation concentration (mol·m^{-3}).

Electrochemistry

The unit cell's electrochemistry was solved through a steady-state secondary current distribution approach, accounting for the concentration gradient and electrode kinetics. The electrolyte (phases Ω_1 and Ω_2) was assumed to conduct current according to Ohm's law (Eqs. 16 and 17).

$$\boldsymbol{i}_l = -\sigma_l \nabla \phi_l \tag{16}$$

$$\nabla \cdot \boldsymbol{i}_l = 0 \tag{17}$$

where $\boldsymbol{i}_l$ (A·m^{-2}) is the current density vector, σ_l (S·m^{-1}) is the electrical conductivity and ϕ_l (V) is the electrolyte potential. The conductivity of each phase (σ_{l,Ω_1} and σ_{l,Ω_2}) was constant. However, the values attributed to σ_{l,Ω_1} and σ_{l,Ω_2} were systematically varied in this study.

Null electric flux was assigned to the unit cell's lateral boundaries (Eq. 18), ensuring periodicity.

$$-\boldsymbol{n} \cdot \boldsymbol{i}_l = 0 \tag{18}$$

where $\boldsymbol{n}$ (dimensionless) is the normal vector.

On the other hand, the electric flux assumed finite values at the electrodes (Eq. 19), which in a generic case can be expressed as the sum of the local current densities from the m

chemical reactions occurring at those boundaries (Eq. 20).

$$\boldsymbol{n} \cdot \boldsymbol{i}_l = i_{total} \tag{19}$$

$$i_{total} = \sum_m i_{loc,m} = i_{loc} \tag{20}$$

where i_{total} (A·m^{-2}) is the total current density arising from the m chemical reactions occurring at the electrode's surface. In this study, $m = 1$ and i_{total} is equal to the position-dependent current density i_{loc} (A·m^{-2}).

In particular, concentration-dependent kinetics was prescribed at the anode (Eq. 21) to account for the current density at that surface, while linearized Butler-Volmer kinetics was assumed at the cathode (Eq. 22).

$$i_{loc} = i_0 \left[c_R exp\left(\frac{\alpha_a F \eta}{RT}\right) - c_O exp\left(\frac{\alpha_c F \eta}{RT}\right) \right] \tag{21}$$

$$i_{loc} = i_0 \left[\frac{(\alpha_a + \alpha_c)F}{RT} \right] \eta \tag{22}$$

where i_{loc} (A·m^{-2}) is the local current density, F (C·mol^{-1}) is the Faraday constant, i_0 (A·m^2) is the exchange current density, c_R and c_O (dimensionless) are the concentration of reduced and oxidized species, respectively, α_a and α_c (dimensionless) are the anodic and cathodic transfer coefficients, respectively, R (J·mol^{-1}·K^{-1}) is the universal gas constant, T (K) is the temperature and η (V) is the overpotential.

The overpotential η was calculated according to Eq. 23, where ϕ_s (V) and ϕ_l (V) are the electrode and electrolyte potential, respectively, and E_{eq} (V) is the equilibrium potential. Finally, a comprehensive potential balance was carried in the system, accounting for the activation (η_a and η_c, at the anode and the cathode, respectively), the ohmic (η_{ohm}) and the concentration (η_{conc}) overpotentials, according to Eq. 24.

$$\eta = \phi_s - \phi_l - E_{eq} \tag{23}$$

$$E_{cell} = E_{eq} + \eta_a + \eta_c + \eta_{ohm} + \eta_{conc} \quad (24)$$

Computational domain and solution strategy

We started the simulations by solving the fluid dynamics in the 2D unit cell. A UC with height $H = 250\,\mu m$ and length $4H$ was taken as reference. The ratio $\gamma = \Omega_1/\Omega_2$ was initially fixed in 0.5. An arbitrary shape for the secondary phase (Ω_2) was considered. Given the boundary conditions imposed, a time-dependent solution of the fluid flow equations was performed until steady-state was reached, i.e., when the interface velocity was virtually zero. An iterative procedure was adopted to find the wall velocity (U_w) resulting in steady-state conditions, i.e., stable secondary phase morphology with negligible interface motion positioned at the center of the UC, for a given set of boundary conditions. Three velocities were considered though a multiplier β = 1 – 3 (β = 3 corresponding to the velocity leading to the residence time of 5 min – typical in liquid-liquid electroorganic transformations in microchannels; $\beta_2 = \beta_3/2$ and $\beta_1 = \beta_3/3$). The surface tension coefficient was defined as 1 mN·m^{-1} in all simulations. Surface tension coefficients for aqueous-organic pairs typically vary in the range of ~1 mN/m to ~50 mN/m.[81] The external phase consists of CH_3CN, with density of 786 kg·m^{-3} and dynamic viscosity of 0.341 mPa·s, while the internal phase is water, with density of 1000 kg·m^{-3} and dynamic viscosity of 1 mPa·s.

Validation of the fluid flow model

Based on the same approach, different configurations were tested varying the two-phase velocity in the UC (U_{TP}), the UC length keeping γ constant (elongated secondary phase), the UC length with variable γ and the UC height H.

The same procedure was also applied to verify the fluid flow model, taking the thin film formed between the interface and the walls (external phase, Ω_2, film thickness), the droplet (internal phase, Ω_1) velocity and the pressure drop per droplet (internal phase, Ω_1) as reference. The numerical result for the external phase film thickness was compared with the prediction from the correlations developed or modified by Bretherton[82], Aussillous and Quéré[83], Han, Shikazono and Kasagi[84] and Eain, Egan and Punch[85] according to Eqs. (25) to

(28), respectively.

$$\frac{\delta}{D} = \frac{1}{2} \cdot 0.643 \cdot (3 \cdot Ca_D)^{2/3} \tag{25}$$

$$\frac{\delta}{D} = \frac{1}{2} \cdot \frac{0.643 \cdot (3 \cdot Ca_D)^{2/3}}{1 + 2.5 \cdot 0.643 \cdot (3 \cdot Ca_D)^{2/3}} \tag{26}$$

$$\frac{\delta}{H} = \frac{0.670 \cdot Ca_D^{2/3}}{1 + 3.13 \cdot Ca_D^{2/3} + 0.504 \cdot Ca_D^{0.672} \cdot Re_D^{0.589} - 0.352 \cdot We_D^{0.0629}} \tag{27}$$

$$\frac{\delta}{D} = \frac{1}{2} \cdot \frac{0.643 \cdot (3 \cdot Ca)^{2/3}}{1 + 1.6 \cdot 0.643 \cdot (3 \cdot Ca)^{2/3}} \tag{28}$$

where δ (m) is the thin film thickness, D (m) is the channel's diameter, H (m) is the channel's height, Ca_D (dimensionless) is the capillary number based on the dispersed phase velocity ($Ca_D = \mu_{ext} U_D / \sigma$; μ_{ext} consisting the dynamic viscosity of the external phase) and Ca is the capillary number based on the average two-phase velocity ($Ca = \mu_{ext} U_{TP} / \sigma$).

The droplet velocity was calculated as a function of the average two-phase velocity, the film thickness (predicted by a correlation) and the channel's characteristic length according to Eq. (29).[86]

$$\frac{U_D}{U_{TP}} = \left(1 - 2 \cdot \frac{\delta}{D}\right)^{-2} \tag{29}$$

Moreover, the pressure drop per droplet was estimated using the correlations of Ratulowski and Chang[87] and Langewisch and Buongiorno[88], according to Eqs. (30) and (31), respectively.

$$\frac{\Delta P_D}{\sigma / R} = 4.52 \cdot (3 \cdot Ca_D)^{2/3} - 12.6 \cdot Ca_D^{0.95} \tag{30}$$

$$\frac{\Delta P_D}{\sigma / R} = \begin{cases} 3.96 \cdot Ca_D^{0.58}, & Ca_D < 0.187, Re_D < 5 \\ 8 \cdot Ca_D, & Ca_D \geq 0.187 \end{cases} \tag{31}$$

Calculation of the species transport and the electrochemistry

The next step consisted of simulating the coupled species transport and electrochemistry with a steady-state solver. A specific concentration of species *i* was considered in the Ω_1 subdomain (internal phase) and at the interface, while null concentration was specified in the subdomain Ω_2 (external phase). The species *i* dissolved in the subdomain Ω_2 reacted at the anode's surface following concentration-dependent kinetics. Periodicity was ensured, as indicated before.

A half-cell approach was adopted, considering a varying positive voltage at the anode ($+3$ V to $+4$ V in intervals of 0.1 V) while keeping 0 V at the cathode. E_{eq} was specified as 0 V and $+2.9$ V at the cathode and the anode, respectively. Moreover, the exchange current density was defined as $i_0 = 1.0$ A·m^{-2} at the anode, while $i_0 = 10$ A·m^{-2} was considered at the cathode.

The concentration of the species *i* transferred from the phase Ω_1 to phase Ω_2, the electrical conductivity ratio $\theta = \sigma_1/\sigma_2$ and the diffusivity of species *i* were systematically varied in the simulations:

- $c_{i,\Omega_1} = c_{i,int}$ assumed the values 500 mol·m^{-3}, 5 mol·m^{-3}, 0.5 mol·m^{-3}, and 0.05 mol·m^{-3}.
- θ was defined as 2 (500 μS·cm^{-1}/250 μS·cm^{-1}), 50 (500 μS·cm^{-1}/10 μS·cm^{-1}), 0.5 (250 μS·cm^{-1}/500 μS·cm^{-1}) and ~ 0 (10^{-6} μS·cm^{-1}/250 μS·cm^{-1}).
- D_i was equal to 10^{-9} m^2·s^{-1} (reference), 10^{-8} m^2·s^{-1} and 10^{-10} m^2·s^{-1}.

CFD code and numerical details

The mathematical model was solved with the finite element method-based software COMSOL® Multiphysics (Burlington, MA), using the laminar flow, secondary current distribution and transport of diluted species modules. A mesh independence study was carried out to determine the optimal refinement level (i.e., capturing the intrinsic phenomena with an adequate computational cost). The optimal mesh refinement level consisted of ~2.6×10^5 elements. The fluid flow (time-dependent) and the coupled mass transfer and

electrochemistry (steady-state) were solved in two separate steps with direct solvers (MUMPS and PARDISO, respectively). The BDF algorithm was used for the variable time-stepping when solving the fluid dynamics.

7.4 Fluid dynamics in the electrochemical microreactor

Figure 7.3A presents the Taylor recirculation obtained through the CFD simulations in the 2D unit cell. The toroidal recirculation pattern obtained herein is consistent with previous works reported in the literature.[58,63,89,90]

In fact, Taylor recirculation plays a significant role in segmented flow in microchannels, contributing to intensifying the mixing.[91] The reliability of the fluid dynamics model was tested in the 2D rectangular channel taking the external phase (Ω_2) film thickness, the droplet (internal phase, Ω_1) velocity and the pressure drop per droplet (internal phase, Ω_1) as reference. For the given set of boundary conditions specified, the wall velocity was iteratively varied until a steady-state was reached with stagnant internal phase (Ω_1) positioned at the UC's center (considering $\gamma = 0.5$ and $L_{UC} = 4H_{UC}$). Under these conditions, the thin film thickness was measured (average value in the uniform liquid film zone) and compared to the correlations expressed by Eqs. (25) to (28). Figure 7.3B presents the external phase thin film thickness obtained numerically (CFD solution) and through the correlations of Bretherton [82], Aussillous and Quéré[83], Han, Shikazono and Kasagi[84] and Eain, Egan and Punch[85]. Good agreement was observed between the CFD results and all the correlations tested. The correlations from Aussillous and Queré, Han, Shikazono and Ksagi (HSK) and Eain, Egan and Punch (EEP) tended to underpredict the film thickness as the capillary number increased, while Bretherton's correlation resulted in a slight overprediction of δ for the higher capillary number evaluated.

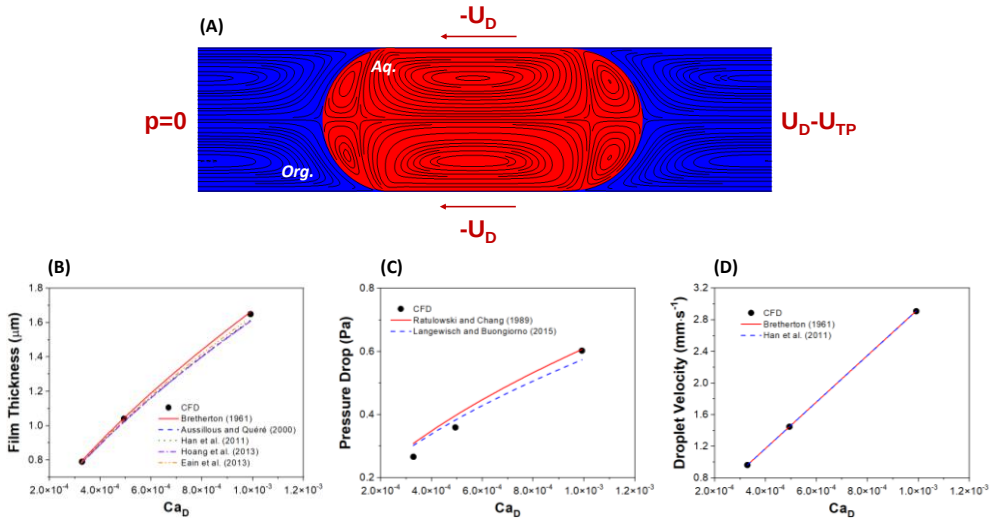

Figure 7.3 (A) Taylor flow in the unit cell. (B) Film thickness as a function of the capillary number. (C) Pressure drop per droplet as a function of the capillary number. (D) Droplet velocity as a function of the capillary number.

A critical capillary number for the transition from viscous-capillary to viscous-inertial regime can be estimated as $\mathbf{Ca^{*}\sim(\mu^{2}/\rho R\sigma)^{3/4}}$.[83,85] For the conditions evaluated in this work, $\mathbf{Ca^{*}\sim 2.5}$. Therefore, a viscous-capillary regime can be considered for all scenarios studied herein.

The theoretical expression proposed by Bretherton[82] ($\mathbf{10^{-4} < Ca_b < 10^{-2}}$, inviscid gas bubbles, $\boldsymbol{\delta \ll R}$) and the semi-empirical correlation presented by Aussillous and Quéré[83] ($\mathbf{Ca_b < 1.4}$) were obtained for gas-liquid Taylor flow in circular channels. The model from Aussillous and Queré captures the capillary's confinement effect imposing a limit to the film thickness for large $\mathbf{Ca_b}$, but reduces to Bretherton's predictions for low $\mathbf{Ca_b}$. The correlations proposed by Bretherton and Aussillous and Quéré fail to capture inertial effects on the film thickness. The correlation proposed by Eain, Egan and Punch[85] consists in a modification of the empirical coefficient in the expression from Aussillous and Quéré and considers liquid-liquid Taylor flow in circular channels ($\mathbf{Ca < 0.14}$). The correlation of Han, Shikazono and Kasagi[84] is applicable for gas-liquid Taylor flow in between two parallel plates (considering $\mathbf{0 < Ca_b \lesssim 0.4}$ and $\mathbf{Re < 2 \times 10^{3}}$). Thus, it is suitable for the

2D cases evaluated in this work. Moreover, it accounts for the inertial effects (inertial thinning at low $\mathbf{Re}$ and inertial thickening at high $\mathbf{Re}$).[88]

Therefore, given the low $\mathbf{Ca_b}$ and $\mathbf{Re}$ for the cases evaluated in this study, the film thickness obtained numerically is in good agreement with all correlations tested. Also, the low viscosity ratio for the internal/external phases (0.341) minimizes the effect of the droplet viscosity on the film thickness, as observed in previous works,[92-95] so that the predictions from the Bretherton's correlation are in agreement with the CFD results.

It is also interesting to note, from Fig. 7.3C, that a good agreement was obtained when comparing the pressure drop per droplet (internal phase, $\mathbf{\Omega_1}$) and the prediction from the expressions proposed by Ratulowski and Chang[87] ($\mathbf{Ca_b < 10^{-1}}$) and Langewisch and Buongiorno[88] ($\mathbf{Ca_b < 0.187}$ and $\mathbf{Re < 5}$). Finally, Fig. 7.3D shows that an excellent agreement was observed when comparing the droplet velocity obtained numerically (based on the iterative approach described earlier) and that predicted by Eq. (29) taking the film thickness predicted by the correlations of Bretherton[82] and Han, Shikazono and Kasagi[84] as reference.

It is important to highlight that different surface tension coefficients (taken as 1 $mN \cdot m^{-1}$ as a reference in this study) would essentially result in different thin film thicknesses.

In a previous study,[41] we have simulated gas-liquid Taylor flow in microchannel electrochemical reactors in steady-state, considering that the shear rate at the interface is negligible. Therefore, the slip boundary condition can be successfully applied to the interface. Since in liquid-liquid flow this assumption is not valid, the model must account for the shear rate at the interface. Therefore, a proper boundary condition should be implemented at the interface, allowing for a steady-state solution similar to what we did, or a multiphase model can be solved, which is the case of the moving mesh ALE approach

used herein. Robust results could also be obtained with traditional multiphase models, such as level-set, phase field, etc.

7.5 Liquid-liquid micro-flow electrochemistry

Polarization plots for the standard UC

Figure 7.4 presents the polarization plot (average current density measured at the anode varying the potential applied to the electrochemical cell in the range +3 V to +4 V in intervals of + 0.1 V) for the standard UC, considering different concentrations ($c_{i,sat}$ = 500 mol·m^{-3}, 5 mol·m^{-3}, 0.5 mol·m^{-3} and 0.05 mol·m^{-3}), diffusivities (D_i = 10^{-8} m^2·s^{-1}, 10^{-9} m^2·s^{-1} and 10^{-10} m^2·s^{-1}) and velocities (β = 1 – 3), but keeping the internal:external phase electrical conductivity ratio as 2 (500 μS·cm^{-1} and 250 μS·cm^{-1} for the internal and external phase, respectively). Each row indicates a different diffusivity (10^{-8} m^2·s^{-1} → 10^{-10} m^2·s^{-1}), while each column represents a different velocity for a variable-length reactor (β = 1 → 3).

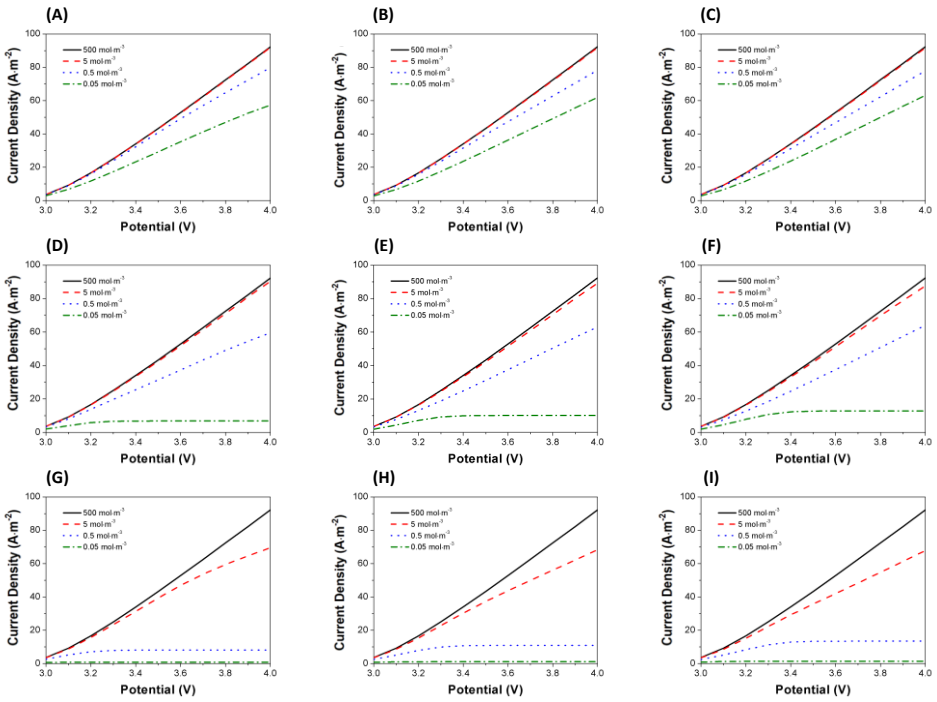

Figure 7.4 Polarization plot. Each column represents a given velocity (β = 3 → 1), while each row represents a diffusivity ($D_i = 10^{-8}$ m^2·s^{-1}, $D_i = 10^{-9}$ m^2·s^{-1} and $D_i = 10^{-10}$ m^2·s^{-1}, respectively). (A) β = 3, $D_i = 10^{-8}$ m^2·s^{-1}. (B) β = 2, $D_i = 10^{-8}$ m^2·s^{-1}. (C) β = 1, $D_i = 10^{-8}$ m^2·s^{-1}. (D) β = 3, $D_i = 10^{-9}$ m^2·s^{-1}. (E) β = 2, $D_i = 10^{-9}$ m^2·s^{-1}. (F) β = 1, $D_i = 10^{-9}$ m^2·s^{-1}. (G) β = 3, $D_i = 10^{-10}$ m^2·s^{-1}. (H) β = 2, $D_i = 10^{-10}$ m^2·s^{-1}. (I) β = 1, $D_i = 10^{-10}$ m^2·s^{-1}.

Effect of $c_{i,sat}$, D_i and β on the performance of electrochemical microreactor

Overall, the diffusivity has a more significant effect on the reactor performance than the velocity. Concentrations higher than 500 mol·m^{-3} did not result in mass transfer limitations for any diffusivities or velocities tested. In fact, for 5 mol·m^{-3} the mass transfer limitations are negligible for all scenarios when considering $D_i = 10^{-8}$ m^2·s^{-1}. However, for $c_{i,sat} <$ 5 mol·m^{-3} significant mass transfer limitations can be observed for all velocities considered.

When the diffusivity $D_i = 10^{-9}$ m^2·s^{-1} is considered, mass transfer limitations have a weak but noticeable effect for 5 mol·m^{-3}. However, the higher the velocity, the lower these limitations, which is aligned with the expected behavior. A limiting current density can be observed for the lower concentration tested (0.05 mol·m^{-3}), indicating severe mass transfer limitations.

For the diffusivity $D_i = 10^{-10}$ m^2·s^{-1}, significant mass transfer limitations are observed for 5 mol·m^{-3} and a limiting current density is noticed even for 0.5 mol·m^{-3}.

Interestingly, lower velocities result in higher current densities saturation values (limiting current densities) for lower concentrations. As the velocity increases, the mixing effect due to the Taylor recirculation is more pronounced. It leads to a higher concentration gradient (dc_i/dH) close to the anode's surface at the midpoint of two consecutive droplets (considering the saturation concentration of 0.05 mol·m^{-3} of species *i* from the aqueous phase). At this point, a higher velocity results in a higher local species concentration at the anode's surface and a higher species flux towards the anode.

However, it shows that the concentration gradient (dc_i/dH) decreases as the velocity

increases in the region of the external phase liquid film. In particular, this profile was obtained at the center of the liquid film region. Also, note that in this plot the concentration is represented across the entire thickness of the external phase liquid film, i.e., in between the liquid-liquid interface and the electrode (anode). The extent of this region (y-axis range) is naturally dependent on the velocity, as discussed before. Thus, it reveals that the species flux to the anode decreases as the velocity increases. Moreover, the local concentration at the anode surface is lower for higher velocities. Overall, the average species mass flux to the anode increases as the velocity decreases, as illustrated previously.

Thus, the limiting current density obtained is higher for lower velocities than the higher velocities evaluated. Another important conclusion is that the higher mass flux in the UC occurs precisely at the dispersed phase region. Therefore, in systems where the electrical conductivity of the secondary phase is higher than that of the primary phase (e.g., in liquid-liquid processes operating with aqueous droplets in a continuous organic phase), there is an intensification of the reaction rate due to the presence of the dispersed phase.

From these observations, it is clear that it is relevant to operate electrochemical microreactors at high concentrations (>5 mol·m^{-3} for $D_i \geq 10^{-9}$ m^2·s^{-1}; 500 mol·m^{-3} for $D_i \sim 10^{-10}$ m^2·s^{-1}) since it maximizes the current/voltage relation. However, an optimization is required since excessively high concentrations (>500 mol·m^{-3}) will not result in any efficiency gain. Moreover, too high concentrations are challenging in microreactors due to solubility limits and thus clogging can occur when e.g., the product is less soluble than the starting materials.

Potential balance under different operational conditions

A complementary understanding of the effect of the different operational variables studied herein can be obtained from Figure 7.5, representing the relative importance of the ohmic (η_{ohm}), concentration (η_{conc}) and activation (at the anode, $\eta_{(+)}^{act}$, and the cathode, $\eta_{(-)}$) overpotentials, excluding the equilibrium potential, i.e., $\left[E_{cell}/\left(\sum_i \eta_i - E_{eq}\right)\right] \times 100$, on the cell potential, for $D_i = 10^{-9}$ m^2·s^{-1}.

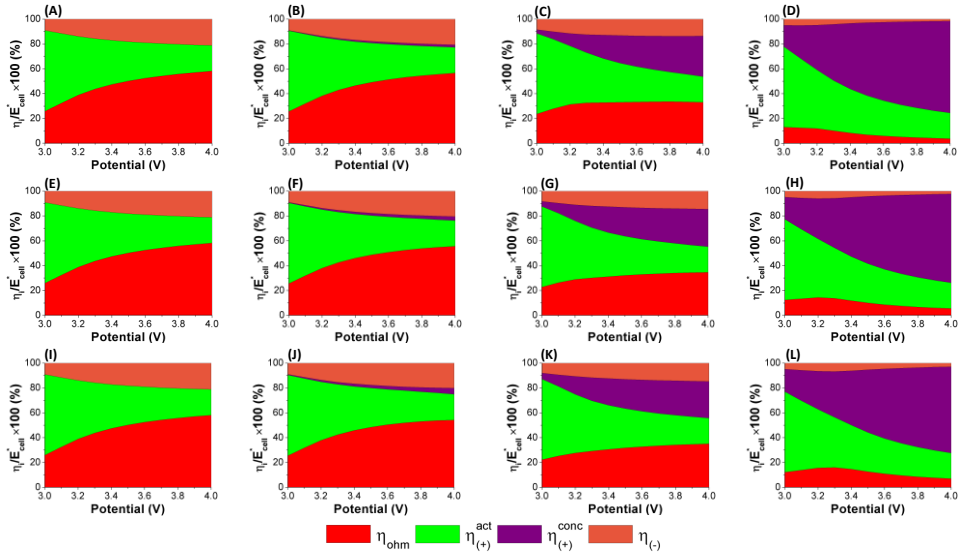

Figure 7.5 Potential distribution map. Each column represents a concentration (500 mol·m^{-3}, 5 mol·m^{-3}, 0.5 mol·m^{-3} and 0.05 mol·m^{-3}, respectively), while each row represents a given velocity ($\beta = 3 \rightarrow 1$). $D_i = 10^{-9}$ m^2·s^{-1} in all cases. (A) $\beta = 3$, $c_{i,sat} = 500$ mol·m^{-3}. (B) $\beta = 3$, $c_{i,sat} = 5$ mol·m^{-3}. (C) $\beta = 3$, $c_{i,sat} = 0.5$ mol·m^{-3}. (D) $\beta = 3$, $c_{i,sat} = 0.05$ mol·m^{-3}. (E) $\beta = 2$, $c_{i,sat} = 500$ mol·m^{-3}. (F) $\beta = 2$, $c_{i,sat} = 5$ mol·m^{-3}. (G) $\beta = 2$, $c_{i,sat} = 0.5$ mol·m^{-3}. (H) $\beta = 2$, $c_{i,sat} = 0.05$ mol·m^{-3}. (I) $\beta = 1$, $c_{i,sat} = 500$ mol·m^{-3}. (J) $\beta = 1$, $c_{i,sat} = 5$ mol·m^{-3}. (K) $\beta = 1$, $c_{i,sat} = 0.5$ mol·m^{-3}. (L) $\beta = 1$, $c_{i,sat} = 0.05$ mol·m^{-3}.

Effect of $c_{i,sat}$ and β, for a given $\sigma_{O_4}/\sigma_{O_2}$ and D_i

Clearly, for the higher concentration (500 mol·m^{-3}) there is a negligible effect of varying the velocity (decreasing $\beta = 3 \rightarrow 1$ for (A) → (I)). For 5 mol·m^{-3} there is a noticeable increase in the concentration overpotential as E_{cell} increases for lower velocities due to the lower mixing effect in this scenario. As the concentration is even lower (0.5 mol·m^{-3} and 0.05 mol·m^{-3}), the concentration overpotential (η_{conc}) becomes significant and represents the largest fraction of the cell potential when the applied potential is increased. However, it is interesting to note that for the lower concentration evaluated (0.05 mol·m^{-3}), the concentration overpotential decreased as the velocity decreased. On the other hand, the ohmic drop increased as the velocity decreased, which can be attributed to a reduced ion transport

between the electrodes at decreasing velocities. The activation overpotentials at the anode and the cathode were virtually independent of the velocity. The same behavior can be noticed for the concentration of 0.5 mol·m^{-3}.

Effect of $c_{i,sat}$ under different D_i, for a given β

Figure 7.6 shows the effect of the diffusivity of species *i* on the potential distribution in the electrochemical cell.

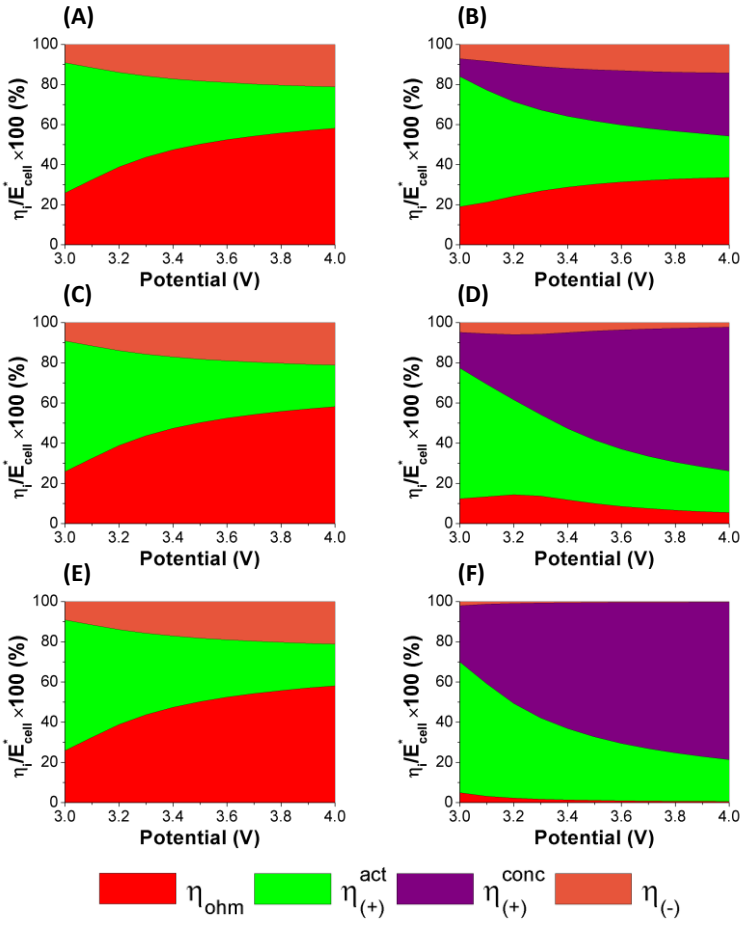

Figure 7.6 Potential distribution map. First column represents the concentration of 500 mol·m^{-3}, while the second column represents the concentration of 0.05 mol·m^{-3} (i.e., the limits

tested). Each row represents a different diffusivity ($D_i = 10^{-8}$ m^2·s^{-1}, $D_i = 10^{-9}$ m^2·s^{-1} and $D_i = 10^{-10}$ m^2·s^{-1}, respectively). (A) $D_i = 10^{-8}$ m^2·s^{-1}, $c_{i,sat}$ = 500 mol·m^{-3}. (B) $D_i = 10^{-8}$ m^2·s^{-1}, $c_{i,sat}$ = 0.05 mol·m^{-3}. (A) $D_i = 10^{-9}$ m^2·s^{-1}, $c_{i,sat}$ = 500 mol·m^{-3}. (C) $D_i = 10^{-9}$ m^2·s^{-1}, $c_{i,sat}$ = 0.05 mol·m^{-3}. (D) $D_i = 10^{-10}$ m^2·s^{-1}, $c_{i,sat}$ = 500 mol·m^{-3}. (E) $D_i = 10^{-10}$ m^2·s^{-1}, $c_{i,sat}$ = 0.05 mol·m^{-3}. β = 2 in all cases.

Clearly, for the higher concentration (500 mol·m^{-3}), the effect of varying the diffusivity on the potential distribution is insignificant within the considered E_{cell} range. However, this behavior changes as the concentration of species *i* in the dispersed phase decreases. In the limit scenario where the concentration is as low as 0.05 mol·m^{-3}, the potential distribution is indeed significantly dependent on the species *i* diffusivity. Notably, for the diffusivity $D_i = 10^{-10}$ m^2·s^{-1}, the applied E_{cell} is essentially distributed in concentration and anode activation overpotential. As the diffusivity increases, more relevant is the ohmic drop contribution and the cathode activation potential, accompanied by a remarkable decrease of the concentration overpotential. Interestingly, when taking the higher E_{cell} as a reference, the anode overpotential is virtually independent of the diffusivity.

Next, we set out to investigate the effect of the internal/external phase electrical conductivity ratio on the electrochemical performance. Figure 7.7 shows the observed behavior when the electrical conductivity ratio was changed to 50 (500 μS·cm^{-1}:10 μS·cm^{-1} for the internal and external phase, respectively), keeping the diffusivity constant ($D_i = 10^{-9}$ m^2·s^{-1}) and considering the velocity multiplier β = 2.

In this scenario, the maximum current density observed (for the concentration of 500 mol·m^{-3}) is 55.6% lower than in the case where $\sigma_{\Omega_1}/\sigma_{\Omega_2}$ = 2. Moreover, it is interesting to note that for $\sigma_{\Omega_1}/\sigma_{\Omega_2}$ = 50, the polarization curves overlap for the concentrations of 500 mol·m^{-3}, 5 mol·m^{-3} and 0.5 mol·m^{-3} (while for the reference case, $\sigma_{\Omega_1}/\sigma_{\Omega_2}$ = 2, a deviation from the maximum current-voltage relation is observed for 0.5 mol·m^{-3}). Different behavior is observed for the concentration of 0.05 mol·m^{-3}, leading to a limiting current density. Interestingly, the limiting current density for $\sigma_{\Omega_1}/\sigma_{\Omega_2}$ = 50 is virtually at the same level observed for $\sigma_{\Omega_1}/\sigma_{\Omega_2}$ = 2. The potential distribution plot reveals that the ohmic drop effect dominates for the concentrations of 500 mol·m^{-3}, 5 mol·m^{-3} and 0.5 mol·m^{-3}. A small

concentration overpotential is only observed when the concentration is reduced to 0.5 mol·m^{-3}. However, when the concentration is further reduced to 0.05 mol·m^{-3} the behavior is significantly different, and the concentration overpotential is the main contributor as the E_{cell} is increased (although for $E_{cell} \rightarrow 3$ V the ohmic drop is still the controlling mechanism).

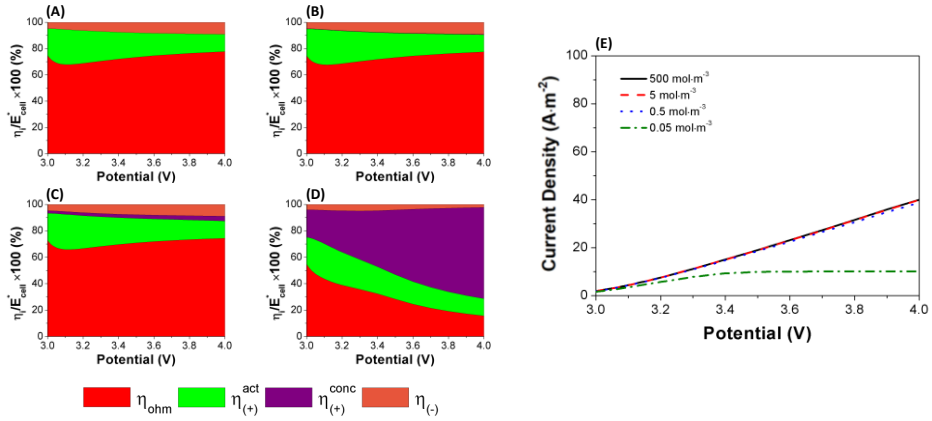

Figure 7.7 Potential distribution map and polarization plot for $\sigma_{\Omega_1}/\sigma_{\Omega_2}$ = 50 (500 μS·cm^{-1}:10 μS·cm^{-1} for the internal and external phase, respectively), keeping $D_i = 10^{-9}$ m^2·s^{-1} and β = 2 in all cases. (A) – (D) illustrates the potential distribution for the concentrations of 500 mol·m^{-3}, 5 mol·m^{-3}, 0.5 mol·m^{-3} and 0.05 mol·m^{-3}, respectively, while (E) illustrates the polarization plot for different concentrations considering the E_{cell} range of 3 V – 4 V.

Next, we have inverted the electrical conductivity ratio to $\sigma_{\Omega_1}/\sigma_{\Omega_2}$ = 0.5 (10 μS·cm^{-1}:500 μS·cm^{-1} for the internal and external phase, respectively), keeping the diffusivity $D_i = 10^{-9}$ m^2·s^{-1} and β = 2. The results are summarized in Figure 7.8.

In this scenario, the maximum current density for the concentration of 500 mol·m^{-3} is the same obtained in the reference case ($\sigma_{\Omega_1}/\sigma_{\Omega_2}$ = 2). However, as the concentration is reduced, lower current densities are obtained as E_{cell} is increased for $\sigma_{\Omega_1}/\sigma_{\Omega_2}$ = 0.5, but a limiting current density at the same level for $\sigma_{\Omega_1}/\sigma_{\Omega_2}$ = 2 is observed when the lower concentration (0.05 mol·m^{-3}) is taken into account (i.e., the limits are kept constant, although some deviation occurs within the analyzed range). In terms of potential distribution, it is interesting to note

that the ohmic drop dominates for the higher concentration (500 mol·m^{-3}) as E_{cell} increases. But, as $E_{cell} \rightarrow 3$ V, the anode activation overpotential becomes the dominating mechanism. Reducing the concentration has a sensible impact on the potential distribution from 5 mol·m^{-3}, as the concentration overpotential is significant for $E_{cell} \rightarrow 4$ V. As the concentration is reduced to the lowest level tested (0.05 mol·m^{-3}), the concentration overpotential dominates the potential distribution in the electrochemical cell as $E_{cell} \rightarrow 4$ V. However, for $E_{cell} \rightarrow 3$ V the anode activation overpotential is the main mechanism. It is also interesting to note that the ohmic drop represents a smaller portion of the potential map in all conditions tested for $\sigma_{\Omega_1}/\sigma_{\Omega_2}$ = 0.5 when compared to $\sigma_{\Omega_1}/\sigma_{\Omega_2}$ = 2 (reference case).

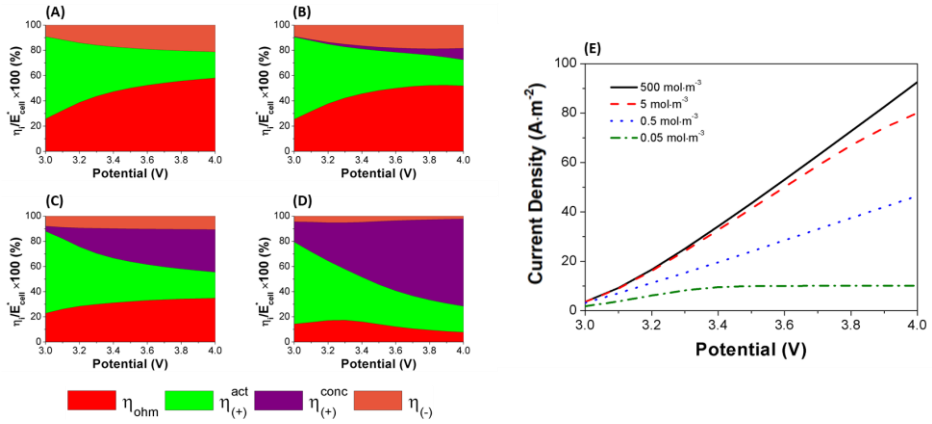

Figure 7.8 Potential distribution map and polarization plot for $\sigma_{\Omega_1}/\sigma_{\Omega_2}$ = 0.5 (10 μS·cm^{-1}:500 μS·cm^{-1} for the internal and external phase, respectively), keeping $D_i = 10^{-9}$ m^2·s^{-1} and β = 2 in all cases. (A) – (D) illustrates the potential distribution for the concentrations of 500 mol·m^{-3}, 5 mol·m^{-3}, 0.5 mol·m^{-3} and 0.05 mol·m^{-3}, respectively, while (E) illustrates the polarization plot for different concentrations considering the E_{cell} range of 3 V – 4 V.

Then, we investigated the scenario where $\sigma_{\Omega_1}/\sigma_{\Omega_2} \approx 10^{-9}$ (10^{-6} μS·cm^{-1}:500 μS·cm^{-1} for the internal and external phase, respectively), keeping the diffusivity $D_i = 10^{-9}$ m^2·s^{-1} and β = 2. This scenario corresponds to a limiting case where the electrical resistance in the internal phase tends to infinite. We have investigated it deeply in our previous study on the influence of gas-liquid segmented flow on the electrochemical performance.[32] Figure 7.9

summarizes the results obtained.

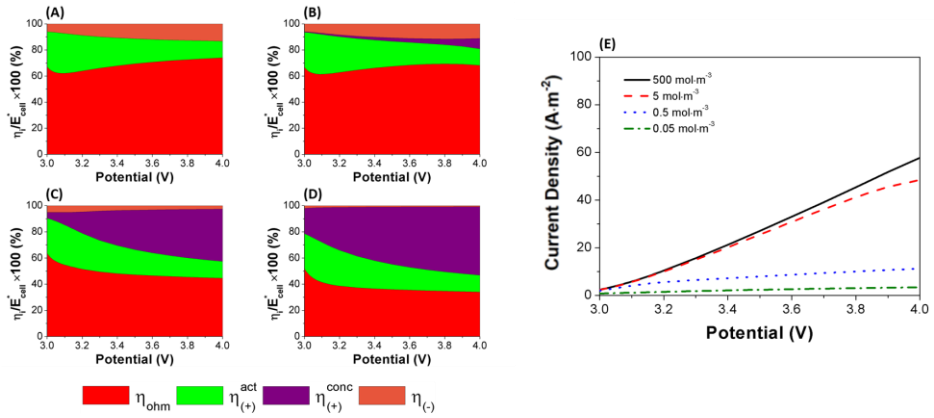

Figure 7.9 Potential distribution map and polarization plot for $\sigma_{\Omega_1}/\sigma_{\Omega_2} \approx 10^{-9}$ (10^{-6} μS·cm^{-1}:500 μS·cm^{-1} for the internal and external phase, respectively), keeping $D_i = 10^{-9}$ m^2·s^{-1} and β = 2 in all cases. (A) – (D) illustrates the potential distribution for the concentrations of 500 mol·m^{-3}, 5 mol·m^{-3}, 0.5 mol·m^{-3} and 0.05 mol·m^{-3}, respectively, while (E) illustrates the polarization plot for different concentrations considering the E_{cell} range of 3 V – 4 V.

Overall, lower current densities were observed for all concentrations (500 mol·m^{-3}, 5 mol·m^{-3}, 0.5 mol·m^{-3} and 0.05 mol·m^{-3}). A reduction of approximately 34% is noticed for the higher concentration at the higher potential (4 V) when compared to the reference case ($\sigma_{\Omega_1}/\sigma_{\Omega_2}$ = 2). Limiting current densities are observed for the concentrations of 0.5 mol·m^{-3} and 0.05 mol·m^{-3}. Interestingly, the plateau obtained for the concentration of 0.05 mol·m^{-3} is lower than the result obtained in the reference case. The reaction shuts down in the region of the internal phase. For the higher concentration tested (500 mol·m^{-3}), this scenario is even more noticeable. On the other hand, for the lower concentration (0.05 mol·m^{-3}), the species *i* flux is maximum at the edges of the internal phase.

Summary of the effect of $c_{i,sat}$ under different $\sigma_{\Omega_1}/\sigma_{\Omega_2}$

Figure 7.10 summarizes the conclusions extracted from the study of the effect of the electrical conductivity ratio $\sigma_{\Omega_1}/\sigma_{\Omega_2}$ on the performance of the electrochemical reactor, based on the

polarization plots. A higher $\sigma_{\Omega_2}/\sigma_{\Omega_1}$ leads to better performance. However, for optimal operation, σ_{Ω_2} must be tuned to significant levels, as lower values for this parameter are detrimental for the overall performance. While the reaction is intensified at the internal phase region when $\sigma_{\Omega_1} > \sigma_{\Omega_2}$, the reaction shuts down in this region when $\sigma_{\Omega_1}/\sigma_{\Omega_2} \rightarrow 0$, i.e., when the electrical resistance in the internal phase becomes almost infinite; this is a situation which is comparable to gas-liquid Taylor flow where no ion transport is observed in and around the gas bubble.

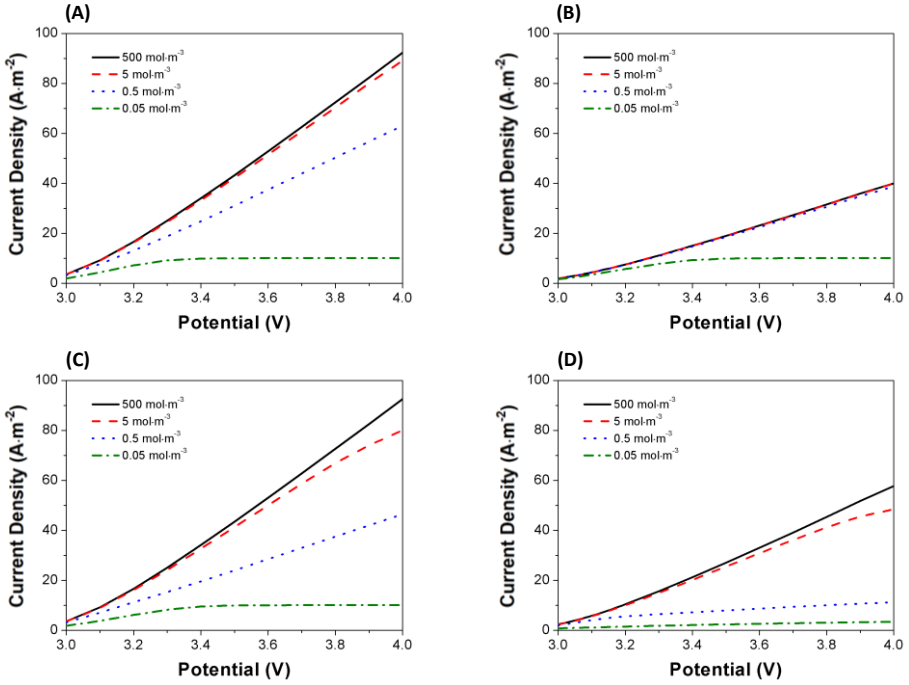

Figure 7.10 Polarization plot for different operating conditions. (A) $\sigma_{\Omega_1}/\sigma_{\Omega_2}$ = 2 (500 μS·cm^{-1}:250 μS·cm^{-1} for the internal and external phase, respectively). (B) $\sigma_{\Omega_1}/\sigma_{\Omega_2}$ = 50 (500 μS·cm^{-1}:10 μS·cm^{-1} for the internal and external phase, respectively). (C) $\sigma_{\Omega_1}/\sigma_{\Omega_2}$ = 0.5 (10 μS·cm^{-1}:500 μS·cm^{-1} for the internal and external phase, respectively). (D) $\sigma_{\Omega_1}/\sigma_{\Omega_2}$ ≈ 10^{-9} (10^{-6} μS·cm^{-1}:500 μS·cm^{-1} for the internal and external phase, respectively). $D_i = 10^{-9}$ m^2·s^{-1} and β = 2 in all cases.

Finally, we investigated the effect of different configurations for the UC, considering a

varying γ (volume fraction ratio of internal/external phase) first. As γ is reduced for the same set of operational conditions (diffusivity $D_i = 10^{-9}$ m^2·s^{-1}, $\beta = 2$ and $\sigma_{\Omega_1}/\sigma_{\Omega_2} = 2$) the reactor performance deteriorates. With lower γ, the current density is lower for a given E_{cell}. While for the higher concentration tested (500 mol·m^{-3}) the potential distribution is virtually independent of γ, this scenario is different when the concentration of 0.05 mol·m^{-3} is considered. In this case, as γ is reduced, the ohmic drop reduces and the concentration overpotential increases, becoming the dominating mechanism as $E_{cell} \rightarrow 4$ V. Therefore, it is preferable to operate the reactor with a higher frequency of dispersed phase to maximize its performance. Figure 7.11 illustrates this behavior.

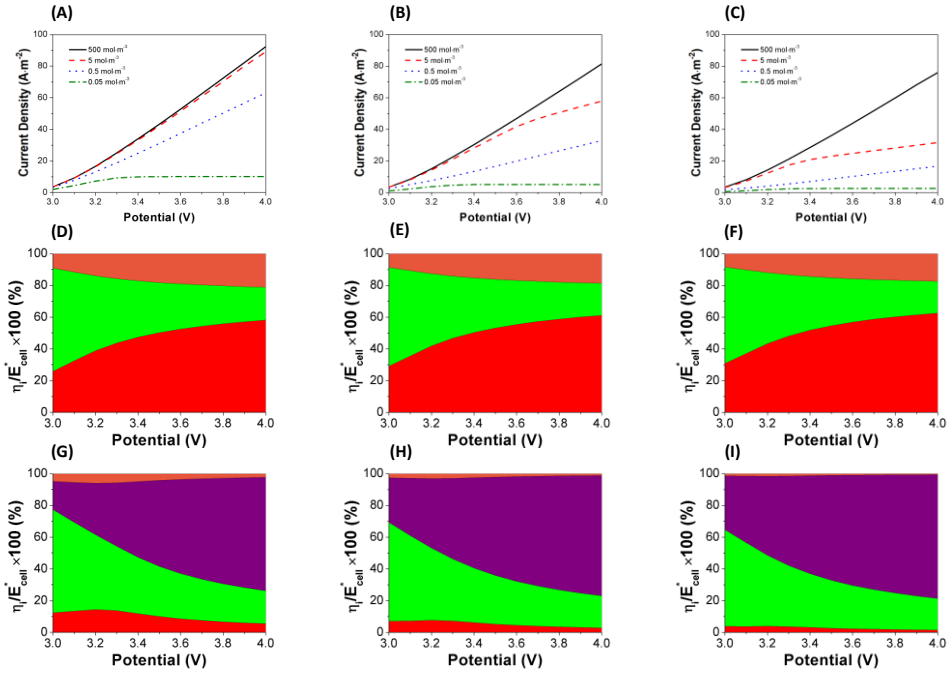

Figure 7.11 Polarization plot and potential distribution map as a function of the volume fraction (γ) of the internal phase and the concentration. Each column represents a different volume fraction ($\gamma = 0.5$, $\gamma = 0.25$ and $\gamma = 0.125$, respectively). Second row illustrates the behavior for the concentration of 500 mol·m^{-3}, while the third row represents the concentration of 0.05 mol·m^{-3} (i.e., the limits of analysis). $D_i = 10^{-9}$ m^2·s^{-1} and $\beta = 2$ in all cases.

Complementary studies about the effect of relevant variables

The effect of increasing the UC length while keeping the volume fraction of the internal phase (γ) constant (i.e., working with elongated internal phase), varying the inter-electrode gap (H) as well as the maps for the electrolyte potential, electrolyte current density and concentration for the system operating under different reaction conditions are presented and discussed in the Supplementary Information.

Figures 7.12 and 7.13 illustrate the electrolyte potential, electrolyte current density and concentration maps for the system operating under different reaction conditions. In Figure 7.12, one can notice that for $\sigma_{\Omega_1}/\sigma_{\Omega_2} = 2$, $D_i = 10^{-9}$ m^2·s^{-1} and $\beta = 2$, i.e., the standard case for a concentration of 500 mol·m^{-3}, it is clear to see the intensification of the reaction rate at the region of the internal phase, regardless of E_{cell}.

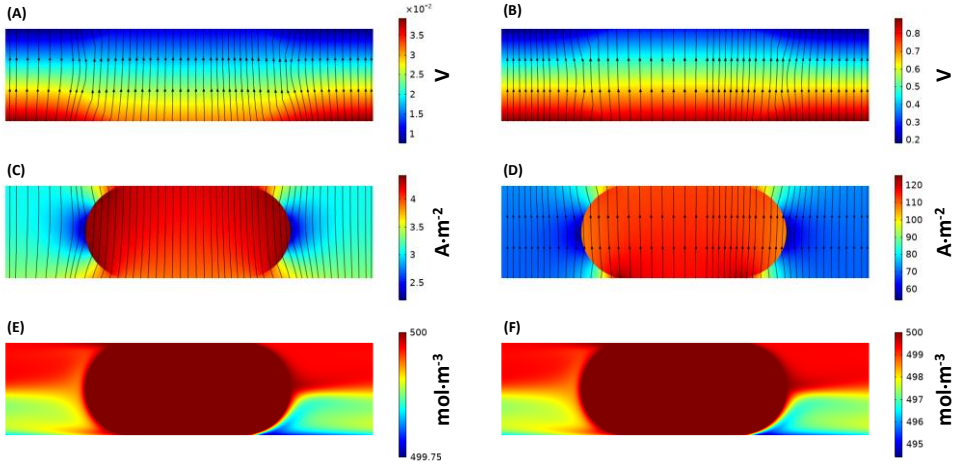

Figure 7.12 Contours of electrolyte potential, electrolyte current density and concentration as a function of the applied potential (E_{cell}), considering a concentration of 500 mol·m^{-3} in the internal phase. (A) Electrolyte potential for E_{cell} = 3 V. (B) Electrolyte potential for E_{cell} = 4 V. (C) Electrolyte current density for E_{cell} = 3 V. (D) Electrolyte current density for E_{cell} = 4 V. (E) Concentration for E_{cell} = 3 V. (F) Concentration for E_{cell} = 4 V. $D_i = 10^{-9}$ m^2·s^{-1}, β = 2 and $\sigma_{\Omega_1}/\sigma_{\Omega_2}$ = 2 in all cases.

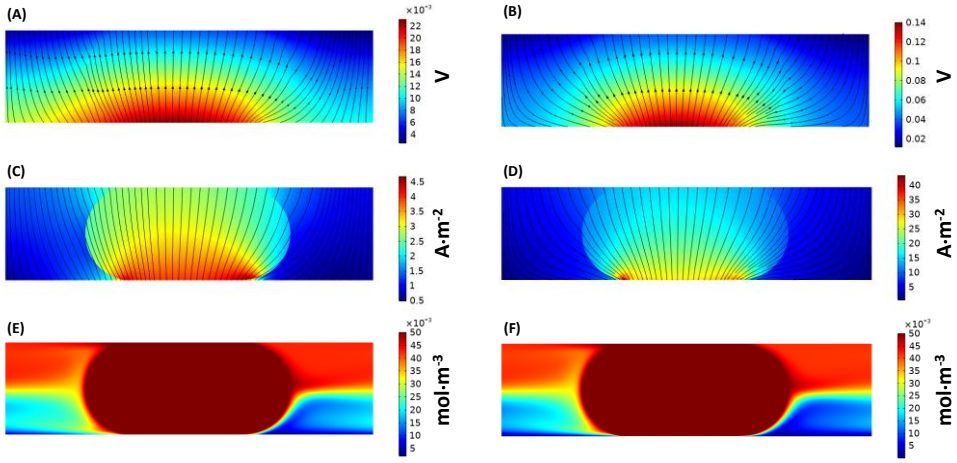

Figure 7.13 Contours of electrolyte potential, electrolyte current density and concentration as a function of the applied potential (E_{cell}), considering a concentration of 0.05 mol·m^{-3} in the internal phase. (A) Electrolyte potential for E_{cell} = 3 V. (B) Electrolyte potential for E_{cell} = 4 V. (C) Electrolyte current density for E_{cell} = 3 V. (D) Electrolyte current density for E_{cell} = 4 V. (E) Concentration for E_{cell} = 3 V. (F) Concentration for E_{cell} = 4 V. $D_i = 10^{-9}$ m^2·s^{-1}, β = 2 and $\sigma_{\Omega_1}/\sigma_{\Omega_2}$ = 2 in all cases.

It is also interesting to note that as the diffusivity decreases, the reactor tends to operate like a divided cell. Moreover, Figure 7.13 presents the behavior when the conditions from Figure 7.12 are kept except that the concentration is reduced to the lower limit (0.05 mol·m^{-3}). Clearly, in this scenario there is still an intensification of the reaction rate at the region of the internal phase, but the pattern observed for the electrolyte potential and the electrolyte current density is significantly different.

7.6 Conclusions

We have conducted a phenomenological investigation on the effect of different operational scenarios for liquid-liquid Taylor flow electrochemistry. We show that the selected variables (electrical conductivity ratio, mass diffusivity, velocity, concentration, cell potential, internal phase volume fraction, internal phase length and inter-electrode distance) have different impact levels on the reactor performance, with a strong interdependence.

Operating micro-flow electrochemical devices at high concentrations is beneficial in all scenarios evaluated. However, a large excess should be avoided as it does not result in a further improvement after a specific limit which should be optimized for each specific electrochemical transformation and reactor configuration. Moreover, the systems take advantage of higher diffusivities, although even in this case, limiting current densities can be noticed when operating at low concentrations.

In all cases, operating with an electrical conductivity ratio > 1 for internal:external phase is beneficial, which is commonly observed when working with aqueous droplets in a continuous organic phase. In general, the higher the ratio, the better the performance. However, care should be taken to keep the external phase electrical conductivity at sufficiently high levels to ensure the improved performance. The velocity impact is significant only under specific operating windows, and in some cases working at lower velocities is beneficial since higher limiting current densities are observed (and consequently, the reaction rate is improved).

The higher the applied potential, the better the performance in terms of current density (and consequently reaction rate) at a given set of operating conditions. Although, it should be noted that in some cases a limiting level is reached due to severe mass transfer limitations (null limiting reagent concentration at the working electrode surface). Interestingly, a diverse set of potential distribution fractions (considering ohmic, concentration and activation overpotentials) is observed as the cell potential is varied under the subspaces of independent variables.

The flow arrangement (internal phase volume fraction, droplet length and inter-electrode distance) also has a significant effect on the electrochemical performance, although the same limiting-performances can be observed in some scenarios.

Finally, we believe that the insights gained herein will be important to electrochemistry practitioners in both academia and industry to develop more efficient electrochemical micro-flow reactors and processes for liquid-liquid transformations.

References

[1] Mohan SV, Katakojwala R (2021). Curr Opin Green Sustain Chem 28:100434

[2] Yang F, Gu S (2021). Complex Intell Syst 7:1311-1325

[3] Van Gerven T, Stankiewicz A (2009). Ind Eng Chem Res 48:2465–2474

[4] Keil FJ (2018). Rev Chem Eng 34:135–200

[5] Becht S, Franke R, Geißelmann A, Hahn H (2009). Chem Eng Process Process Intensif 48:329–332

[6] Ponce-Ortega JM, Al-Thubaiti MM, El-Halwagi MM (2012). Chem Eng Process Process Intensif 53:63–75

[7] Rivas DF, Castro-Hernández E, Villanueva Perales AL, van der Meer W (2018). Chem Eng Process - Process Intensif 123:221–232

[8] Kim Y, Park LK, Yiacoumi S, Tsouris C (2017). Annu Rev Chem Biomol Eng 8:359–380

[9] Boffito DC, Fernandez Rivas D (2020). Can J Chem Eng 98:2489–2506

[10] Dautzenberg FM, Mukherjee M (2001). Chem Eng Sci 56:251–267

[11] Chaudhuri A, Kuijpers KPL, Hendrix R, Hacking J, Shivaprasad P, Emanuelsson EAC, Noel T, Schaaf J van der (2020). Chem Eng J 400:125875

[12] Dong Z, Wen Z, Zhao F, Kuhn S, Noël T (2021). Chem Eng Sci X :100097

[13] Balomenou SP, Tsiplakides D, Katsaounis A, Brosda S, Hammad A, Fóti G, Comninellis C, Thiemann-Handler S, Cramer B, Vayenas CG (2006). Solid State Ionics 177:2201–2204

[14] Wang C, Gu Y, Wu S, Yu H, Chen S, Su Y, Guo Y, Wang X, Chen H, Kang W, Quan X (2020). Environ Sci Technol 54:1920–1928

[15] Rabuni MF, Vatcharasuwan N, Li T, Li K (2020). J Power Sources 458:228026

[16] Hessel V (2009). Chem Eng Technol 32:1655–1681

[17] Hessel V, Kralisch D, Kockmann N, Noël T, Wang Q (2013). ChemSusChem 6:746–789

[18] Hammad A, Souentie S, Papaioannou EI, Balomenou S, Tsiplakides D, Figueroa JC, Cavalca C, Pereira CJ (2011). Appl Catal B Environ 103:336–342

[19] Balomenou S, Tsiplakides D, Katsaounis A, Thiemann-Handler S, Cramer B, Foti G, Comninellis C, Vayenas CG (2004). Appl Catal B Environ 52:181–196

[20] Chatzilias C, Martino E, Katsaounis A, Vayenas CG (2021). Appl Catal B Environ 284:119695

[21] Jacobs M, Kayahan E, Thomassen LCJ, Kuhn S, Leblebici ME (2020). J Adv Manuf

Process 2:e10047
[22] Tomašić V, Jović F (2006). Appl Catal A Gen 311:112–121
[23] Moulijn JA, Kapteijn F (2013). Curr Opin Chem Eng 2:346–353
[24] Su Y, Straathof NJW, Hessel V, Noël T (2014). Chem – A Eur J 20:10562–10589
[25] Sambiagio C, Noël T (2020). Trends Chem 2:92–106
[26] Noël T, Cao Y, Laudadio G (2019). Acc Chem Res 52:2858–2869
[27] Atobe M, Tateno H, Matsumura Y (2018). Chem Rev 118:4541–4572
[28] Obama B (2017). Science (80-) 355:126–129
[29] Armaroli N, Balzani V (2011). Energy Environ Sci 4:3193–3222
[30] Tanbouza N, Ollevier T, Lam K (2020). iScience 23
[31] Yan M, Kawamata Y, Baran PS (2017). Chem Rev 117:13230–13319
[32] Wiebe A, Gieshoff T, Möhle S, Rodrigo E, Zirbes M, Waldvogel SR (2018). Angew Chemie Int Ed 57:5594–5619
[33] Marken F, Wadhawan JD (2019). Acc Chem Res 52:3325–3338
[34] Tang S, Liu Y, Lei A (2018). Chem 4:27–45
[35] Reymond F, Fermín D, Lee HJ, Girault HH (2000). Electrochim Acta 45:2647–2662
[36] Scholz F (2006). Annu Reports Sect "C" (Physical Chem 102:43–70
[37] Vanýsek P (1995). Electrochim Acta 40:2841–2847
[38] Gupta R, Fletcher DF, Haynes BS (2010). J Comput Multiph Flows 2:1–31
[39] Haase S, Murzin DY, Salmi T (2016). Chem Eng Res Des 113:304–329
[40] Sobieszuk P, Aubin J, Pohorecki R (2012). Chem Eng Technol 35:1346–1358
[41] Cao Y, Soares C, Padoin N, Noël T (2021). Chem Eng J 406:126811
[42] Oliveira de Brito Lira J, Riella HG, Padoin N, Soares C (2021). J Environ Chem Eng 9:105068
[43] Lira JOB, Riella HG, Padoin N, Soares C (2020). Chem Eng Process - Process Intensif 154:107998
[44] de Oliveira GX, Lira JOB, Cambié D, Noël T, Riella HG, Padoin N, Soares C (2020). Chem Eng Res Des 153:626–634
[45] de O.B. Lira J, Padoin N, Vilar VJP, Soares C (2019). J Hazard Mater 372:145–153
[46] Padoin N, Souza AZ de, Ropelato K, Soares C (2016). Chem Eng Res Des 109:698–706
[47] Padoin N, Soares C (2017). Chem Eng J 310:381–388
[48] Padoin N, Dal'Toé ATO, Rangel LP, Ropelato K, Soares C (2014). Int J Heat Mass Transf

73:239–249

[49] Cambié D, Bottecchia C, Straathof NJW, Hessel V, Noël T (2016). Chem Rev 116:10276–10341

[50] Poe SL, Cummings MA, Haaf MP, McQuade DT (2006). Angew Chemie Int Ed 45:1544–1548

[51] Karim A, Bravo J, Gorm D, Conant T, Datye A (2005). Catal Today 110:86–91

[52] Sebastian Cabeza V, Kuhn S, Kulkarni AA, Jensen KF (2012). Langmuir 28:7007–7013

[53] Günther A, Jensen KF (2006). Lab Chip 6:1487–1503

[54] Gupta R, Leung SSY, Manica R, Fletcher DF, Haynes BS (2013). Chem Eng Sci 92:180–189

[55] Abdollahi A, Norris SE, Sharma RN (2020a). Int J Heat Mass Transf 156:119802

[56] Jovanović J, Zhou W, Rebrov E V, Nijhuis TA, Hessel V, Schouten JC (2011). Chem Eng Sci 66:42–54

[57] Desir P, Chen T-Y, Bracconi M, Saha B, Maestri M, Vlachos DG (2020). React Chem Eng 5:39–50

[58] Abdollahi A, Norris SE, Sharma RN (2020b). Appl Therm Eng 172:115123

[59] Dai Z, Guo Z, Fletcher DF, Haynes BS (2015). Chem Eng Sci 138:140–152

[60] Vivekanand SVB, Raju VRK (2018). Heat Transf Res 47:794–805

[61] Abdollahi A, Sharma RN, Vatani A (2017). Int Commun Heat Mass Transf 84:66–74

[62] Sarkar PS, Singh KK, Shenoy KT, Sinha A, Rao H, Ghosh SK (2012). Ind Eng Chem Res 51:5056–5066

[63] Yao C, Ma H, Zhao Q, Liu Y, Zhao Y, Chen G (2020). Chem Eng Sci 223:115734

[64] Dessimoz A-L, Cavin L, Renken A, Kiwi-Minsker L (2008). Chem Eng Sci 63:4035–4044

[65] Vansteene A, Jasmin J-P, Cote G, Mariet C (2018). Ind Eng Chem Res 57:11572–11582

[66] Girault HH. In: Bard AJ, Zoski CG (eds) Electroanalytical chemistry. CRC Press PP - Boca Raton, pp 1–104

[67] Liu B, Mirkin M V (2000). Electroanalysis 12:1433–1446

[68] Liu S, Li Q, Shao Y (2011). Chem Soc Rev 40:2236–2253

[69] Kivlehan F, Lanyon YH, Arrigan DWM (2008). Langmuir 24:9876–9882

[70] Laudadio G, Bartolomeu A de A, Verwijlen LMHM, Cao Y, de Oliveira KT, Noël T (2019a). J Am Chem Soc 141:11832–11836

[71] Cao Y, Adriaenssens B, de A. Bartolomeu A, Laudadio G, de Oliveira KT, Noël T (2020). J Flow Chem 10:191–197

[72] Laudadio G, de Smet W, Struik L, Cao Y, Noël T (2018). J Flow Chem 8:157–165

[73] Laudadio G, Barmpoutsis E, Schotten C, Struik L, Govaerts S, Browne DL, Noël T (2019b). J Am Chem Soc 141:5664–5668

[74] Dong J, Krasnova L, Finn MG, Sharpless KB (2014). Angew Chemie Int Ed 53:9430–9448

[75] Abdul Fattah T, Saeed A, Albericio F (2018). J Fluor Chem 213:87–112

[76] Ni D, Hong FJ, Cheng P, Chen G (2017). Int Commun Heat Mass Transf 88:37–47

[77] Yang K, Hong F, Cheng P (2014). Int J Heat Mass Transf 70:409–420

[78] Jia H, Xiao X, Kang Y (2019). Int J Heat Mass Transf 137:545–557

[79] Donea J, Huerta A, Ponthot J-P, Rodríguez-Ferran A (2017). Encycl. Comput. Mech. Second Ed. 1–23

[80] Bretherton FP (1961). J Fluid Mech 10:166–188

[81] Aussillous P, Quéré D (2000). Phys Fluids 12:2367–2371

[82] Han Y, Shikazono N, Kasagi N (2011). Int J Multiph Flow 37:36–45

[83] Andersson MP, Bennetzen M V, Klamt A, Stipp SLS (2014). J Chem Theory Comput 10:3401–3408

[84] Mac Giolla Eain M, Egan V, Punch J (2013). Int J Heat Fluid Flow 44:515–523

[85] Hoang DA, van Steijn V, Portela LM, Kreutzer MT, Kleijn CR (2013). Comput Fluids 86:28–36

[86] Ratulowski J, Chang H-C (1990). J Fluid Mech 210:303–328

[87] Langewisch DR, Buongiorno J (2015). Int J Heat Fluid Flow 54:250–257

[88] Peng Z, Ge L, Moreno-Atanasio R, Evans G, Moghtaderi B, Doroodchi E (2020). Chem Eng J 396:124738

[89] Ge L, Peng Z, Moreno-Atanasio R, Doroodchi E, Evans GM (2020). Ind Eng Chem Res 59:7965–7981

[90] Ahmed-Omer B, Brandt JC, Wirth T (2007). Org Biomol Chem 5:733–740

[91] Martinez MJ, Udell KS (1990). J Fluid Mech 210:565–591

[92] LAC E, SHERWOOD JD (2009). J Fluid Mech 640:27–54

[93] Jovanović J, Zhou W, Rebrov E V, Nijhuis TA, Hessel V, Schouten JC (2011). Chem Eng Sci 66:42–54

[94] Gupta R, Leung SSY, Manica R, Fletcher DF, Haynes BS (2013). Chem Eng Sci 92:180–189

Outlook

In a nutshell, this dissertation covers the organic electrochemical synthesis in flow, together with the fundamental principles research on multiphase flow regime, as a way to dig deeper into the advantages behind the use of continuous-flow microreactors for carrying out synthetic organic electrochemistry and the potential of biobased platform feedstock. The chapters were introduced in chronological order, from the design and verification of electrochemical microflow reactor, the electrochemical conversion of furfural (a typical biobased chemical) into valuable chemicals in flow, the transformation and acceleration of a liquid-liquid biphasic electrochemical reactions into microflow reactor, and the numerical analysis of gas-liquid Taylor flow regime at last. It was our aim to compile organic chemistry and chemical engineering, which hopefully will serve as a useful reference and starting point for researchers looking to translate their electrochemistry to flow. Fundamental understanding about multiphase flow regime in flow electrochemistry will allow practitioners to get the maximum out of the technology. While significant progress has been made throughout the past decade, moving forward is not without a challenge. Through use of continuous-flow microreactors, new and uncharted chemical space can be discovered. Hence, the community should focus more on examples that provide decisive advantages over their batch counterparts. In our opinion, multiphase electrochemistry remains largely underrepresented to date. Arguably, clogging of the channels continues to be the Achilles heel of microreactor technology, and effective solutions need to be found to accommodate both solid reagents and products in flow. Solving these issues undoubtedly requires collaborative efforts between chemical engineers and chemists from both academia and industry. We are confident that progress on these aspects will increase the utility of flow reactor technology and will push the boundaries of synthetic organic electrochemistry.

Publications

1. Cao, Y.; Knijff, J.; Delparish, A.; Neira d'Angelo, M. F. and Noel, T. A Divergent Paired Electrochemical Process for the Conversion of Furfural Using a Divided-Cell Flow Microreactor. *ChemSusChem* **2021**, 14 (2), 590–594.

2. Cao, Y.; Soares, C.; Padoin, N. and Noël, T. Gas Bubbles Have Controversial Effects on Taylor Flow Electrochemistry. *Chemical Engineering Journal* **2021**, 406, 126811.

3. Cao, Y.; Adriaenssens, B.; de A. Bartolomeu, A.; Laudadio, G.; de Oliveira, K. T. and Noël, T. Accelerating Sulfonyl Fluoride Synthesis through Electrochemical Oxidative Coupling of Thiols and Potassium Fluoride in Flow. *Journal of Flow Chemistry* **2020**, 10, 191-197.

4. Cao, Y. and Noël, T. Efficient Electrocatalytic Reduction of Furfural to Furfuryl Alcohol in a Microchannel Flow Reactor. *Organic Process Research & Development* **2019**, 23 (3), 403-408.

5. Noël, T.; Cao, Y. and Laudadio, G. The Fundamentals Behind the Use of Flow Reactors in Electrochemistry. *Accounts of Chemical Research* **2019**, 52 (10), 2858-2869.

6. Laudadio, G.; Bartolomeu, A. de A.; Verwijlen, L. M. H. M.; Cao, Y.; de Oliveira, K. T. and Noël, T. Sulfonyl Fluoride Synthesis through Electrochemical Oxidative Coupling of Thiols and Potassium Fluoride. *Journal of the American Chemical Society* **2019**, 141 (30), 11832-11836.

7. Laudadio, G.; De Smet, W.; Struik, L.; Cao, Y. and Noël, T. Design and Application of a Modular and Scalable Electrochemical Flow Microreactor. *Journal of Flow Chemistry* **2018**, 8 (3), 157-165.

8. Cao, Y.; Padoin, N.; Soares, C. and Noël, T. On the Performance of Liquid-Liquid Taylor Flow Electrochemistry in a Microreactor – A CFD Study. *submitted for publication.*

Acknowledgements

First and foremost, I would like to express my deepest gratitude to my promotor and supervisor Prof. Timothy Noël for the invitation to the group, so that it is possible for me to be a member of NRG with great honor. You are always a proactive practitioner, thus encouraging me to fight for the best. You hold great patience and tolerance to my shortcomings and immature ideas. As an engineer, it is almost unlikely for me to overcome the hurdles of organic chemistry without your mass support and constructive initiatives. Your meticulous attitude and keen insight really infect my values. Thank you so much for the understanding of the past 4 years. I will always keep your admonition in mind: Be more than fine.

Second, I would like to express my gratitude to adjunct professor dr. Natan Padoin. Thank you so much for professional guidance and efficient conduct on computational fluid dynamics. More like a friend than merely an advisor, you are always generous in both work and life. Your extensive knowledge and experience really count in our projects combining electrochemistry & CFD. Your equanimity is the key to all the difficulties we confronted and overcame. It is my great pleasure to be involved in the collaboration with you and Cintia.

Third, I am indebted to all NRG group members, your knowledge in organic chemistry widens my vision in this field. You can always propose useful and inspiring suggestions in the research and progress meetings in time. Your presentations are always instructive. Also, I am grateful to all the collaborators and nice colleagues in SPE group. You are always patient and amiable to give help, kindly and professionally.

Last, I would like to express my deepest gratitude to my family members. Thank you to my mother, father for giving me birth and offering me a sweet home. You make everything easier for me to be a dream chaser. Thank you to my dearest wife Dr. Xintong Ma, for being my inspiration, supporter and academic companion always.

About the author

Yiran Cao was born on 24th April 1991 in Gansu, China. He received his bachelor's degree from Chemical Engineering Department, East China University of Science and Technology in 2009, Shanghai, China. Afterwards, he proceeded his master study in Otto von Guericke University in Magdeburg, Germany and obtained the master's degree of Chemical & Energy Engineering. Since September 2017, he continued pursuing his PhD degree in Chemical Engineering and Chemistry Department, Eindhoven University of Technology under the supervision of Prof.dr. Timothy Noël. His research focus is on engineering electrochemical transformations in continuous-flow reactors.